# SURGICAL GUIDANCE OF SOFT TISSUE SARCOMA EXCISION USING NEAR-INFRARED RAMAN SPECTROSCOPY AND AUTOFLUORESCENCE IMAGING

By
John Quan Minh Nguyen

Dissertation
Submitted to the Faculty of the
Graduate School of Vanderbilt University
in partial fulfillment of the requirements
for the degree of

DOCTOR OF PHILOSOPHY
in
Biomedical Engineering

January 31, 2018
Nashville, Tennessee

Approved:
Anita Mahadevan-Jansen, Ph.D.
Ginger Holt, M.D.
Duco Jansen, Ph.D.
Robert Galloway, Ph.D.
Bruce Damon, Ph.D.

*Dedicated to my family:*

*My mom: Tuyết-Lê*

*My sisters: Jessica and Patricia*

*And my dogs Spark and Lucky*

## ACKNOWLEDGEMENTS

I would like to begin my acknowledgements by thanking all the members of my Ph.D. committee for the time and guidance they have provided to me over the entire duration of my graduate school endeavor. In particular, I would like to thank my advisor, Dr. Anita Mahadevan-Jansen, for her wisdom, mentorship, and training that was vital in preparing me to become an independent researcher. To the rest of my committee, Dr. Ginger Holt, Dr. Duco Jansen, Dr. Robert Galloway, and Dr. Bruce Damon, I will always be appreciative of the insights you have provided into my studies and how you constantly make me question the results of all my studies.

Along with Dr. Holt, would like to acknowledge the other orthopedic oncologists at the Vanderbilt University Medical Center's Vanderbilt-Ingram Cancer Center: Dr. Herbert Schwartz and Dr. Jennifer Halpern. Thank you for welcoming me into your operating rooms with patience and hospitality as I continually floundered like a fish out of water to test and refine my imaging systems. I know many other researchers who would sacrifice their rarest Pokémon cards in order to have that opportunity, and I am forever grateful to have the opportunity to work with you and get your inputs on clinical device development.

To my co-authors and partners in crime, Dr. Zain Gowani and Maggie O'Connor: thank you for your help in making this project possible and providing the motivation for attending early morning cases. And of course, thank you to all my friends across the Vanderbilt University campus and the Biophotonics Center who've helped me in both my academic growth and overall mental well-being over the past few years: Dr. Zhaoyue Shi, Dr. Isaac Pence, Dr. Christine O'Brien, Dr. Giju Thomas, Dr. Chetan Patil, Dr. The-Quyen Nguyen, Dr. Melanie McWade, Jarrod Collins, Mary Dockery, Daniel Gill, Oscar Ayala, Wilson Adams, Jeremy Ford, Emmanuel Mannoh, Bryce

Beddard, Joanna Chen, Dayna Every, Manqing Wang, Jennifer Bateman, Mohit Ganguly, Logan Jenkins, Laura Masson, Katherine Cochran, and Ellen Yeats.

Finally, I would like to thank my mom and my two younger sisters for their ever-present love and support for me in everything that I pursue in life. I doubt that anything I ever do will rival the work and dedication you sacrificed for me. Cảm ơn Mẹ.

This work was made possible by the financial support of the National Institute of Health Ruth L. Kirschstein Predoctoral Individual National Research Service Award (F31CA200358), the Orthopaedic Research and Education Foundation (OREF) / Musculoskeletal Tumor Society (MSTS) Clinical Research Grant in Orthopaedic Oncology, and the Vanderbilt Orthopaedic Institute.

## TABLE OF CONTENTS

Page

## LIST OF TABLES

Page

Table

## LIST OF FIGURES

Page

Figure

# CHAPTER 1

# INTRODUCTION

## 1.1 Motivation

Soft tissue sarcomas (STS) are a rare and often aggressive form of malignant tumors that arise from mesenchymal progenitors and are primarily treated through surgical resection and radiation.[1] According to the American Cancer Society's report for 2017, there were about 12,390 new cases of STS and nearly 4,990 deaths resulting from STS last year in the United States.[2] A positive surgical margin is the greatest predictor of local recurrence,[3] however, margin status are often determined weeks after the surgery and can suffer from sampling error. This delayed process increases patient morbidity rates, increases healthcare costs,[4,5] and indicates the need for a rapid and accurate tool that can provide surgeons with immediate feedback during surgery. The goal of this research is to address this need by developing an optical system for intraoperative assessment of the tumor bed during STS excision. The method will provide real-time and automated feedback to the surgeon regarding margin statuses and the presence of remnant tumor cells in the resection cavity.

## 1.2 Goals

The overall goal of this research is to test the hypothesis that near-infrared (NIR) autofluorescence imaging in combination with Raman spectroscopy can provide differential diagnoses of STS and surrounding tissues with high sensitivity and specificity. Autofluorescence spectroscopy measures the reemitted light from optically excited molecules and has the potential for differentiating diseased and normal tissue based on fluorophore intensities. Raman spectroscopy, on the other hand, measures inelastic light scattering from tissues and can probe molecular, structural, and

compositional changes to uniquely identify various types of tissue. Preliminary results indicate that normal muscle surrounding STS's have significantly stronger NIR autofluorescence intensities compared to tumors. However, the presence of such a NIR fluorophore in muscle has not been previously reported. Therefore, part of the objective will be to characterize this autofluorescence signal and investigate its biochemical and morphological basis. Another part of the objective will be to evaluate the Raman spectra obtained from normal and diseased tissues that typically surround STS's. This will help determine the sensitivity of the approach, the spatial needs, and the detection limits required for designing a next-generation non-invasive optical biopsy tool that combines both autofluorescence imaging and Raman spectroscopy. Three specific aims are thus presented.

### 1.3 Specific Aims

Specific Aim 1: Characterize the optical signatures of STS and surrounding tissues *in vivo.* Patients undergoing STS excision at the Vanderbilt-Ingram Cancer Center will be enrolled under this aim. Raman and autofluorescence spectra will be collected in each patient from multiple sites in the resection cavity and surrounding tissues, as well as from freshly excised tumors in the operating room. Spectra will be compared to histopathology in order to develop a robust algorithm for discriminating STS from normal tissues using multivariate statistical methods.

Specific Aim 2: Develop and test an optical device to evaluate the surgical margin of a large surface area within the tumor bed. A clinically applicable method requires a device that can scan the entire cavity to detect the presence of any residual STS cells as well as probe adjacent tissues for the presence of micro-invasion. The eventual long term goal of this specific aim will be to combine autofluorescence imaging with Raman spectroscopy for STS margin evaluation using a

single device. Autofluorescence imaging will be used to scan the tumor bed for suspicious margins and Raman spectroscopy will be used to assess the presence of localized STS signatures. The device will be tested on tissue simulating phantoms and *in vitro* samples while being refined for tissue assessment. The outcome of this aim will be a set of hardware and software that will be tested on additional patients in the operating room. Successful development of such a methodology will allow for rapid and accurate *in vivo* detection of STS within the tumor bed and surrounding tissues, and could reduce the incidence of inadequate tumor excision. The method would prevent the need for multiple surgeries, reduce the patients' risk of surgical complications, and drastically reduce healthcare costs for this expanding patient population.

Specific Aim 3: Investigate the biochemical and morphological basis for spectral differentiation of tissue types**.** This aim seeks to explain the biological basis behind the increase in NIR autofluorescence observed in normal muscle surrounding an STS. Towards this aim, ex vivo STS and normal tissue samples including muscle and fat will be obtained from a tissue bank. Optical techniques such as confocal Raman microspectrometer will be used to measure the hyperspectral image of each sample at the cellular level. The image, containing thousands of Raman and fluorescence spectra at a spatial resolution of 1 μm, will be analyzed and compared to gold standard histology. In addition, separation experiments will be performed to help identify the molecular weight range of the fluorophores present. Based on these results, small molecule or protein purification techniques in conjunction with excitation-emission matrix fluorescence screening will be used to identify the structural and molecular components that contribute to the spectral differentiation of STS. These components will be further examined as a possible insight for understanding STS pathogenesis.

## 1.4 Summary of Chapters

The dissertation has been organized with the following structure:

Chapter 1 provides a brief introduction to the problem that will addressed by the research herein, while establishing the motivation for the included studies and their overall goals. From there, the specific aims of the dissertation will be defined and expanded upon.

Chapter 2 contains the relevant background information regarding the biology, impact, and treatment of STS's. Current margin assessment methods along with current state-of-the-art techniques will be discussed along with their limitations. From there, the basis behind clinical Raman and autofluorescence spectroscopy will be explained and introduced along with a statement of innovation.

Chapter 3 describes the first ever intraoperative study of STS NIR autofluorescence. Measurements of tumor beds from patients undergoing STS resection were characterized to differentiate between normal tissue and STS, and a tissue-type classification algorithm was developed. A major finding here was that, on average, skeletal muscle exhibits a significantly high NIR autofluorescence intensity followed by STS then fat. This work demonstrates the potential for NIR autofluorescence spectroscopy as a rapid and nondestructive surgical guidance tool that can inform surgeons of suspicious margins in need of immediate re-excision.

In Chapter 4, the potential of NIR Raman spectroscopy for the intraoperative differentiation of STS from surrounding normal tissue is presented. Measurements were collected from patients *in vivo* and a multivariate classification algorithm was developed in order to reduce the feature rich Raman data into a smaller set of key spectral features for tissue type classification complimenting the findings from Chapter 3.

Chapter 5 describes the design and development of a modular intraoperative wide-field NIR autofluorescence imaging system. Expanding on the work seen in Chapter 3, the overlay tissue imaging system (OTIS) allows for measurements over a large 15 x 15 $cm^2$ area at a distance of 35 cm away from the tumor bed. In addition, the system features a real-time projection overlay technique that intuitively displays fluorescence maps directly into the surgical field. The system described in this chapter helps enable the naked-eye visualization of fluorescence differences originally observed in Chapter 3.

Chapter 6 describes an investigation into the biological basis behind the NIR autofluorescence differences between STS, normal muscle, and fat. Protoporphyrin IX was proposed as a hypothesis and tested across a variety of different studies including spectrofluorimetry, high pressure liquid chromatography, mass spectroscopy, flow cytometry, immunohistochemistry, NIR microscopy, and many others. While the results were inconclusive, a conservative conclusion can be made that the unknown fluorophore is at least porphyrin based.

Chapter 7 summarizes and integrates the work presented in dissertation. Recommendations are made for future research, and contributions to science and society are highlighted.

## 1.5 References


1. Demetri, G. D. *et al.* Soft tissue sarcoma. *Journal of the National Comprehensive Cancer Network : JNCCN* **8**, 630-674 (2010).
2. Cancer Facts & Figures 2017. (American Cancer Society, Atlanta, 2017).
3. Alamanda, V. K. *et al.* Predictors and clinical significance of local recurrence in extremity soft tissue sarcoma. *Acta oncologica* **52**, 793-802, doi:10.3109/0284186X.2012.711953 (2013).
4. Pritchard, D. J., Soule, E. H., Taylor, W. F. & Ivins, J. C. Fibrosarcoma--a clinicopathologic and statistical study of 199 tumors of the soft tissues of the extremities and trunk. *Cancer* **33**, 888-897 (1974).
5. Abraham, J. A., Baldini, E. H. & Butrynski, J. E. Management of adult soft-tissue sarcoma of the extremities and trunk. *Expert review of anticancer therapy* **10**, 233-248, doi:10.1586/era.09.193 (2010).

# CHAPTER 2

# BACKGROUND AND SIGNIFICANCE

## 2.1 Soft Tissue Sarcomas

Soft tissue sarcomas (STS) are a rare and heterogeneous group of malignant tumors that arise from mesenchymal progenitors for a variety of tissue types such as muscle, fat, cartilage, blood vessels, and nerves. As a result, there are over 50 different subtypes of STS, each with their own name, classification, and prognosis.[1] According to the 2017 American Cancer Society report, there was an estimated 12,390 new cases of STS and 4,990 related deaths in the United States in the last year alone.[2]

Despite the heterogeneity of STS subtypes, these sarcomas often manifest similarly as localized masses (Figure 2-1) within a muscular compartment, which makes them ideal for surgical excision. Hence, the mainstay of local treatment is to completely excise the tumor with a wide margin of normal tissue to ensure that no malignant cells remain within the tumor bed. Incomplete resection of tumors has been shown to be a primary cause of local recurrence. For patients with residual STS, additional therapies such as postoperative radiation and/or re-excision are often required, which can lead to increases in patient morbidity and healthcare costs.[3-5]

Figure 2-1: Example of an excised STS: Myxofibrosarcoma (bottom) with normal fat and skin margin (top). Note the presentation as a localized mass.

STS can occur anywhere in the body, but most originate in an extremity (59%), the trunk (19%), the retroperitoneum (15%), or the head and neck (9%).6 In terms of epidemiology, distribution of adult STS cases are not correlated with race and gender. No specific etiological agent has been identified, however, a number of environmental factors have been known to be associated with STS development such as exposure to ionizing radiation, alkylating chemotherapeutic agents, chlorophenols, vinyl chloride, and arsenic.[7] Genetic factors including specific recurrent chromosomal translocations have been observed in individual subtypes, however, it has been noted that these alterations also exist in benign soft tissue tumors. In addition, mutations in tumor suppressing genes such as *p53* has been observed in certain STS cases.[8] This is further evidenced by the higher incidence of STS in patients with Li-Fraumeni syndrome, which is linked to germline mutations in the *p53* gene. In general, only a small fraction of STS cases are related to the

previously described environmental or genetic factors. A large majority of STS occur spontaneously without any known etiological agent, and the precise etiology of an individual STS subtype does not impact therapeutic decision-making beyond limiting the use of radiation treatments.[7]

### 2.2 STS Histopathology

STS subtypes are classified according to their presumptive tissue of origin (i.e. the normal tissues the tumor most resembles).[9] Examples include liposarcomas (fat), rhabdomyosarcomas (skeletal muscle), and fibrosarcomas (fibrous connective tissue). In cases where histogensis is uncertain, the tumor is designated by the morphologic appearance of the cells or architectural pattern. Histologically, STS diagnosis and grading is mainly based on morphological observations such as mitotic index, tumor necrosis, cellularity, nuclear atypia, and presence of malignant giant cells.[10] Additionally, immunohistochemical staining can be used to identify presumptive tissue of origin, and in specific cases, fluorescence *in situ* hybridization (FISH) may be used to detect chromosomal translocations that can be used to diagnose certain STS subtypes.[9]

### 2.3 Current Margin Assessment Methods and Limitations

Current intraoperative margin assessment methods are limited and highlight the need for an improved approach that prevents recurrence due to incomplete resection. Pre-operative magnetic resonance imaging (MRI) can provide a general evaluation of the tumor's size and allows for image-guided surgery, however resolution is limited and the technique suffers from low sensitivity to non-lipomatous STS subtypes.[11] Intraoperatively, frozen section biopsies are often acquired for pathologic inspection. This process can take 30 to 60 minutes and is prone to sampling errors, especially when assessing large tumor beds like the one pictured in Figure 2-2.[12] Ultimately, the

definitive evaluation of margin status relies on post-operative serial sectioning of the resected tumor and analysis using full-range histopathology techniques. However, results may take several days to over a week for processing, which may limit treatment options for the surgeon and patient if a positive margin is found.

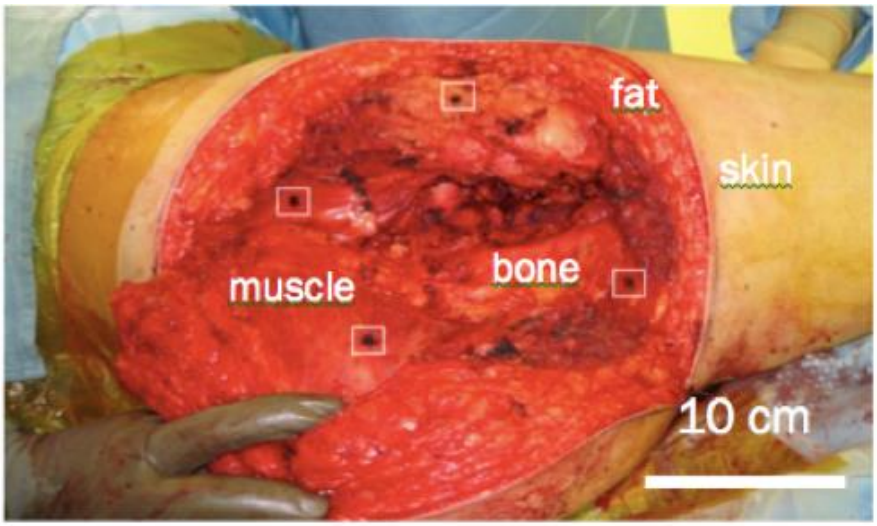


Figure 2-2: Example of a tumor bed after STS excision. Rectangles mark regions biopsied for histopathological evaluation of margin status.

### 2.4 Need and Impact

Limitations in current methods therefore highlight the need for a real-time, accurate, and automated guidance tool that can be used in the operating room during any tumor resection operation so that immediate re-excision of suspicious margins can be performed, thus minimizing the necessity for a second surgery and its associated risks. This would significantly improve the management of STS with respect to both time and cost. In addition, the knowledge gathered from this study could revolutionize the way other sarcomas and tumors are excised by providing surgeons with a tool to accurately identify and locate residual cancers in real-time. Currently, re-excision surgery and postoperative radiation cost about $6,000 to $10,000 per patient while

increasing morbidity rates. In addition, the uncertainty in prognosis introduced by the lack of an intra-operative tool can cause significant physical, emotional, mental, and economic stress for patients.

### 2.5 Optical Methods for STS Detection

In terms of current research methods for tumor margin evaluation, optical techniques have been a relatively popular area of study due to their potential to provide quick, automated, and non-destructive assessment of tissue health. Various groups have researched the potential of optical techniques for STS diagnosis including optical coherence tomography (OCT), Raman spectroscopy, and extrinsic fluorescence agents.

Recently as 2011, groups such as Carbajal *et al* were able to demonstrate the use of OCT to distinguish between normal fat, well-differentiated liposarcomas, and dedifferentiated liposarcomas by analyzing high-resolution structural images analogous to conventional histological methods.[13] However, their study was restricted to morphological analysis as OCT cannot probe the biochemical aspects of the tumor.

Optical techniques such as Raman spectroscopy lack structural information, but allow for tissue assessment through analysis of tumor biochemistry. Groups such as Manoharan *et al* in 1994 identified specific Raman spectral features that could be used to differentiate between liposarcoma and normal adipose tissue using frozen tissue samples.[14] Recent work by Kast *et al.* was able to further differentiate Raman spectral features of rhabdomyosarcoma, Ewing sarcoma, neuroblastoma, and non-Hodgkin's lymphoma with 100% accuracy based on frozen tissue samples.[15] While these groups were able to identify specific Raman spectral features that could be used to differentiate between normal and diseased tissue with high sensitivity and specificity, all

of these studies were based on *in vitro* and animal models that have yet to be translated to clinical study.

As a potential solution for avoiding sampling errors, other groups have attempted to apply fluorescence spectroscopy as a margin assessment method. Groups such as Edward *et al.* demonstrated the feasibility of fluorescence imaging mediated by fluorescent dyes for assessing a large surface area of the tumor bed in an animal model.[16,17] However, the use of potentially toxic exogenous fluorescent dyes hinders the practicality of this approach and thus limits its impact for use in human patients.

The ultimate goal of this research is to develop a surgical guidance tool that combines both NIR autofluorescence imaging and Raman spectroscopy for the intraoperative assessment of the tumor bed during STS excision. Ideally, this margin analysis system will be easy to implement and will provide a quick and cost-effective method that can be adapted into an operating room. NIR wavelengths between 700 to 900 nm will be targeted according to application in order to target the necessary intrinsic biomarkers.[18] Within this optical window, scattering is the most dominant light-tissue interaction and will allow for millimeter scale penetration depths that are ideal for studying the diagnosis and detection of residual tumors.

### 2.6 Autofluorescence Spectroscopy

Autofluorescence spectroscopy is a technique for measuring the intrinsic fluorescence signals that result from natural biological fluorophores such as flavins, porphyrins, collagen, elastin, and NADH.[19] Unlike the fluorescence spectroscopy techniques mentioned earlier, it does not require the use of any potentially toxic exogenous contrast agents.

As illustrated by the Jablonski diagram in Figure 2-3, fluorescence occurs when a fluorophore absorbs light and is excited from a singlet ground state, $S_0$, to a higher electronic state $S_1$ or $S_2$.[19] With a few rare exceptions, excited molecules will rapidly relax to the lowest electronic state, $S_1$, through a process known as internal conversion. From there, return to ground state can result in fluorescence photon emission. From the same figure, it can be seen that the energy of the emission is typically less than that of absorption, hence, fluorescence often occurs at longer wavelengths than the excitation photon. This energy difference between the excitation photon and the emitted photon is known as Stoke's Shift.

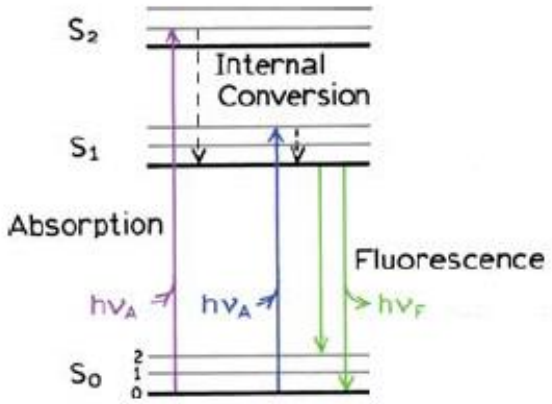


Figure 2-3: Jablonski diagram illustrating light absorption and fluorescence emission.[19]

Another property of fluorescence is that the emission is generally observed irrespective of the excitation wavelength as long as absorption is achieved.[19] This is because upon excitation into a higher electronic state, any excess energy is quickly dissipated until the fluorophore is in the lowest $S_1$ electronic state where fluorescence emission is most dominant. However, excitation only occurs when the incident photons contains energy that corresponds to the energy difference between two different singlet states of a particular molecule. Thus, the amount of energy required for excitation

varies depending on fluorophore and can be optimized for maximal fluorescence depending on the molecule of interest.

Autofluorescence has been shown to differ between normal and neoplastic tissues due to changes in fluorophore concentration or environment related to disease progression.[20] It has been researched as a diagnostic method in various organ systems including the brain,[21-24] bronchus,[25] colon,[26] cervix,[27] bladder,[28] esophagus,[29] skin,[30] breast,[31] and arterial wall.[32] More recently, researchers have attempted to use this technique for therapeutic guidance and assessment of surgery. For example, autofluorescence imaging was used to evaluate the status of breast surgical margins with a classification accuracy of about 85%.[33] While autofluorescence has been investigated extensively for disease detection, the technique itself is prone to poor specificity due to broad spectral peaks.

### 2.7 Raman Spectroscopy

Unlike fluorescence spectroscopy which measures the emission of photons resulting from an excited sample, Raman spectroscopy measures the energy shifts of scattered light from a sample.[34] As mentioned earlier, if the energy of an incident photon corresponds to the energy gap between the ground state of a molecule and an excited state, the photon may be absorbed and the molecule promoted to the higher energy state. However, it is also possible for the photon to interact with the molecule and scatter from it. In this case, it is not required that the photon have an energy that matches the difference between two energy levels of the molecule. While the majority of photons will be elastically scattered with very small energy changes (Rayleigh scattering), a few photons can inelastically scatter and cause a molecule to enter a virtual excited state before returning to a ground state higher (Raman Stokes scattering) or lower (Raman Anti-Stokes scattering) than the

incident photon. The resulting photons from the molecule's return to ground state will thus exhibit an energy shift from the input light as illustrated by the diagram in Figure 2-4. This inherently weak process is known as Raman scattering and occurs in only one out every $10^6$ to $10^8$ photons that scatter. Thus, Raman spectroscopy measurements often require a powerful laser source and sensitive detector, as well as a method for removing the much stronger fluorescence background that may be present. This scattering phenomena is independent of the input wavelength and produces a spectrum based on the Raman energy shifts relative to the input wavelength. Each peak in a Raman spectrum represents a different vibrational mode of the sample's chemical bonds or functional groups. These narrow peaks are highly specific and allows for a "biochemical fingerprint" of molecular structure.

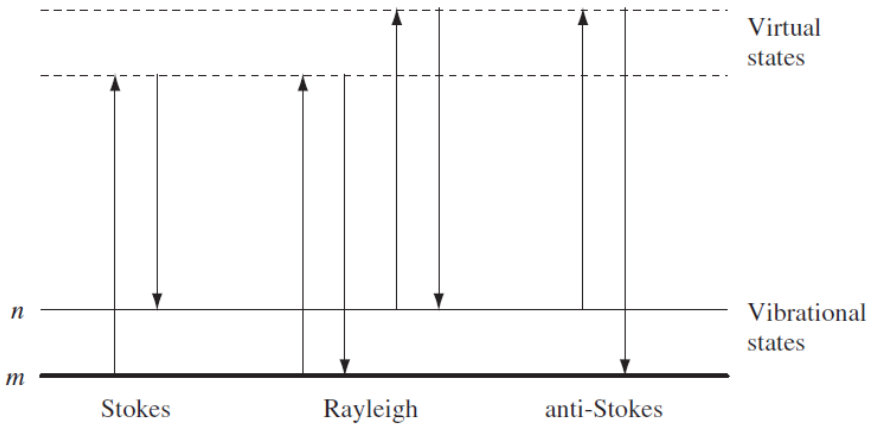


Figure 2-4: Jablonski diagram of Stokes Raman scattering, Rayleigh scattering, and Raman anti-Stokes scattering. [34]

Because many biological molecules have distinguishably unique spectra, the biochemical composition of a tissue can be determined from its Raman spectrum. One particularly relevant biochemical change for cancer cells is an increase in the nucleic acid content associated with increased proliferation and genetic instability. This, along with others such as changes in glycogen and collagen can all be detected by Raman spectroscopy.[35,36] Several research groups have

exploited Raman spectroscopy for disease diagnosis in many organs, including the cervix,[37,38] bladder, prostate,[39] lung,[40] skin,[41,42] and GI tract.[43-45] The Mahadevan-Jansen laboratory at Vanderbilt in particular is a well-known pioneer in the *in vivo* application of Raman spectroscopy for disease detection and has recently reported the application of spatially offset Raman spectroscopy to discriminate negative or positive margins of breast tissue samples with 95% sensitivity and 100% specificity.[46,47]

### 2.8 Combination of Raman Spectroscopy and Autofluorescence Imaging

Although Raman and fluorescence are two distinct optical phenomena, they can occur concurrently when light is illuminated on the sample. Thus, a sample's Raman and autofluorescence signals can be simultaneously measured using the same instrument. Figure 2-5(a) shows the raw measured spectrum of a tissue sample at 785 nm excitation. This spectrum contains both Raman and autofluorescence information, and the autofluorescence signal can be approximated using polynomial fitting as seen in the green curve in Figure 2-5(b). The Raman spectrum is shown in red in Figure 2-5(b) and is obtained by subtracting the fluorescence from the raw data.

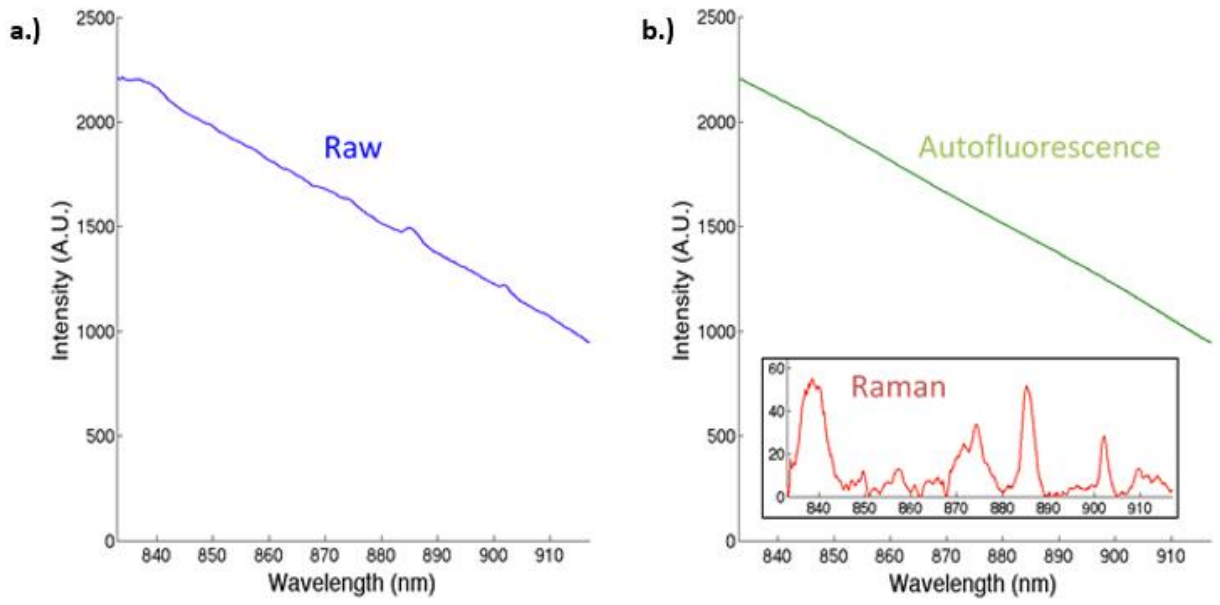


Figure 2-5: Decomposition of raw spectroscopy into its constituent Raman and autofluorescence spectra. (a) Raw measured spectrum. (b) Separated autofluorescence and Raman spectrum

This research project will use a combination of Raman spectroscopy and autofluorescence imaging to provide a complete assessment of the tumor bed and surrounding tissues after STS excision. The developed optical device will detect the presence of any residual sarcoma cells within the tumor bed, report their location to surgeons so that more tissue can be removed, and thus help to ensure complete removal of the tumor with clear margins in a single procedure. This device would solve a critical problem in STS care by greatly reducing or eliminating the need for re-operation/radiation, as well as reducing the time, cost, and anxiety associated with repeat surgeries and additional radiation.

Currently, only one group has attempted to combine autofluorescence and Raman spectroscopy for differentiating normal tissue and STS. In 2005, Huang *et al*, published a study in which Raman spectroscopy and single-point autofluorescence spectra were acquired from mice subcutaneously implanted with fibrosarcoma cells.[48] This method, when used to compare between normal skin and

fibrosarcoma, was able to achieve a diagnostic sensitivity of 93.8% and a specificity of 100%. Tumors were not exposed and native tissues within the bed were not assessed in the comparison. No further studies were published here after.

### 2.9 Innovation

The innovation of this research is two-fold:

1. No other group in the literature has applied intrinsic optical imaging and spectroscopy for guidance of STS excision within human patients. The Huang study in particular never moved onto clinical human studies, nor were other types of common STS such as liposarcomas or undifferentiated pleomorphic sarcomas investigated in their study.
2. This research project seeks to develop a clinical device using the unique combination of NIR autofluorescence imaging with Raman spectroscopy for this application. The innovation is in the distinct preliminary observation that normal tissues typically surrounding STS's are highly fluorescent in the NIR and may have potential as a widefield imaging technique for detecting remnant STS cells in the tumor bed. Because of the large number of known intrinsic fluorophores with excitation in the ultraviolet or visible wavelength range, not many researchers have investigated NIR autofluorescence for disease detection. Furthermore, this enhanced signal in the NIR as a function of disease state has not been previously observed and is a distinctive innovation of this work.

## 2.10 References


1. Demetri, G. D. *et al.* Soft tissue sarcoma. *Journal of the National Comprehensive Cancer Network : JNCCN* **8**, 630-674 (2010).
2. Cancer Facts & Figures 2016. (American Cancer Society, Atlanta, 2016).
3. Atean, I. *et al.* Prognostic factors of extremity soft tissue sarcoma in adults. A single institutional analysis. *Cancer radiotherapie : journal de la Societe francaise de radiotherapie oncologique* **16**, 661-666, doi:10.1016/j.canrad.2012.05.021 (2012).
4. Blakely, M. L. *et al.* The impact of margin of resection on outcome in pediatric nonrhabdomyosarcoma soft tissue sarcoma. *Journal of pediatric surgery* **34**, 672-675 (1999).
5. Gronchi, A. *et al.* Status of surgical margins and prognosis in adult soft tissue sarcomas of the extremities: a series of patients treated at a single institution. *Journal of clinical oncology : official journal of the American Society of Clinical Oncology* **23**, 96-104, doi:10.1200/JCO.2005.04.160 (2005).
6. Cormier, J. N. & Pollock, R. E. Soft tissue sarcomas. *CA: a cancer journal for clinicians* **54**, 94-109 (2004).
7. Pisters, P. T. in *Surgery* (eds JeffreyA Norton *et al.*) Ch. 80, 1753-1777 (Springer Berlin Heidelberg, 2001).
8. Sreekantaiah, C., Ladanyi, M., Rodriguez, E. & Chaganti, R. S. Chromosomal aberrations in soft tissue tumors. Relevance to diagnosis, classification, and molecular mechanisms. *The American journal of pathology* **144**, 1121-1134 (1994).
9. Christopher D.M. Fletcher, K. K. U., Fredrik Mertens. (ed Leslie H. Sobin Paul Kleihues) (International Agenecy for Research on Cancer (IARC), 2002).
10. Guillou, L. *et al.* Comparative study of the National Cancer Institute and French Federation of Cancer Centers Sarcoma Group grading systems in a population of 410 adult patients with soft tissue sarcoma. *Journal of clinical oncology : official journal of the American Society of Clinical Oncology* **15**, 350-362, doi:10.1200/JCO.1997.15.1.350 (1997).
11. Gould, S. W. *et al.* Resection of soft tissue sarcomas with intra-operative magnetic resonance guidance. *Journal of magnetic resonance imaging : JMRI* **15**, 114-119 (2002).
12. Shives, T. C. Biopsy of soft-tissue tumors. *Clinical orthopaedics and related research*, 32-35 (1993).

13. Carbajal, E. F. *et al.* Revealing retroperitoneal liposarcoma morphology using optical coherence tomography. *Journal of biomedical optics* **16**, 020502, doi:10.1117/1.3541789 (2011).
14. Manoharan, R. *et al.* Raman spectroscopy for cancer detection: instrument development and tissue diagnosis. *Proceedings of SPIE* **2328**, 128-132 (1994).
15. Kast, R. *et al.* Differentiation of small round blue cell tumors using Raman spectroscopy. *Journal of pediatric surgery* **45**, 1110-1114, doi:10.1016/j.jpedsurg.2010.02.072 (2010).
16. Eward, W. C. *et al.* A novel imaging system permits real-time in vivo tumor bed assessment after resection of naturally occurring sarcomas in dogs. *Clinical orthopaedics and related research* **471**, 834-842, doi:10.1007/s11999-012-2560-8 (2013).
17. Demos, S. G., Gandour-Edwards, R., Ramsamooj, R. & White, R. Near-infrared autofluorescence imaging for detection of cancer. *Journal of biomedical optics* **9**, 587-592, doi:10.1117/1.1688812 (2004).
18. Hadjipanayis, C. G., Jiang, H., Roberts, D. W. & Yang, L. Current and future clinical applications for optical imaging of cancer: from intraoperative surgical guidance to cancer screening. *Seminars in oncology* **38**, 109-118, doi:10.1053/j.seminoncol.2010.11.008 (2011).
19. Lakowicz, J. R. *Principles of Fluorescence Spectroscopy*. 3rd edn, (Springer US, 2006).
20. Lakowicz, J. R. *Principles of Fluorescence Spectroscopy*. (Plenum Press, 1983).
21. Lin, W. C., Toms, S. A., Motamedi, M., Jansen, E. D. & Mahadevan-Jansen, A. Brain tumor demarcation using optical spectroscopy; an in vitro study. *Journal of biomedical optics* **5**, 214-220, doi:10.1117/1.429989 (2000).
22. Lin, W. C., Toms, S. A., Johnson, M., Jansen, E. D. & Mahadevan-Jansen, A. In vivo brain tumor demarcation using optical spectroscopy. *Photochemistry and photobiology* **73**, 396-402 (2001).
23. Chung, Y. G., Schwartz, J. A., Gardner, C. M., Sawaya, R. E. & Jacques, S. L. Diagnostic potential of laser-induced autofluorescence emission in brain tissue. *Journal of Korean medical science* **12**, 135-142 (1997).
24. Bottiroli, G. *et al.* Brain tissue autofluorescence: an aid for intraoperative delineation of tumor resection margins. *Cancer detection and prevention* **22**, 330-339 (1998).

25. Zellweger, M. *et al.* In vivo autofluorescence spectroscopy of human bronchial tissue to optimize the detection and imaging of early cancers. *Journal of biomedical optics* **6**, 41-51, doi:10.1117/1.1332774 (2001).
26. Richards-Kortum, R. *et al.* Spectroscopic diagnosis of colonic dysplasia. *Photochemistry and photobiology* **53**, 777-786 (1991).
27. Ramanujam, N. *et al.* Cervical precancer detection using a multivariate statistical algorithm based on laser-induced fluorescence spectra at multiple excitation wavelengths. *Photochemistry and photobiology* **64**, 720-735 (1996).
28. D'Hallewin, M. A., Baert, L. & Vanherzeele, H. Fluorescence imaging of bladder cancer. *Acta urologica Belgica* **62**, 49-52 (1994).
29. Panjehpour, M. *et al.* Spectroscopic diagnosis of esophageal cancer: new classification model, improved measurement system. *Gastrointest Endosc* **41**, 577-581 (1995).
30. Chwirot, B. W., Chwirot, S., Redzinski, J. & Michniewicz, Z. Detection of melanomas by digital imaging of spectrally resolved ultraviolet light-induced autofluorescence of human skin. *European journal of cancer* **34**, 1730-1734 (1998).
31. Gupta, P. K., Majumder, S. K. & Uppal, A. Breast cancer diagnosis using N2 laser excited autofluorescence spectroscopy. *Lasers in surgery and medicine* **21**, 417-422 (1997).
32. Warren, S. *et al.* Combined ultrasound and fluorescence spectroscopy for physico-chemical imaging of atherosclerosis. *IEEE transactions on bio-medical engineering* **42**, 121-132, doi:10.1109/10.341824 (1995).
33. Keller, M. D. *et al.* BSuB6 (Optical Society of America).
34. Smith, E. & Dent, G. Modern Raman Spectroscopy – A Practical Approach. (2005).
35. Mahadevan-Jansen, A. in *Raman Spectroscopy: From Benchtop to Bedside, Biomedical Photonics Handbook,* (ed 30:1-30:27 T. Vo-Dinh, CRC Press, Washington DC, 2003.).
36. Mahadevan-Jansen, A. & Richards-Kortum, R. R. Raman spectroscopy for the detection of cancers and precancers. *Journal of biomedical optics* **1**, 31-70, doi:10.1117/12.227815 (1996).
37. Mahadevan-Jansen, A. *et al.* Near-infrared Raman spectroscopy for in vitro detection of cervical precancers. *Photochemistry and photobiology* **68**, 123-132 (1998).
38. Mahadevan-Jansen, A., Mitchell, M. F., Ramanujam, N., Utzinger, U. & Richards-Kortum, R. Development of a fiber optic probe to measure NIR Raman spectra of cervical tissue in vivo. *Photochemistry and photobiology* **68**, 427-431 (1998).

39. Crow, P. *et al.* Assessment of fiberoptic near-infrared raman spectroscopy for diagnosis of bladder and prostate cancer. *Urology* **65**, 1126-1130, doi:10.1016/j.urology.2004.12.058 (2005).
40. Huang, Z. *et al.* Near-infrared Raman spectroscopy for optical diagnosis of lung cancer. *International journal of cancer. Journal international du cancer* **107**, 1047-1052, doi:10.1002/ijc.11500 (2003).
41. Lieber, C. A., Majumder, S. K., Ellis, D. L., Billheimer, D. D. & Mahadevan-Jansen, A. In vivo nonmelanoma skin cancer diagnosis using Raman microspectroscopy. *Lasers in surgery and medicine* **40**, 461-467, doi:10.1002/lsm.20653 (2008).
42. Sigurdsson, S. *et al.* Detection of skin cancer by classification of Raman spectra. *IEEE transactions on bio-medical engineering* **51**, 1784-1793, doi:10.1109/TBME.2004.831538 (2004).
43. Shetty, G., Kendall, C., Shepherd, N., Stone, N. & Barr, H. Raman spectroscopy: elucidation of biochemical changes in carcinogenesis of oesophagus. *British journal of cancer* **94**, 1460-1464, doi:10.1038/sj.bjc.6603102 (2006).
44. Shim, M. G., Song, L. M., Marcon, N. E. & Wilson, B. C. In vivo near-infrared Raman spectroscopy: demonstration of feasibility during clinical gastrointestinal endoscopy. *Photochemistry and photobiology* **72**, 146-150 (2000).
45. Molckovsky, A., Song, L. M., Shim, M. G., Marcon, N. E. & Wilson, B. C. Diagnostic potential of near-infrared Raman spectroscopy in the colon: differentiating adenomatous from hyperplastic polyps. *Gastrointest Endosc* **57**, 396-402, doi:10.1067/mge.2003.105 (2003).
46. Keller, M. D. *et al.* Development of a spatially offset Raman spectroscopy probe for breast tumor surgical margin evaluation. *Journal of biomedical optics* **16**, 077006, doi:10.1117/1.3600708 (2011).
47. Mahadevan-Jansen A *et al.* Looking Below the Surface of Breast Tissue during Surgery. *Spectroscopy* (2011).
48. Huang, Z., Lui, H., McLean, D. I., Korbelik, M. & Zeng, H. Raman spectroscopy in combination with background near-infrared autofluorescence enhances the in vivo assessment of malignant tissues. *Photochemistry and photobiology* **81**, 1219-1226, doi:10.1562/2005-02-24-RA-449 (2005).

# CHAPTER 3

# NEAR-INFRARED AUTOFLUORESCENCE SPECTROSCOPY OF *IN VIVO* SOFT TISSUE SARCOMAS

John Quan Nguyen, [1*] Zain Gowani,[2] Maggie O'Connor,[1] Isaac Pence,[1]

The-Quyen Nguyen,[3] Ginger Holt,[4] Anita Mahadevan-Jansen[1]

[1]Biophotonics Center, Vanderbilt University, 410 24th Ave. South (Keck FEL Center), Nashville, TN 37232

[2]School of Medicine, Vanderbilt University, 2215 Garland Ave (Light Hall), Nashville, TN 37232

[3]Biomedical Engineering Department, Northwestern University, Silverman Hall, Evanston, IL 60208

[4]Vanderbilt-Ingram Cancer Center, Vanderbilt University Medical Center, 691 Preston Building, Nashville, TN 37232-6838

The work comprised in this chapter was published in:

"Near-infrared autofluorescence spectroscopy of *in vivo* soft tissue sarcomas"

*Optics Letters*, Volume 40, Issue 23, Page 5498-5501 (2015)

## 3.1 Abstract

Soft tissue sarcomas (STS) are a rare and heterogeneous group of malignant tumors that are often treated via surgical resection. Inadequate resection can lead to local recurrence and decreased survival rates. In this study, we investigate the hypothesis that near-infrared (NIR) autofluorescence can be utilized for tumor margin analysis by differentiating STS from the surrounding normal tissue. Intraoperative in vivo measurements were acquired from 30 patients undergoing STS resection and were characterized to differentiate between normal tissue and STS. Overall, normal muscle and fat were observed to have the highest and lowest autofluorescence intensities, respectively, with STS falling in between. With the exclusion of well-differentiated liposarcomas, the algorithm's accuracy for classifying muscle, fat, and STS was 93%, 92% and 88% respectively. These findings suggest that NIR autofluorescence spectroscopy has potential as a rapid and non-destructive surgical guidance tool that can inform surgeons of suspicious margins in need of immediate re-excision.

## 3.2 Background

Soft tissue sarcomas (STS) are a rare and heterogeneous group of malignant tumors that arise from mesenchymal progenitors for a variety of tissue types such as muscle, fat, cartilage, blood vessels, and nerves. As a result, there are over 50 different subtypes of STS, each with their own name, classification, and prognosis.[1] STS can occur anywhere in the body, but most originate in an extremity (59%), the trunk (19%), the Retroperitoneum (15%), or the head and neck (9%).[2]

Despite the heterogeneity of STS subtypes, these sarcomas often manifest similarly as localized masses within a muscular compartment, which makes them ideal for surgical resection. Hence, the mainstay of local treatment is to completely excise the tumor with a wide margin of normal tissue to ensure that all malignant cells are removed from the tumor bed while avoiding unnecessary damage to the surrounding muscle, blood vessels, nerves, and bone. Incomplete resection of tumors has been shown to be a primary cause of local recurrence.[3] For patients with residual STS, additional therapies such as postoperative radiation and/or re-excision are often required, which can lead to increases in patient morbidity and healthcare costs.[4-6]

Current surgical guidance and margin assessment methods are limited and highlight the need for an improved approach to ensure complete resections. Pre-operative magnetic resonance imaging (MRI) can provide a general evaluation of the tumor's size and allows for image-guided surgery, however, resolution is limited and the technique suffers from low sensitivity.[7] Intraoperatively, frozen section biopsies are often acquired for pathologic inspection. This process can take 30 to 60 minutes and is prone to sampling errors, especially when assessing large tumor beds.[8] Ultimately, the definitive evaluation of margin status relies on post-operative serial sectioning of the resected tumor and analysis using full-range histopathology techniques. However, results may

take several days to over a week for processing, which may limit treatment options for the surgeon and patient if a positive margin is found.

In terms of current research methods for tumor margin evaluation, optical techniques have been a relatively popular area of study due to their potential to provide quick, automated, and non-destructive assessment of tissue health. Techniques such as optical coherence tomography allow for morphological studies akin to physical biopsies[9] while other techniques, such as Raman spectroscopy, allow for extensive biochemical analysis[10]. However, due to the rarity of the disease, the majority of research for STS margin evaluation has been limited to *in vitro* and animal studies.

Of these optical modalities, autofluorescence spectroscopy is a technique for measuring the intrinsic light emissions from natural biological fluorophores that are excited by a light source. It does not require the use of any toxic exogenous contrast agents and has been shown to differentiate between normal and neoplastic tissue based on changes in fluorophore concentrations and environment related to disease progression.[11] Compared to other optical techniques, autofluorescence spectroscopy is relatively easy to implement and can provide a quick and cost-effective method for discriminating between diseased and normal tissue. However, because of the large number of known intrinsic fluorophores with excitation in the ultraviolet or visible wavelength range, few researchers have studied near infrared (NIR) autofluorescence for disease detection.[11]

In this paper, we investigate the hypothesis that NIR autofluorescence spectra can be used to differentiate *in vivo* STS from the surrounding normal tissue commonly encountered within a surgical tumor bed.

## 3.3 Materials and Methods

### *3.3.1 Patient Recruitment*

Intraoperative *in vivo* autofluorescence spectra were collected under written informed consent as approved by the Vanderbilt University Institutional Review Board. Thirty subjects were recruited at the Vanderbilt University Medical Center (VUMC) from amongst patients screened for STS excisional surgery. A detailed breakdown of tissue types, number of patients, and number of measurements can be seen in Table 3-1.

| Tissue Type | Patients | Measurements |
|---|---|---|
| Normal Muscle | 26 | 215 |
| Normal Fat | 28 | 170 |
| Well-Differentiated Liposarcoma | 6 | 63 |
| Myxofibrosarcoma | 2 | 30 |
| Undifferentiated Pleomorphic Sarcoma | 2 | 40 |
| Sclerosing Epithelioid Fibrosarcoma | 2 | 19 |
| Pleomorphic Rhabdomyosarcoma | 1 | 15 |
| Pleomorphic Liposarcoma | 1 | 14 |
| Pleomorphic Myxoid Liposarcoma | 1 | 10 |

Table 3-1: Recruitment table listing tissue type, number of patients, and number of measurements collected for this study.

### *3.3.2 Intraoperative Autofluorescence Spectroscopy*

The mobile spectroscopy system consists of a custom-designed 7x1 fiberoptic probe (EmVision LLC, Loxahatchee, FL) connected to a HoloSpec f/1.8i imaging spectrograph (Kaiser Optical Systems Inc., Ann Arbor, MI) equipped with a deep depletion CCD (Princeton Instruments, Trenton, NJ, SPEC-10:256BR). The probe's light source consists of a 785 nm diode laser

(Innovative Photonic Solutions, NJ, I0785MM0350MS) and output power at the probe's tip was regulated to 80 mW. Each spectrum's wavelength axis was calibrated with a neon-argon light source. In addition, wavelength-dependent response of the system was calibrated using a secondary reflective standard to a NIST-certified quartz-tungsten-halogen lamp. (Oriel Instruments, Irvine, CA, 63355)

After each tumor was completely excised, the sterilized fiberoptic probe was handed to the surgeon. During each measurement, all ambient light within the operating room was turned off and/or covered. Measurements were made from various tissues within the tumor bed, which included control healthy tissue such as muscle, fat, nerves, bone, and blood vessels as identified by the surgeon. Afterwards, a small incision was made on the excised tumor and measurements were made within the tumor's interior. STS subtype was confirmed via post-operative histopathology.

Measurements were acquired using 0.5-second exposures summed over 5 accumulations. Five sets of measurements were acquired at each tissue of interest.

### *3.3.3 Data Analysis*

Spectral data was smoothed using a Savitzky-Golay filter and fitted to a $7^{th}$ order polynomial in order to extract the autofluorescence profile for each sample from 810 to 918 nm.[12]

To account for the varying patient-dependent range of autofluorescence intensities, each patient's data set was standardized using min-max feature scaling to a range between 0 and 1. Unpaired Student's t-test was utilized to determine significant differences between tissue types based on the spectral area under the curve.

Features from the standardized data including area under the curve and slopes from five equal segments of the spectra were used to generate a predictive classifier algorithm based on multinomial logistic regression.[13] Area under the curve was selected as many of the spectra did not exhibit an autofluorescence peak within the acquired spectral range. Slopes were chosen in order to incorporate spectral line shape into the model. While other methods such as polynomial fitting could have been applied, a simple slope based approach was selected as it is less computationally intensive and would allow for future work towards real-time processing. Five slopes were chosen in order to minimize testing error and overfitting. These include the slopes from 810 to 830 nm, 830 to 850 nm, 850 to 871 nm, 871 to 894 nm, and 894 to 918 nm.

The algorithm was then tested to differentiate normal muscle, normal fat, and STS using leave-one-patient-out cross validation. During this process, one patient's set of measurements would be excluded and a model would be trained using the remaining data sets before being tested on the previously excluded measurements. In order to avoid bias, each model was trained and tested independently for all 30 patients without the use of an aggregate model. Due to the rarity of specific STS subtypes as seen in Table 3-1, our study was not powered for subtype differentiation.

### 3.4 Results

Average raw autofluorescence for each tissue type measured in this study can be seen in Figure 3-1(a). Average raw autofluorescence spectra including 95% confidence intervals for normal muscle, normal fat, and all STS can be seen Figure 3-1(b). Standardized area under the curve for each tissue was calculated in order to generate a single value for comparing the overall intensity differences between normal muscle, normal fat, and STS as shown in Figure 3-2. An unpaired Student's t-test was performed and significant differences ($p << 0.01$) were observed amongst each

group. From both Figure 3-1(a-b) and Figure 3-2, it can be seen that normal muscle and fat within the tumor bed have both the highest and lowest autofluorescence intensities respectively, while STS intensities tend to fall in between. Due to STS heterogeneity, a larger spread in confidence interval was observed for the STS autofluorescence intensitites.

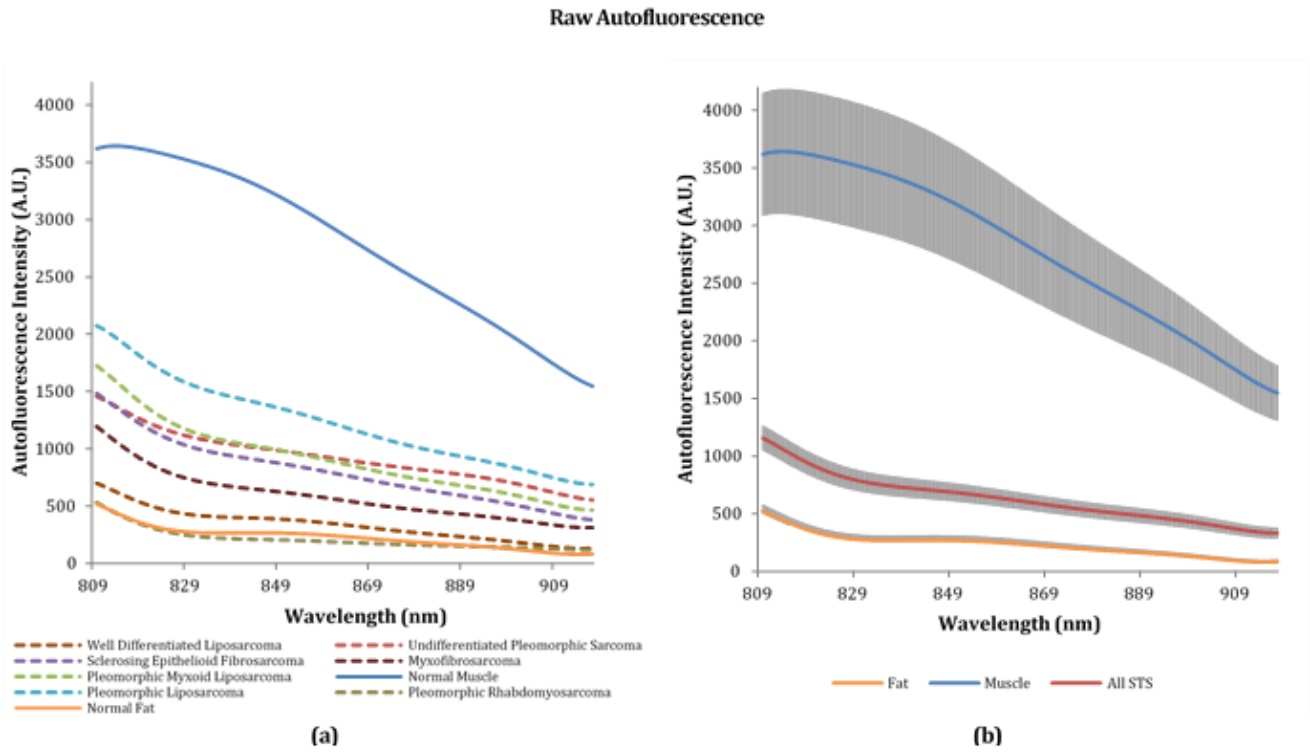


Figure 3-1: Raw autofluorescence spectra resulting from a 785 nm excitation source. a.) Average raw spectra for each tissue type b.) Average raw spectra with 95% confidence intervals for normal muscle, normal fat, and all STS's averaged into a single spectrum.

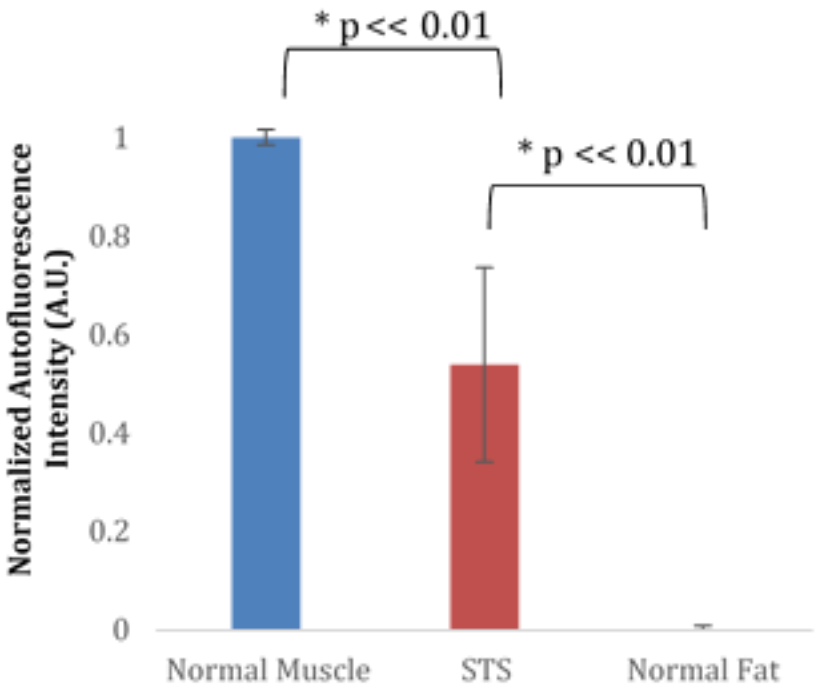


Figure 3-2: Standardized fluorescence area under the curve distribution for normal muscle, STS, and normal fat. Error bars indicate 95% confidence interval. Significant differences are marked with an asterisk.

Features from the standardized spectra were subsequently used in a classification algorithm based on multinomial logistic regression, which was then tested using leave-one-patient-out cross validation. The total performance from all individual tests can be seen in the confusion matrices shown in Table 3-2 and Table 3-3 where each row represents a true class and each column represents a predicted class. Correctly identified classes are highlighted in the diagonal. The algorithm's accuracy in classifying normal muscle, normal fat, and all STS was 89%, 84%, and 56% respectively. With the exclusion of well-differentiated liposarcomas, the algorithm's accuracy in classifying normal muscle, normal fat, and STS increased to 93%, 92%, and 88% respectively.

| | | *Prediction* | | |
|---|---|---|---|---|
| | | **Muscle** | **Fat** | **STS** |
| ***Actual*** | **Muscle** | 192 | 1 | 22 |
| | **Fat** | 0 | 144 | 26 |
| | **STS** | 11 | 73 | 107 |

Table 3-2: Normal tissue vs STS confusion matrix visualizing the total results from validating the multinomial logistic regression classification algorithm using a leave-one-patient-out technique. Correct predictions are highlighted on each table's diagonal.

| | | *Prediction* | | |
|---|---|---|---|---|
| | | **Muscle** | **Fat** | **STS** |
| ***Actual*** | **Muscle** | 200 | 10 | 5 |
| | **Fat** | 0 | 158 | 12 |
| | **STS** | 5 | 10 | 113 |

Table 3-3: Normal tissue vs STS excluding well-differentiated liposarcomas confusion matrix visualizing the total results from validating the multinomial logistic regression classification algorithm using a leave-one-patient-out technique. Correct predictions are highlighted on each table's diagonal.

### 3.5 Discussion

To the best of our knowledge, this is the first ever NIR autofluorescence study of STS within human patients. Due to the rarity of the disease, a majority of STS optical analysis in the past has been limited to *in vitro* and animal studies. While various optical modalities have been explored for disease detection, NIR autofluorescence has largely been ignored due to the lack of known biological fluorophores beyond the visible spectrum. However, during the course of this study, the presence of NIR autofluorescence within the human body was observed, most notably within normal muscle tissue. The presented results suggest that this autofluorescence could be utilized to

develop a surgical guidance tool for differentiating between STS and the surrounding normal tissue with deeper interrogation depths afforded by the use of NIR wavelengths.

The key observation can be seen in the raw spectra of Figure 3-1(a-b) where normal muscle exhibits a much stronger autofluorescence signal compared to normal fat or any STS subtype. Correspondingly, STS autofluorescence was found to span the intensity range between normal muscle and fat depending on subtype. When the data was standardized to account for inter-patient variability as seen in Figure 3-2, this trend continued to be consistent with significant differences ($p<<0.01$) observed between each tissue type based on overall intensity alone. Using multinomial logistic regression, we were able to develop a classification algorithm for differentiating tissue types based on the standardized spectra, which was then tested using a robust leave-one-patient out validation technique. Despite the broad spectral line shapes, it was possible to identify classification features based on the spectral shape and overall autofluorescence intensities.

Since the two predominant normal tissues within a STS tumor bed are muscle and fat, there was a strong clinical motivation to test the algorithm's capability for discriminating between normal muscle, normal fat, and STS. From the results presented in Table 3-2, it can be seen that our model has high accuracy for identifying normal tissues but a much lower accuracy for detecting STS. The reason for this discrepancy is due to one specific STS subtype, well-differentiated liposarcomas, which in prior research has been shown to have histological similarities to normal fat despite atypia.[14] Consequently, the autofluorescence profile of this STS subtype shares close similarities to that of normal fat. As one of the most commonly diagnosed STS subtypes,[15] it constituted a large majority of our STS data set, which subsequently lowered the accuracy for differentiating

STS from normal fat. When well-differentiated liposarcomas were excluded from the study, a significant increase in accuracy was observed as shown in Table 3-3.

From a clinical standpoint, the inability to differentiate this particular subtype from the surrounding normal fat has a negligible effect on surgical outcome as well-differentiated liposarcomas are one of the lowest grade liposarcomas with the least metastatic potential. Proper treatment that includes pre-operative MRI scans, marginal surgical excision, and post-operative radiation often have 5-year disease specific survival rates close to 95%. [16,17] This is because well-differentiated liposarcomas are often surrounded by large regions of normal fat that can be completely excised without risk of affecting vital tissue such as normal muscle, blood vessels, or nerves. The same cannot be said of any other STS subtype. Even for those that share a lipomatous origin, other subtypes may develop in or around vital tissue that can hinder an attempt at complete tumor resection, thus highlighting the need for an improved intraoperative margin assessment tool. Due to the rare and highly heterogeneous nature of each individual STS subtype, the current study was limited to classification between diseased and non-diseased tissue. Separation of well-differentiated liposarcomas from normal fat, along with further subtype differentiation, may be possible with the use of a more specific optical modality such as near-infrared and high wavenumber Raman spectroscopy.

The basis for NIR autofluorescence within *in vivo* muscle is currently unknown at this time and further studies will have to be conducted. From the spectra presented in Figure 3-1, it can be seen that normal muscle has an intensity peak near 813 nm while STS and normal fat may have peaked prior to our spectral range. This suggests that there may be two fluorophores present within the tumor bed, one of which is unique to normal muscle. Porphyrin derivatives have been hypothesized

as a possible source of near-infrared autofluorescence, however, the longest emitting known porphyrins are currently confined to the visible wavelength regime up to 700 nm.[11] For future work, we will further characterize the autofluorescence signal and investigate its biochemical and morphological origins.

In terms of clinical impact, the results of this study suggest that an optical device based on near-infrared autofluorescence alone could allow for intraoperative tumor margin assessment. If successful, it would allow for real-time and automated feedback to the surgeon regarding suspicious margins that may need to be excised in order to achieve complete tumor resection. This would significantly improve the management of STS with respect to time, patient morbidity, and healthcare costs.

### 3.6 Conclusion

The results of this study suggest that despite broad spectral line shapes, NIR autofluorescence spectroscopy can be used to differentiate *in vivo* STS from the surrounding normal muscle and fat. This was accomplished by generating a classifier algorithm based on multinomial logistic regression with overall autofluorescence intensity and slopes from five segments of the spectra used as inputs. With the exclusion of well-differentiated liposarcomas, the algorithm was able to perform with 88% accuracy when classifying STS from other normal tissues. In addition, a strong NIR autofluorescence signal from normal muscle was observed that has not been reported in past literature. The identity of this intrinsic fluorophore is currently unknown and will be the subject of future work.

## 3.7 Acknowledgements

We would like to thank Dr. Herbert Schwartz, Dr. Jennifer Halpern, Dr. Krishna Reddy, Dr. Nathan Mesko, and all participating surgical personnel for their patience and assistance in this work.

This work was supported by the National Cancer Institute of the National Institutes of Health under Award Number F31CA200358, the Orthopaedic Research and Education Foundation / Muscle Skeletal Tumor Society Clinical Research Grant in Orthopaedic Oncology, the Vanderbilt Orthopaedic Institute, and the Vanderbilt Medical Scholars Fellowship.

### 3.8 References


1. Demetri, G. D. *et al.* Soft tissue sarcoma. *Journal of the National Comprehensive Cancer Network : JNCCN* **8**, 630-674 (2010).
2. Cormier, J. N. & Pollock, R. E. Soft tissue sarcomas. *CA: a cancer journal for clinicians* **54**, 94-109 (2004).
3. Alamanda, V. K. *et al.* Incomplete excisions of extremity soft tissue sarcomas are unaffected by insurance status or distance from a sarcoma center. *Journal of surgical oncology* **108**, 477-480, doi:10.1002/jso.23427 (2013).
4. Atean, I. *et al.* Prognostic factors of extremity soft tissue sarcoma in adults. A single institutional analysis. *Cancer radiotherapie : journal de la Societe francaise de radiotherapie oncologique* **16**, 661-666, doi:10.1016/j.canrad.2012.05.021 (2012).
5. Blakely, M. L. *et al.* The impact of margin of resection on outcome in pediatric nonrhabdomyosarcoma soft tissue sarcoma. *Journal of pediatric surgery* **34**, 672-675 (1999).
6. Gronchi, A. *et al.* Status of surgical margins and prognosis in adult soft tissue sarcomas of the extremities: a series of patients treated at a single institution. *Journal of clinical oncology : official journal of the American Society of Clinical Oncology* **23**, 96-104, doi:10.1200/JCO.2005.04.160 (2005).
7. Gould, S. W. *et al.* Resection of soft tissue sarcomas with intra-operative magnetic resonance guidance. *Journal of magnetic resonance imaging : JMRI* **15**, 114-119 (2002).
8. Shives, T. C. Biopsy of soft-tissue tumors. *Clinical orthopaedics and related research*, 32-35 (1993).
9. Carbajal, E. F. *et al.* Revealing retroperitoneal liposarcoma morphology using optical coherence tomography. *Journal of biomedical optics* **16**, 020502, doi:10.1117/1.3541789 (2011).
10. Manoharan, R. *et al.* Raman spectroscopy for cancer detection: instrument development and tissue diagnosis. *Proceedings of SPIE* **2328**, 128-132 (1994).
11. Lakowicz, J. R. *Principles of Fluorescence Spectroscopy*. 3rd edn, (Springer US, 2006).

12. Lieber, C. A. & Mahadevan-Jansen, A. Automated method for subtraction of fluorescence from biological Raman spectra. *Applied spectroscopy* **57**, 1363-1367, doi:10.1366/000370203322554518 (2003).
13. Johnson, R. A. & Wichern, D. W. *Applied Multivariate Statistical Analysis*. 6th edn, (2007).
14. Evans, H. L., Soule, E. H. & Winkelmann, R. K. Atypical lipoma, atypical intramuscular lipoma, and well differentiated retroperitoneal liposarcoma: a reappraisal of 30 cases formerly classified as well differentiated liposarcoma. *Cancer* **43**, 574-584 (1979).
15. Singer, S., Antonescu, C. R., Riedel, E. & Brennan, M. F. Histologic subtype and margin of resection predict pattern of recurrence and survival for retroperitoneal liposarcoma. *Annals of surgery* **238**, 358-370; discussion 370-351, doi:10.1097/01.sla.0000086542.11899.38 (2003).
16. Crago, A. M. & Singer, S. Clinical and molecular approaches to well differentiated and dedifferentiated liposarcoma. *Current opinion in oncology* **23**, 373-378, doi:10.1097/CCO.0b013e32834796e6 (2011).
17. Dalal, K. M., Kattan, M. W., Antonescu, C. R., Brennan, M. F. & Singer, S. Subtype specific prognostic nomogram for patients with primary liposarcoma of the retroperitoneum, extremity, or trunk. *Annals of surgery* **244**, 381-391, doi:10.1097/01.sla.0000234795.98607.00 (2006).

# CHAPTER 4

# INTRAOPERATIVE RAMAN SPECTROSCOPY OF SOFT TISSUE SARCOMAS

John Quan Nguyen,[1] Zain S. Gowani,[2] Maggie O'Connor,[1] Isaac J. Pence,[1] The-Quyen Nguyen,[3] Ginger E. Holt, MD,[4] Herbert S. Schwartz,[4] Jennifer L. Halpern,[4] Anita Mahadevan-Jansen[1]

[1]Biophotonics Center, Vanderbilt University, 410 24th Ave. South (Keck FEL Center), Nashville, Tennessee 37232, USA

[2]School of Medicine, Vanderbilt University, 2215 Garland Ave (Light Hall), Nashville, Tennessee 37232, USA

[3]Biomedical Engineering Department, Northwestern University, Silverman Hall, Evanston, Illinois 60208, USA

[4]Vanderbilt-Ingram Cancer Center, Vanderbilt University Medical Center, 691 Preston Building, Nashville, Tennessee 37232-6838, USA

The work comprised in this chapter was published in:

"Intraoperative Raman spectroscopy of soft tissue sarcomas"

*Lasers in Surgery and Medicine*, Volume 48, Issue 8, Page 774-781 (2016)

## 4.1 Abstract

Soft tissue sarcomas (STS) are a rare and heterogeneous group of malignant tumors that are often treated through surgical resection. Current intraoperative margin assessment methods are limited and highlight the need for an improved approach with respect to time and specificity. Here we investigate the potential of near-infrared Raman spectroscopy for the intraoperative differentiation of STS from surrounding normal tissue. *In vivo* Raman measurements at 785 nm excitation were intraoperatively acquired from subjects undergoing STS resection using a probe based spectroscopy system. A multivariate classification algorithm was developed in order to automatically identify spectral features that can be used to differentiate STS from the surrounding normal muscle and fat. The classification algorithm was subsequently tested using leave-one-subject-out cross-validation. With the exclusion of well-differentiated liposarcomas, the algorithm was able to classify STS from the surrounding normal muscle and fat with a sensitivity and specificity of 89.5% and 96.4%, respectively. These results suggest that single point near-infrared Raman spectroscopy could be utilized as a rapid and non-destructive surgical guidance tool for identifying abnormal tissue margins in need of further excision.

## 4.2 Introduction

Soft tissue sarcomas (STS) are a rare and heterogeneous group of malignant tumors that derive from mesenchymal progenitors for a variety of tissue types including muscle, fat, cartilage, blood vessels, and nerves. As such, there are over 50 different subtypes of STS, each with their own name and prognosis.[1] According to the 2016 American Cancer Society report, there will be an estimated 12,310 new cases of STS and 4,990 related deaths this year in the United States alone with undifferentiated pleomorphic sarcomas and well-differentiated liposarcomas as the most common STS subtypes in adults.[2] By the numbers, STS is a rare disease that accounts for less than 1% of all new cancers each year, making it a relatively difficult disease to study *in vivo.* Regardless of its prevalence, STS poses an interesting problem in that since 1974, the overall 5 year survival rate following treatment has generally lingered around 60% while treatments methods have not dramatically changed.[3,4]

Despite the large heterogeneity of STS subtypes, the mainstay of local treatment is to completely excise the tumor with a wide margin of normal tissue. During this procedure, the surgeon must ensure that all malignant cells have been removed from the tumor bed while avoiding unnecessary damage to the surrounding muscle, blood vessels, nerves, and bone. Incomplete tumor resection has been shown to be a primary cause of local recurrence, which can often lead to increases in patient morbidity and healthcare costs.[5-8] For patients with residual STS, additional therapies such as postoperative radiation and/or re-excision are often required.

Current methods used for surgical guidance and margin assessment are limited and highlight the need for an improved approach that can ensure complete tumor resections in real time. While techniques such as magnetic resonance imaging can provide a general evaluation of the tumor's

size and location during the pre-operative phase of the procedure, critical margin evaluation during surgery is often accomplished through frozen section biopsies. This process can take upwards of 30 to 60 minutes and is prone to sampling errors, especially when assessing the large tumor beds commonly encountered in these cases.[9] The ultimate evaluation of margin status occurs post-operatively when the resected tumor has been serially sectioned and analyzed using full-range histopathology techniques. However, this may take several days to over a week for processing and can restrict treatment options should a positive margin be found.

In terms of current research methods for tumor margin evaluation, optical techniques have been a popular area of study due to their potential to provide quick, automated, and non-destructive assessment of tissue health. However, due to the rare incidence of STSs, a large majority of these studies have been confined to *in vitro* measurements and animal models. Certain groups have used techniques such as optical coherence tomography in order to study tissue morphology[10] while others have investigated the use of extrinsic contrast agents for delineating tumor margins.[11,12]

We recently reported the first *in vivo* study of STS within human subjects using autofluorescence spectroscopy.[13] By quantitatively measuring the light emissions from an illuminated sample, the study was able to differentiate between normal and cancerous tissue with a sensitivity and specificity of 88.3% and 95.6%, respectively. Although sensitive to changes in bulk tissue properties based on emission intensities, the technique itself is limited in its ability to differentiate specific tissue types due to the broad and relatively featureless profiles of the measured autofluorescence spectra.

Raman spectroscopy, on the other hand, is an optical modality that is well suited for characterizing the distinct biomolecular composition of a tissue sample. When a sample is irradiated with light,

the majority of the photons will be scattered elastically with the same amount of input energy, however, a small fraction is scattered inelastically, resulting in an energy loss from the incident light.[14] These energy shifts constitute a sample's Raman spectrum and are specific to the vibrational modes for a variety of different chemical bonds and functional groups. Since many biological molecules have distinguishably unique Raman spectra, the individual composition of a sample can be determined solely from the "biochemical fingerprint" of its Raman spectrum.

One particularly relevant biochemical change for cancer cells is an increase in the nucleic acid content associated with increased proliferation and genetic instability. This along with others such as changes in glycogen and collagen can all be detected by Raman spectroscopy.[15,16] Several research groups have exploited Raman spectroscopy for disease diagnosis in many organs, including the cervix,[17,18] bladder, prostate,[19] lung,[20] skin,[21,22] and GI tract.[23-25] In terms of sarcoma research, groups have been able to identify spectral features related to levels of polyunsaturation and tryptophan that could be used to differentiate between liposarcoma, rhabdomyosarcoma, Ewing sarcoma, neuroblastoma, and non-Hodgkin's lymphoma.[26,27] These studies, however, were conducted with *ex vivo* tissue samples and did not include comparisons to normal tissue.

Towards the goal of developing an optical system for the intraoperative assessment of tumor margins during STS excision, we evaluate the potential of near-infrared Raman spectroscopy for the automated differentiation of *in vivo* STS from the surrounding normal muscle and fat commonly encountered within a surgical tumor bed.

## 4.3 Materials and Methods

### *4.3.1 Intraoperative Raman Spectroscopy*

The portable Raman spectroscopy system used in this study consists of a custom-designed fiberoptic probe (EmVision LLC, Loxahatchee, FL) connected to a HoloSpec f/1.8i imaging spectrograph (Kaiser Optical Systems Inc., Ann Arbor, MI) equipped with a back-illuminated thermoelectrically cooled deep depletion charge coupled device (CCD) (Princeton Instruments, Trenton, NJ, SPEC-10:256BR). The hand held probe itself is approximately 15 cm in length with a diameter of about 6 mm and was designed to be as intuitive to grip as an office pen. At the tip of the probe is a single 400 μm diameter excitation fiber surrounded by seven 300 μm diameter collection fibers with inline long pass filtering to minimize interference signals from the probe itself. The tip is approximately 1 mm in diameter and covers a tissue area of about 0.79 $mm.^2$ A 785 nm diode laser (Innovative Photonics Solutions, NJ) was used as an excitation source and output power at the probe's tip was maintained at 80 mW. These parameters in combination with the probe's excitation and collection fiber geometry provides an effective depth interrogation of about 700 μm in to the tissue. Each measurement was collected within a wavenumber range of 550 to 1800 $cm^{-1}$ and a spectral resolution of 3.5 $cm^{-1}$ after binning. Wavenumber calibration was accomplished using standards based on acetaminophen, naphthalene, and a neon argon light source. Wavelength-dependent intensity response was calibrated using a secondary reflective standard to a NIST-certified quartz-tungsten-halogen lamp (Oriel Instruments, Irvine, CA, Model 63355).

After the STS mass was excised from the body, all ambient light within the operating room was turned off and/or covered. The attending surgeon would then acquire measurements by placing the

tip of the fiberoptic probe in direct contact with the regions of interest. From the tumor bed, distal measurements were acquired from control normal muscle and fat as visually identified by the surgeon. Afterwards, a small incision was made on the excised tumor and measurements were taken from the interior of the tumor before it was sent for post-operative histology. Five measurements at 3 second exposures were acquired from each tissue location with multiple sets of measurements collected at different locations in order to mitigate the effects of possible sampling errors.

All post-processing was performed in MATLAB (Natick, MA, 2014b). Each Raman spectrum was noise smoothed using a Savitzky-Golay filter and fitted to a $7^{th}$ order polynomial to remove background fluorescence.[28] To account for overall intensity variability, each spectrum was normalized to its mean spectral intensity across all wavenumbers.

### *4.3.2 Patient Recruitment and Outlier Detection*

Forty-two adult subjects undergoing STS excision were recruited under approval of the Vanderbilt University Institutional Review Board (#120813). Subject eligibility was determined during pre-operative evaluation by the surgical oncologists participating in the study, and informed written consent was obtained from each subject prior to measurements. Out of the 42 subjects enrolled, 28 were confirmed to have malignant tumors through post-operative histology. Outlier detection was performed within each tissue class in order to exclude measurements with aberrant spectra due to stray light, detector oversaturation, and insufficient contact of the probe to the sample. This was automatically performed through principal component analysis in which data that exceeded a preset Mahalanobis distance within the first 5 principal components were identified as outliers and excluded from further analysis.[29,30] After outlier detection, the following was retained for analysis:

normal fat from 34 subjects, normal muscle from 27 subjects, and tumor measurements from 21 subjects. At least one category of tissue was measured from each of the 42 enrolled subjects. A detailed listing of tissue types, number of subjects, and number of spectroscopic measurements following outlier detection can be seen in Table 4-1.

| Tissue Type | Patients | Measurements |
|---|---|---|
| Fat | 34 | 187 |
| Muscle | 27 | 171 |
| Well-Differentiated Liposarcoma | 7 | 98 |
| Undifferentiated Liposarcoma | 5 | 44 |
| Pleomorphic Liposarcoma | 2 | 24 |
| Myxofibrosarcoma | 2 | 25 |
| Epithelioid Sclerosing Fibrosarcoma | 2 | 20 |
| Well-Differentiated Liposarcoma with Myxoid Change | 1 | 10 |
| Dedifferentiated Liposarcoma | 1 | 15 |

Table 4-1: Recruitment table listing tissue type, number of patients, and number of measurements collected for this study following outlier detection.

### *4.3.3 Data Analysis*

Spectral feature reduction, predictive classifier training, and cross-validation was accomplished using a multivariate discrimination algorithm known as sparse multinomial logistic regression (SMLR). As a probabilistic multi-class model based on a Bayesian machine-learning framework of statistical pattern recognition, SMLR's iterative algorithm allows for the reduction of high dimensional Raman data into a small subset of spectral basis features that are weighted according

to their ability to successfully perform classification during training.[31] Theoretically, this should allow for a more robust and generalized model of tissue type discrimination. In order to avoid bias, each model was trained and tested using leave-one-subject out cross-validation where a decision threshold was placed at a minimum of 50% probability of class membership. A range of input SMLR parameters were tested to achieve the best classification while maximizing the sparsity of spectral features (basis functions). These include re-centering and rescaling each feature to have zero mean and unit variance, a direct kernel, no added bias term, a Laplacian prior, sparsity control of 0.1, and a non-component update rule. As the study was not powered for subtype differentiation, spectra from all STS subtypes were averaged to create a single diseased category during cross-validation.

A quantitative metric known as feature importance (FI) was utilized in order to assess the relative merit of the spectral features identified by SMLR for classification.[32] The value for FI, which ranges from 0 to 1, was defined as the product of the feature's cross-validation frequency percentage and its scaled weight. This helps to intuitively emphasize spectral features that are both heavily weighted for decisions and chosen consistently during the model's training.

### 4.4 Results

Average normalized Raman spectra for each tissue type measured in this study can be seen in Figure 4-1. For visual comparison, STS that are lipomatous in origin are arranged on the left, while STS that are non-lipomatous in origin are arranged on the right.

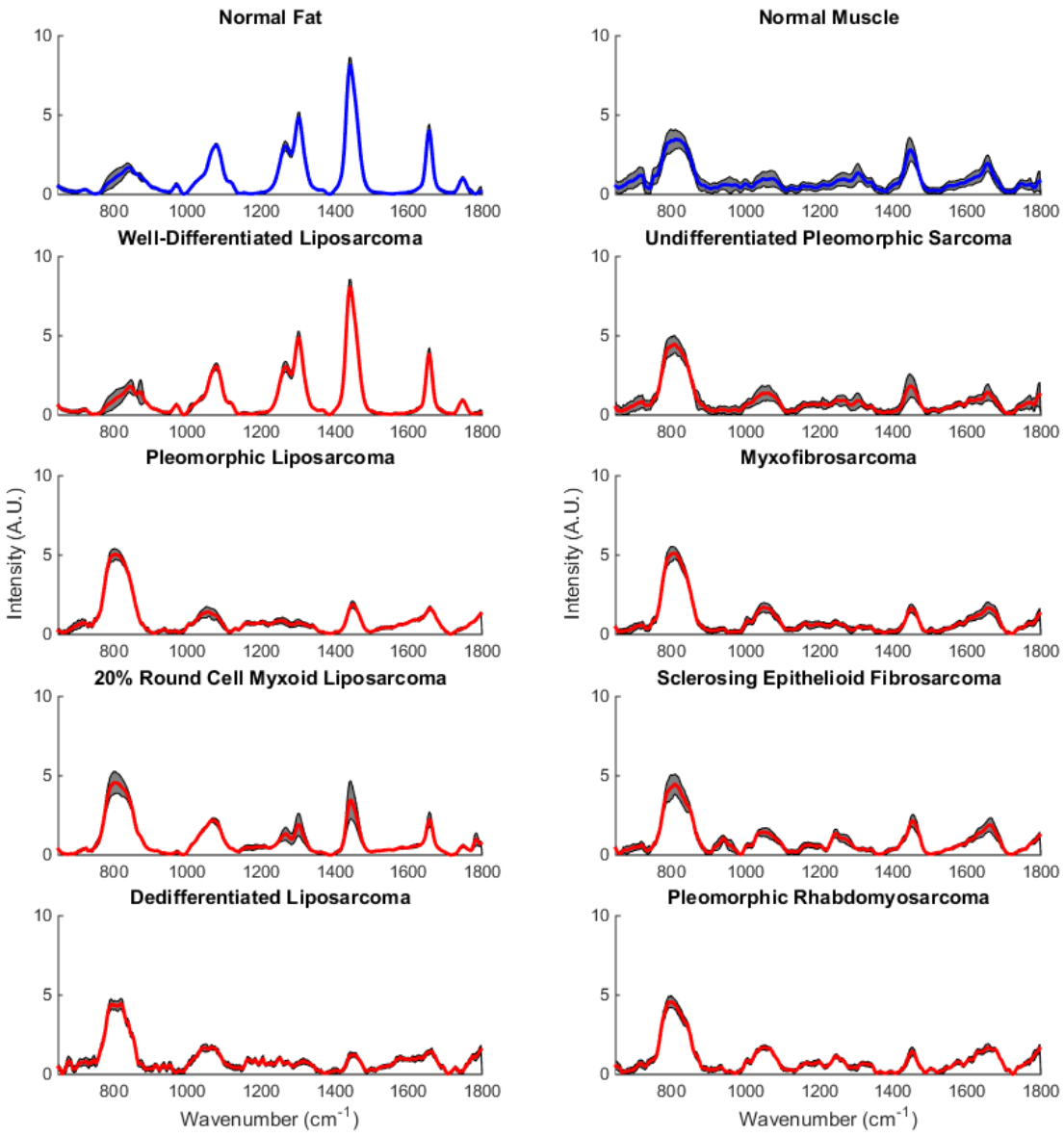


Figure 4-1: Average normalized Raman spectra for each tissue type. Normal tissues are plotted in blue while STS are in plotted red. Grey bands indicate standard deviation. For visual comparison, STS that are lipomatous in origin are arranged on the left while STS that are non-lipomatous in origin are arranged on the right.

Data from each labeled spectrum were subsequently used to develop a model for tissue type classification using SMLR and tested using leave-one-subject out cross-validation. Since muscle

and fat are the two most predominant normal tissues encountered within an STS tumor bed, there was a strong clinical motivation to test the SMLR based classification algorithm's performance at discriminating between normal muscle, normal fat, and STS. The performance from all individual tests can be seen in the confusion matrices in Table 4-2 and Table 4-3 where each row indicates a true category and each column indicates a model predicted category. Correctly classified measurements are highlighted in each table's diagonal. As seen in Table 4-2, SMLR's initial sensitivity and specificity for classifying STS from the surrounding normal muscle and fat were 59.6% and 91.69%, respectively. Upon further analysis of the results, it was apparent that 84 of the 98 well-differentiated liposarcoma measurements were misclassified as normal fat. When this specific subtype was excluded from analysis (Table 4-3), SMLR was able to classify STS from the surrounding normal muscle and fat with a sensitivity and specificity of 89.5% and 96.4%, respectively.

| | | ***Prediction*** | | | ***Performance*** | |
|---|---|---|---|---|---|---|
| | | **Fat** | **Muscle** | **STS** | **Sensitivity** | **Specificity** |
| ***Actual*** | **Fat** | 168 | 0 | 19 | 89.8% | 77.9% |
| | **Muscle** | 3 | 157 | 11 | 91.8% | 94.9% |
| | **STS** | 84 | 17 | 149 | 59.6% | 91.6% |

Table 4-2: SMLR normal fat vs normal muscle vs STS including well-differentiated liposarcomas

| | | ***Prediction*** | | | ***Performance*** | |
|---|---|---|---|---|---|---|
| | | **Fat** | **Muscle** | **STS** | **Sensitivity** | **Specificity** |
| ***Actual*** | **Fat** | 187 | 0 | 0 | 100% | 100% |
| | **Muscle** | 0 | 158 | 13 | 92.4% | 95.3% |
| | **STS** | 0 | 16 | 136 | 89.5% | 96.4% |

Table 4-3: SMLR normal fat vs normal muscle vs STS excluding well-differentiated liposarcomas

As part of the training process, SMLR was able to minimize the large dimensionality of each Raman spectrum into a reduced set of basis features for improved generalization during classification. After preprocessing, each measurement's spectrum originally consisted of 357 features associated with the Raman intensity at each wavenumber. When well-differentiated liposarcomas were included, the number of basis features required to differentiate normal fat, normal muscle, and STS was 177, 156, and 206, respectively. With the exclusion of well-differentiated liposarcomas, the number of basis features required were 107, 166, and 160, respectively.

A plot of averaged spectra with encoded regions of significant importance (FI > 0.30) can be seen in Figure 4-2. These features along with their quantitative importance and wavenumber assignments can be seen in Table 4-4 where the bands at 876, 1265, 1307, 1405, 1643 and 1786 $cm^{-1}$ were ascribed the highest importance for differentiating STS from normal muscle and fat.

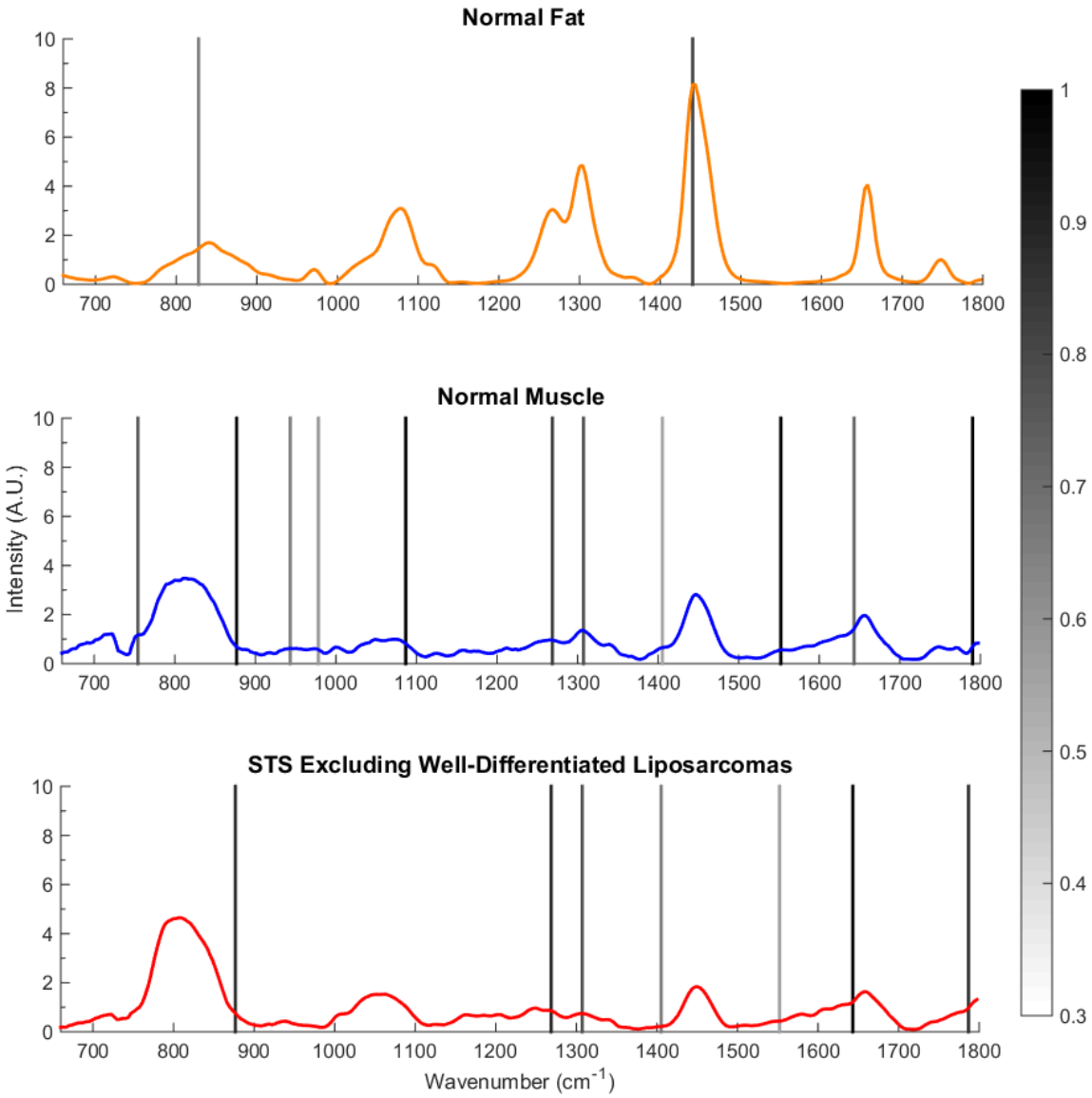


Figure 4-2: Average spectra of normal fat, normal muscle, and STSs excluding well-differentiated liposarcomas. Significant spectral features identified by SMLR for classification are highlighted with graded bands indicating their importance greater than a 0.30 threshold value.

| Raman Shift ($cm^{-1}$) | Feature Importance | Tissue Type | Assignment |
|---|---|---|---|
| 754 | 0.65 | Muscle | Tryptophan [33] |
| 827 | 0.50 | Fat | Tyrosine [15] |
| 876 | 0.95 / 0.83 | Muscle / STS | Hydroxyproline, Tryptophan [33,34] |
| 943 | 0.49 | Muscle | - |
| 978 | 0.40 | Muscle | Phosphorylated proteins and nucleic acids [15] |
| 1086 | 0.98 | Muscle | Phenylalanine, Phospholipids [17] |
| 1265 | 0.75 / 0.85 | Muscle / STS | Amide III (C-N) in Protein, =C-H in phospholipids [17] |
| 1307 | 0.67 / 0.67 | Muscle / STS | $CH_2$ in Lipids [34] |
| 1405 | 0.35 / 0.52 | Muscle / STS | $CH_3$ bending in Protein [15] |
| 1440 | 0.74 | Fat | $CH_2$ in Lipids [34] |
| 1552 | 0.96 / 0.37 | Muscle / STS | Tryptophan [17] |
| 1643 | 0.60 / 1.00 | Muscle / STS | Amide I C=O in Protein [17], C=C in Lipids |
| 1786 | 0.67 / 0.78 | Muscle / STS | - |

Table 4-4: Key SMLR spectral bands, feature importance, and assignment.

## 4.5 Discussion

To the best of our knowledge, this is the first ever near-infrared Raman spectroscopy study of STS within human subjects. From our measurements, we were able to develop a multivariate classification algorithm that can automatically identify spectral features that could be used to differentiate STS subtypes excluding well-differentiated liposarcomas from the surrounding

normal tissue. Raman spectroscopy is a feature-rich optical modality that has often been compared to "biological fingerprinting", and this abundance of information can be seen in the average normalized Raman spectra in Figure 4-1. For example, qualitative observation of normal fat spectra shows distinct narrow peaks at 1080, 1265, 1304, 1440, and 1657 $cm^{-1}$ due to the vibrational modes of the C-C, C-O, =C-H, $CH_2$, $CH_3$, and C=C groups in lipids.[17] These peaks are not as prominent within many of the normal muscle and STS subtypes, which instead have a stronger, although broader, band between 750 and 850 $cm^{-1}$ that encompasses a range of wavenumbers often associated with amino acids and nucleotides.[15,33,35] In addition, close similarities can be observed among many of the STS subtypes except for well-differentiated liposarcomas, which instead share strong spectral similarities to normal fat.

From the results presented in Table 4-2, it can be seen that the algorithm performs with high sensitivity for classifying normal tissue but much lower sensitivity for classifying STS. Upon further analysis, it was apparent that this disparity was due to one specific STS subtype, well-differentiated liposarcomas, which prior research has shown to have histological similarities to normal fat despite atypia.[36] In addition, these tumors are often non-homogenously distributed among large regions of normal adipose tissue, which may contribute to spatial sampling errors during measurements. Correspondingly, the Raman spectra of this STS subtype share close similarities to those of normal fat. As one of the most commonly diagnosed STS subtypes,[37] it constituted a large majority of our STS data set, which subsequently lowered the sensitivity and increased the number of basis features required for differentiating STS from normal fat. With the exclusion of well-differentiated liposarcomas from the study, SMLR was able to perform with a significant increase in sensitivity and decrease in required basis features as shown in Table 4-3. This level of performance despite some subtypes having only a single subject count and strict

cross-validation method suggests that these remaining STS subtypes may share common characteristic features.

From a clinical standpoint, the inability to differentiate well-differentiated liposarcomas from the surrounding normal fat has a negligible effect on surgical outcome as this particular subtype is one of the lowest grade sarcomas with the least metastatic potential.[38] Standard treatment using pre-operative MRI scans, marginal surgical excision, and post-operative radiation often have 5-year disease specific survival rates close to 95%.[38,39] However, well-differentiated liposarcomas still pose a considerable risk as they can further recur or progress into a much more aggressive de-differentiated state. Histologically, de-differentiated liposarcoma is defined as a biphasic neoplasm with one component of atypical lipomatous tumor and a second component of high grade tumor such as pleomorphic sarcoma.[40] Interestingly, this progression can be observed from the Raman measurements of lipomatous tumors presented in Figure 4-2, in which the well-differentiated liposarcomas begin with nearly identical spectra to normal fat. For subjects with later progression of de-differentiation such as the 20% round cell myxoid liposarcoma, the strong characteristic lipid peaks between 1080 and 1657 $cm^{-1}$ can be seen to significantly decrease as the peaks between 720 and 880 $cm^{-1}$ increase, possibly due to increased amino acid and nucleotide content associated with increased proliferation and genetic instability. Once in a de-differentiated state, the tumor has a qualitatively similar spectrum to that of the pleomorphic sarcomas.

As far as we are aware, the only other study of Raman spectroscopy in liposarcomas was carried out by Manoharan et al. in which they were able to observe a significant peak intensity increase at 1667 $cm^{-1}$ (C=C stretching) compared to 1442 $cm^{-1}$ (C-H bending) in their *ex vivo* liposarcoma samples compared to normal fat.[26] The increase of this ratio as the sample's mitosis rate increased

suggested that more aggressive liposarcomas could be identified by their levels of polyunsaturation. This was further validated by other groups studying liposarcomas with various metastatic potential using nuclear magnetic resonance spectroscopy.[41,42] The results from our study also follow a similar trend with the highest polyunsaturation increase in the dedifferentiated liposarcomas and lowest in the well-differentiated liposarcomas. However, the differences we observed and identified through SMLR went beyond a ratio of those two peaks, suggesting that there may be many other biochemical markers for STS and their progression.

In an effort to develop a robust model for differentiating the various tissue types based on their quantitative spectral differences, SMLR was also utilized to iteratively reduce the data into a smaller set of basis features essential for classification. With the exclusion of well-differentiated liposarcomas, the spectral features that were ascribed the highest importance for classifying STS were the bands at 1265, 1307, and 1405 $cm^{-1}$ along with peak shoulders at 876, 1643 and 1786 $cm^{-1}$. All of these distinguishing features were also used by SMLR to classify normal muscle to varying extent. The most important feature, the band at 1643 $cm^{-1}$ (FI = 1.0), is a shoulder of the peak often attributed to Amide I peptide bonds, and may be indicative of a major change in protein secondary structure within the malignant tumors.[17] This is further validated by the importance of the 1265 $cm^{-1}$ peak (FI = 0.85) attributed to Amide III peptide bonds, which is significantly decreased in the STS compared to normal muscle. Despite these changes in protein confirmation, STS had higher intensity spectra from 750 to 876 $cm^{-1}$ (FI = 0.83), which is a region dominated by signals from various amino acids and nucleotides. By using an SMLR based multivariate analysis approach, we were able to computationally identify differences with a robust algorithm that is not susceptible to subjectivity and overfitting regarding FI.

In terms of clinical impact, the results of this preliminary study suggests that an optical device based on Raman spectroscopy could allow for intraoperative tumor margin assessment. However, there are limitations that must be addressed before this technique can be translated into clinical use. As stated in the introduction, STS is a rare disease that accounts for less than 1% of all new cancers each year. This along with its vast heterogeneity in subtypes, makes it a relatively difficult disease to study *in vivo*. Yet despite the limited number of STS subtypes recruited for this study, the subtypes that that were measured constitute the ones most commonly encountered in the operating room.[2] With the exclusion of well-differentiated liposarcomas, common spectral features across various STS subtypes were found that could potentially be exploited for future margin assessment studies where there is much ambiguity in terms of tissue type composition. These findings could later be utilized in other Raman modalities such as spatially offset Raman spectroscopy, which has been demonstrated to perform depth sectioned measurements down to 8 mm.[43] Unlike the frozen section biopsies currently used in the operating room which may take 30 to 60 minutes, Raman spectroscopy could be utilized to non-destructively evaluate a single margin within seconds. The strength of Raman spectroscopy is its inherent biochemical specificity which can allow clinicians to rapidly and automatically identify abnormalities within margins that may require further excision or further adjuvant therapies. This would significantly improve the management of STS with respect to time, patient outcome, and healthcare costs.

## 4.6 Conclusion

The results of this study suggests that near-infrared Raman spectroscopy could be used to differentiate *in vivo* STS from the surrounding normal muscle and fat during surgeries. This was accomplished by developing a SMLR based classification algorithm that was then tested using

leave-one-subject out cross-validation. With the exclusion of well-differentiated liposarcomas that have strong spectral similarities to normal fat, the algorithm was able to perform with a sensitivity and specificity of 89.5% and 96.4%, respectively when classifying the remaining STS subtypes from normal muscle and fat. As part of the training process, the algorithm was able to reduce the high dimensional Raman spectra into a smaller set of basis features associated with significant differences in protein secondary structure and amino acid content that could be used to detect the presence of residual STS within a tumor bed.

## 4.7 Acknowledgements

This work was supported by the National Cancer Institute of the National Institutes of Health under Award Number F31CA200358, the Orthopaedic Research and Education Foundation / Musculoskeletal Tumor Society Clinical Research Grant in Orthopaedic Oncology, the Vanderbilt Orthopaedic Institute, and the Vanderbilt Medical Scholars Fellowship.

## 4.8 References


1. Demetri, G. D. *et al.* Soft tissue sarcoma. *Journal of the National Comprehensive Cancer Network : JNCCN* **8**, 630-674 (2010).
2. American Cancer Society. Cancer Facts & Figures 2016. (Atlanta: American Cancer Society, 2016).
3. Pritchard, D. J., Clayton, R. M. & Cunningham, W. L. Abnormal lens capsule carbohydrate associated with the dominant gene "small-eye" in the mouse. *Experimental eye research* **19**, 335-340 (1974).
4. Abraham, J. A., Baldini, E. H. & Butrynski, J. E. Management of adult soft-tissue sarcoma of the extremities and trunk. *Expert review of anticancer therapy* **10**, 233-248, doi:10.1586/era.09.193 (2010).
5. Atean, I. *et al.* Prognostic factors of extremity soft tissue sarcoma in adults. A single institutional analysis. *Cancer radiotherapie : journal de la Societe francaise de radiotherapie oncologique* **16**, 661-666, doi:10.1016/j.canrad.2012.05.021 (2012).
6. Blakely, M. L. *et al.* The impact of margin of resection on outcome in pediatric nonrhabdomyosarcoma soft tissue sarcoma. *Journal of pediatric surgery* **34**, 672-675 (1999).
7. Gronchi, A. *et al.* Status of surgical margins and prognosis in adult soft tissue sarcomas of the extremities: a series of patients treated at a single institution. *Journal of clinical oncology : official journal of the American Society of Clinical Oncology* **23**, 96-104, doi:10.1200/JCO.2005.04.160 (2005).
8. Alamanda, V. K. *et al.* Incomplete excisions of extremity soft tissue sarcomas are unaffected by insurance status or distance from a sarcoma center. *Journal of surgical oncology* **108**, 477-480, doi:10.1002/jso.23427 (2013).
9. Shives, T. C. Biopsy of soft-tissue tumors. *Clinical orthopaedics and related research* **289**, 32-35 (1993).
10. Carbajal, E. F. *et al.* Revealing retroperitoneal liposarcoma morphology using optical coherence tomography. *Journal of biomedical optics* **16**, 020502, doi:10.1117/1.3541789 (2011).

11. Eward, W. C. *et al.* A novel imaging system permits real-time in vivo tumor bed assessment after resection of naturally occurring sarcomas in dogs. *Clinical orthopaedics and related research* **471**, 834-842, doi:10.1007/s11999-012-2560-8 (2013).
12. Demos, S. G., Gandour-Edwards, R., Ramsamooj, R. & White, R. Near-infrared autofluorescence imaging for detection of cancer. *Journal of biomedical optics* **9**, 587-592, doi:10.1117/1.1688812 (2004).
13. Nguyen, J. Q. *et al.* Near-infrared autofluorescence spectroscopy of in vivo soft tissue sarcomas. *Optics letters* **40**, 5498-5501, doi:10.1364/OL.40.005498 (2015).
14. Smith, E. & Dent, G. *Modern Raman Spectroscopy – A Practical Approach*. (John Wiley & Sons, 2005).
15. Mahadevan-Jansen, A. & Richards-Kortum, R. R. Raman spectroscopy for the detection of cancers and precancers. *Journal of biomedical optics* **1**, 31-70, doi:10.1117/12.227815 (1996).
16. Mahadevan-Jansen, A., Patil, C. & Pence, I. in *Biomedical Photonics Handbook* (ed Tuan Vo-Dinh) 759-802 (CRC Press, 2014).
17. Mahadevan-Jansen, A. *et al.* Near-infrared Raman spectroscopy for in vitro detection of cervical precancers. *Photochemistry and photobiology* **68**, 123-132 (1998).
18. Mahadevan-Jansen, A., Mitchell, M. F., Ramanujam, N., Utzinger, U. & Richards-Kortum, R. Development of a fiber optic probe to measure NIR Raman spectra of cervical tissue in vivo. *Photochemistry and photobiology* **68**, 427-431 (1998).
19. Crow, P. *et al.* Assessment of fiberoptic near-infrared raman spectroscopy for diagnosis of bladder and prostate cancer. *Urology* **65**, 1126-1130, doi:10.1016/j.urology.2004.12.058 (2005).
20. Huang, Z. *et al.* Near-infrared Raman spectroscopy for optical diagnosis of lung cancer. *International journal of cancer. Journal international du cancer* **107**, 1047-1052, doi:10.1002/ijc.11500 (2003).
21. Lieber, C. A., Majumder, S. K., Ellis, D. L., Billheimer, D. D. & Mahadevan-Jansen, A. In vivo nonmelanoma skin cancer diagnosis using Raman microspectroscopy. *Lasers in surgery and medicine* **40**, 461-467, doi:10.1002/lsm.20653 (2008).

22. Sigurdsson, S. *et al.* Detection of skin cancer by classification of Raman spectra. *IEEE transactions on bio-medical engineering* **51**, 1784-1793, doi:10.1109/TBME.2004.831538 (2004).
23. Shetty, G., Kendall, C., Shepherd, N., Stone, N. & Barr, H. Raman spectroscopy: elucidation of biochemical changes in carcinogenesis of oesophagus. *British journal of cancer* **94**, 1460-1464, doi:10.1038/sj.bjc.6603102 (2006).
24. Shim, M. G., Song, L. M., Marcon, N. E. & Wilson, B. C. In vivo near-infrared Raman spectroscopy: demonstration of feasibility during clinical gastrointestinal endoscopy. *Photochemistry and photobiology* **72**, 146-150 (2000).
25. Molckovsky, A., Song, L. M., Shim, M. G., Marcon, N. E. & Wilson, B. C. Diagnostic potential of near-infrared Raman spectroscopy in the colon: differentiating adenomatous from hyperplastic polyps. *Gastrointest Endosc* **57**, 396-402, doi:10.1067/mge.2003.105 (2003).
26. Manoharan, R. *et al.* Raman spectroscopy for cancer detection: instrument development and tissue diagnosis. *Proceedings of SPIE* **2328**, 128-132 (1994).
27. Kast, R. *et al.* Differentiation of small round blue cell tumors using Raman spectroscopy. *Journal of pediatric surgery* **45**, 1110-1114, doi:10.1016/j.jpedsurg.2010.02.072 (2010).
28. Lieber, C. A. & Mahadevan-Jansen, A. Automated method for subtraction of fluorescence from biological Raman spectra. *Applied spectroscopy* **57**, 1363-1367, doi:10.1366/000370203322554518 (2003).
29. De Groot, P. *et al.* Application of principal component analysis to detect outliers and spectral deviations in near-field surface-enhanced Raman spectra. *Analytica Chimica Acta* **446**, 71-83 (2001).
30. Jackson, D. A. & Chen, Y. Robust principal component analysis and outlier detection with ecological data. *Environmetrics* **15**, 129-139 (2004).
31. Krishnapuram, B., Carin, L., Figueiredo, M. A. & Hartemink, A. J. Sparse multinomial logistic regression: fast algorithms and generalization bounds. *IEEE transactions on pattern analysis and machine intelligence* **27**, 957-968, doi:10.1109/TPAMI.2005.127 (2005).
32. Patil, C. A., Pence, I. J., Lieber, C. A. & Mahadevan-Jansen, A. 1064 nm dispersive Raman spectroscopy of tissues with strong near-infrared autofluorescence. *Optics letters* **39**, 303-306, doi:10.1364/OL.39.000303 (2014).

33. Erckens, R. J., Motamedi, M., March, W. F. & Wicksted, J. P. Raman spectroscopy for non-invasive characterization of ocular tissue: potential for detection of biological molecules. *Journal of Raman spectroscopy* **28**, 293-299 (1997).
34. Frank, C. J., McCreery, R. L. & Redd, D. C. Raman spectroscopy of normal and diseased human breast tissues. *Analytical chemistry* **67**, 777-783 (1995).
35. Schrader, B. *et al.* NIR FT Raman spectroscopy in medical diagnosis. *Journal of Molecular Structure* **348**, 293-296 (1995).
36. Evans, H. L., Soule, E. H. & Winkelmann, R. K. Atypical lipoma, atypical intramuscular lipoma, and well differentiated retroperitoneal liposarcoma: a reappraisal of 30 cases formerly classified as well differentiated liposarcoma. *Cancer* **43**, 574-584 (1979).
37. Singer, S. *et al.* Prognostic factors predictive of survival for truncal and retroperitoneal soft-tissue sarcoma. *Annals of surgery* **221**, 185-195 (1995).
38. Crago, A. M. & Singer, S. Clinical and molecular approaches to well differentiated and dedifferentiated liposarcoma. *Current opinion in oncology* **23**, 373-378, doi:10.1097/CCO.0b013e32834796e6 (2011).
39. Dalal, K. M., Kattan, M. W., Antonescu, C. R., Brennan, M. F. & Singer, S. Subtype specific prognostic nomogram for patients with primary liposarcoma of the retroperitoneum, extremity, or trunk. *Annals of surgery* **244**, 381-391, doi:10.1097/01.sla.0000234795.98607.00 (2006).
40. Goldblum, J. R., Weiss, S. W. & Folpe, A. L. *Enzinger and Weiss's soft tissue tumors*. (Elsevier Health Sciences, 2013).
41. Millis, K. *et al.* Classification of human liposarcoma and lipoma using ex vivo proton NMR spectroscopy. *Magnetic resonance in medicine* **41**, 257-267 (1999).
42. Singer, S., Millis, K., Souza, K. & Fletcher, C. Correlation of lipid content and composition with liposarcoma histology and grade. *Annals of surgical oncology* **4**, 557-563 (1997).
43. Matousek, P. & Stone, N. Development of deep subsurface Raman spectroscopy for medical diagnosis and disease monitoring. *Chemical Society reviews* **45**, 1794-1802, doi:10.1039/c5cs00466g (2016).

# CHAPTER 5

# DEVELOPMENT OF A MODULAR FLUORESCENCE OVERLAY TISSUE IMAGING SYSTEM FOR QUANTITATIVE WIDE-FIELD INTRAOPERATIVE SURGICAL GUIDANCE

John Quan Nguyen[1], Melanie McWade[1], Giju Thomas[1], Bryce T. Beddard[1], Jennifer L. Herington[2], Bibhash C. Paria[2], Herbert S. Schwartz[3], Jennifer L. Halpern[3], Ginger Holt[3], Anita Mahadevan-Jansen[1*]

[1]Vanderbilt University, Biophotonics Center, Nashville, TN, USA, 37232

[2]Vanderbilt University, Department of Pediatrics, Nashville, TN, USA, 37232

[3]Vanderbilt University Medical Center, Department of Orthopaedic Surgery and Rehabilitation, Nashville, TN, USA 37232

The work comprised in this chapter is currently under review as:

"Development of a modular fluorescence overlay tissue imaging system for quantitative wide-field intraoperative surgical guidance"

*Journal of Medical Imaging*

## 5.1 Abstract

Fluorescence imaging is a well-established optical modality that has been used to localize and track fluorophores *in vivo* and has demonstrated great potential for surgical guidance. Despite the variety of fluorophores currently being researched, many existing intraoperative fluorescence imaging systems are specifically designed for a limited number of applications. Here, we present a modular wide-field fluorescence Overlay Tissue Imaging System (OTIS) for intraoperative surgical guidance that is comprised of commercially available standardized components. Its modular layout allows for the accommodation of a broad range of fluorophores, field-of-views (FOV), and spatial resolutions while maintaining an integrated portable design for intraoperative use. Measurements are automatic, quantitative, and feature a real-time projection overlay technique that intuitively displays fluorescence maps directly onto a 15 x 15 $cm^2$ FOV from a working distance of 35 cm. At a 20 ms exposure time, 10 μM samples of indocyanine green could be measured with high signal-to-noise and was later tested in an *in vivo* mouse model before finally being demonstrated for intraoperative autofluorescence imaging of human soft tissue sarcoma margins. The system's modular design and ability to enable quantitative naked-eye visualization of wide-field fluorescence allows for the flexibility to adapt to numerous clinical applications and can potentially extend the adoption of fluorescence imaging for intraoperative use.

## 5.2 Introduction

Fluorescence imaging is a well-established optical modality that spatially measures the spectral emissions arising from fluorescent chemical molecules when excited by a light source. Fluorophores can be naturally occurring or synthesized and can span a wide range of excitation and emission wavelengths. Over the past two decades, there has been many major advances regarding the utilization of florescence imaging for non-invasive diagnosis and surgical guidance. Exogenous ultraviolet (UV) to near-infrared (NIR) contrast agents such as 5-aminolevulinic acid (5-ALA) induced protoporphyrin IX (PpIX) and FDA-approved indocyanine green (ICG) have demonstrated a great potential for visualizing angiographic applications, improving the gross resection of malignant gliomas, and maximizing the survival benefits associated with surgical excisions in which tissue conservation is a high priority.[1-6] Conjugation of visible to NIR dyes such as Cyanine5.5, DyLight 680, and IRDye 800CW with tumor specific peptides and antibodies can even allow for the development of specialized probes capable of improving the detection of cancers *in vivo* and has been explored in various animal models thus far.[2,7-11] In addition, UV to visible autofluorescence has been demonstrated to differentiate between normal and neoplastic tissue based on the changes of endogenous fluorophores and environment related to disease progression.[12,13] This has been researched as a possible diagnostic tool in various organ systems including the brain,[14-17] bronchus,[18] colon,[19] cervix,[20] bladder,[21] esophagus,[22] skin,[23] breast,[24] and arterial wall.[25] Recently, probe-based NIR autofluorescence spectroscopy has been shown to have potential for differentiating soft tissue sarcomas (STS) from the surrounding normal muscle and fat within a surgical bed without the use of any exogenous contrast agents.[13] This in itself can allow for the detection of residual tumors during surgical resection and help decrease the need for

additional therapies such as postoperative radiation and/or re-excision. With an extensive variety of applications and fluorophores each with their own unique optical properties that span a wide range of wavelengths, there currently does not exist a single quantitative fluorescence imaging system that can be conveniently configured to measure a broad range of fluorophores over a wide field of view (FOV) while being optimized for use in an operating room setting.

Fluorescence imaging at its core consists of three primary components: a light source for fluorophore excitation, an imaging sensor for collecting light emission, and a set of optical filters for selective filtering of the emitted light. Despite the relative simplicity in hardware, there are many design criteria that must be accounted for in order to translate a laboratory research system into an intraoperative environment. These include considerations of working distance, FOV, sensitivity, quantitativeness, physical size, ability to work in a sterile environment, and software for control and data processing. Additionally, emphasis must also be directed towards ergonomics and the ability to relay accurate spatial fluorescence information back to the surgeon in a manner that is intuitive, real-time, and non-obtrusive to normal surgical workflow. It is estimated that 30-40% of errors in surgical imaging are due to interpretive errors related to lack of image context, time consuming image analysis, and the need to mentally co-register images displayed on a distant monitor to the actual surgical bed.[26,27] As a whole, these challenges lessen the effectiveness of image-guided surgery and it is crucial that many of these design constraints be addressed for intraoperative fluorescence imaging to gain widespread use in the operating room.

Currently there are numerous FDA 510(k) approved clinical fluorescence imaging systems available commercially with varying feature sets related to illumination wavelengths, emission collection wavelengths, sensitivity, cost, ergonomics, optics, and image output.[28,29] Lower cost

small profile systems such as the Hamamatsu PDE neo are capable of hand-held operation but can only provide qualitative images at relatively small FOVs (~10 x 6.7 $cm^2$), low pixel dimensions (640 x480), short working distances (~25 cm), and low bit-depth (8 bit).[29] More widely utilized devices such as the higher end Novadaq SPY Elite articulated arm system are capable of measurements at similar FOVs, but with higher pixel dimensions (1024 x 768), and longer working distances (~34 cm).[29] Newer research grade devices that are not FDA-approved such as the Curadel Lab-Flare articulated arm system are much more fully featured and can operate at large FOVs (~25.3 x 25.3 $cm^2$), high pixel dimension (1024 x 1024), long working distances (~45 cm), and is capable of simultaneous multifluorohpore imaging over a range of distinct wavelengths from 470 to 760 nm.[28] Some devices such as the Quest Spectrum feature methods for background light corrected measurements while many others do not.[29] Despite variations in terms of cost and features, many are qualtiative, dependent on remote monitors for displaying fluorsence maps, and are hardware confined to a small number of excitation and emission windows. As intraoperative needs are continually changing along with the discovery of newer fluophores and applications, these strict hardware limitations can hinder the clinical adoption of fluroescence imaging as a whole.

Here we present a modular fluorescence Overlay Tissue Imaging System (OTIS) aimed at quantitative wide-field intraoperative surgical guidance. Unlike most commercial systems which rely on remote monitors, the device presented here works in real time to project fluorescence maps directly on to the surgical field in a manner similar to vein finders, an intraoperative system from the Akers group,[30,31] and a benchtop system described by Gan *et al.*[32] In addition to providing a surgeon with intuitive feedback, the system is built entirely from standardized commercial components and features a modular layout that can allow the system's FOV, spatial resolution,

working distance, and spectral range to be easily customized depending on application. Measurements are quantitative, automatic, and features background light correction that allows for use in low ambient lighting environments. The system was validated in preliminary *ex vivo* studies using ICG and tested in an *in vivo* mouse model before being demonstrated for intraoperative autofluorescence imaging in human patients undergoing STS resections.

## 5.3 Materials and Methods

### *5.3.1 Fluorescence Overlay Tissue Imaging System (OTIS)*

A diagram illustrating the basic design and layout of the imaging head along with a photograph of the OTIS setup can be seen in Figure 5-1.

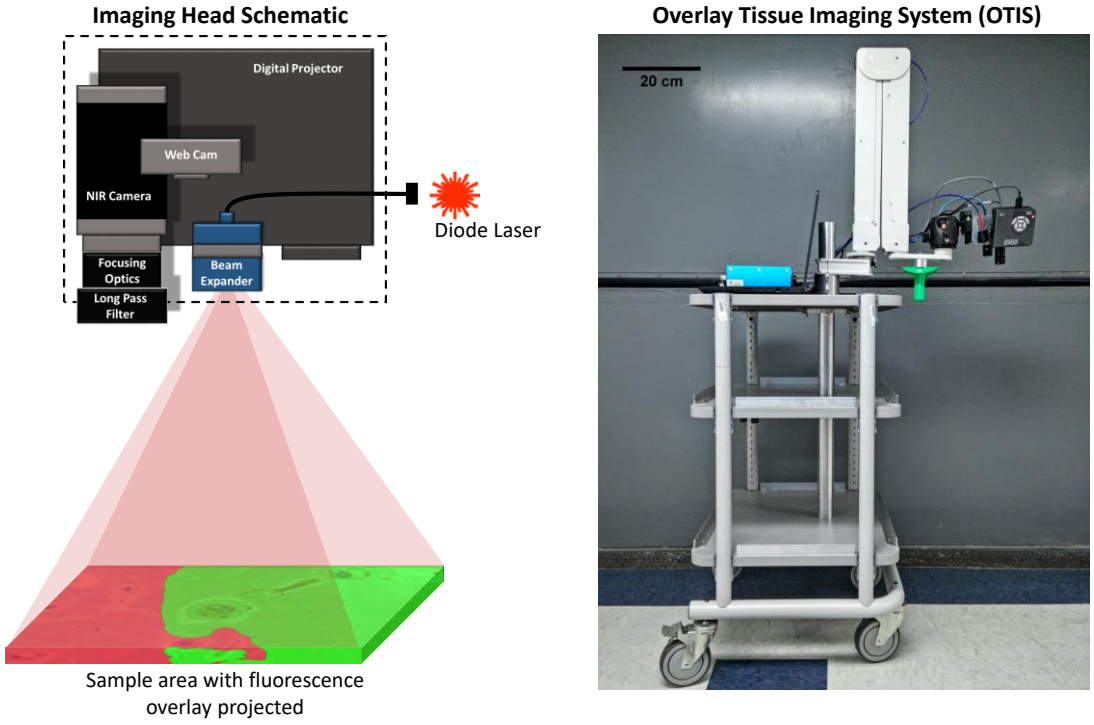


(a) (b)

Figure 5-1: (a) Diagram illustrating the basic design and layout of the OTIS imaging head. (b) Image of the entire fluorescence imaging system including the transport cart and articulated arm.

For studies presented in this paper, the device's excitation source was fitted with a 785 nm diode laser (Innovative Photonic Solutions I0785MM0500MS, Monmouth Junction, NJ) fiber coupled via a SMA905 connector to a 785 nm notch filter (LL01-785, Semrock Inc., Rochester, NY) and a double concave lens for beam divergence. Image collection was accomplished using a 12-bit NIR complementary metal-oxide-semiconductor (CMOS) camera (Baslar AG acA1300-60gmNIR, Ahrensburg, Germany) equipped with a c-mounted manual iris lens (Ricoh FL-CC1214A-2m, Tokyo, Japan) and a c-mounted machine vision 830 nm long pass filter (Midwest Optical Systems Inc. LP830, Palatine, IL). Unlike traditional coated interference filters, this

particular hybrid long pass filter design also includes an absorptive filter glass at the leading edge of the filter passband that helps to minimize short-shifting wavelength aberrations caused by non-normal angels of incidence[33] when imaging large FOVs as seen in Figure 5-2.

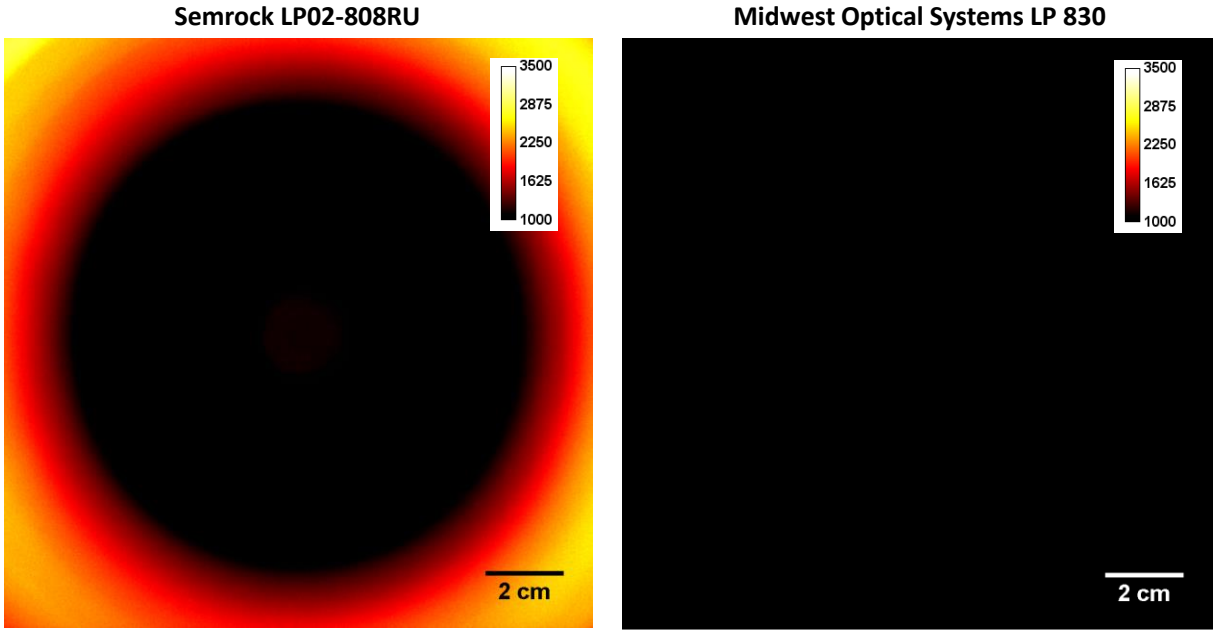


(a) (b)

Figure 5-2: Filter spectral artifacts when collecting at non-normal angles of incidence during wide-field imaging. (a) Example of a traditional thin-film interference filter. (b) Example of a hybrid long pass filter under the same imaging conditions.

Color images were collected using a webcam (Logitech HD Webcam C930e, Lausanne, Switzerland) and fluorescence projection overlay was accomplished using a 300 lumen digital light projector (AAXA Technologies P5, Irvine, CA). The system as a whole is controlled with a 64-bit laptop (Intel Core i7-6700HQ, Santa Clara, CA) , running a custom MATLAB (MathWorks, Natick, MA) graphical user interface (GUI) suite that utilizes the graphics processing unit (GPU)

(NVIDIA Geforce GTX 960M, Santa Clara, CA) for simultaneous capture, data processing, and projection overlay in real time. For intraoperative applications, the imaging head is attached to a ball mount that allows it to be positioned at any angle required during surgery. The mount is connected to a double articulated arm supported by a mobile cart that transports the entire system. The imaging head can be shielded using a 3D printed enclosure and wrapped in a universal c-arm sterile drape without overheating. Additionally, a machined slot on the arm allows for the insertion of a disposable sterile handle similar to a surgical microscope. In its most compact transport configuration, the imaging system occupies a space of about 160 x 64 x 55 $cm^3$.

With the configuration described above, the OTIS is capable of measuring a 15 x 15 $cm^2$ FOV at a pixel dimension of 1024 x 1024 and a working distance of 35 cm. The optical irradiance at this distance is approximately 0.7 $mW/cm^2$. As all the optical components utilize standardized SMA905 and C-Mount threading, each major element can be modified and replaced to best suit different application needs.

### *5.3.2 Flat Field Reference Calibration*

Prior to imaging, the system must be calibrated in order to acquire quantitative measurements and to correct for any system response due to spatial variations in source illumination and other optical aberrations. This is accomplished by acquiring a single reference measurement from a custom designed 20 x 20 x 5 $cm^3$ polydimethylsiloxane phantom consisting of pheophorbide-a (Sigma-Aldrich, St. Louis, MO) as a visible to NIR fluorophore, titanium dioxide as a scattering agent, and India ink as an absorber.[34] Optical property homogeneity and long-term stability of the phantom was validated using a probe based spectrometer described in previous studies.[13,35] For

each subsequent measurement, flat field correction is accomplished through the following equation:

$$C(x,y) = \frac{<R>}{R(x,y)} * I(x,y) \qquad \text{Equation 5-1}$$

Where *C* is the corrected image, *R* is the reference measurement, and *I* is the raw sample image. The correction factor, <R>/R(x,y), is a ratio of the reference's total intensity average to each pixel's raw intensity.

### *5.3.3 Imaging Workflow*

Depending on the application, the signal-to-noise (SNR) performance can be increased through background subtraction of ambient light and by averaging multiple frames of images at the cost of longer total acquisition times. Fluorescence thresholding is automated using a method described by Otsu[36] based on a user defined threshold value, and can be simultaneously projected back on the sample's surface in bright green at the same rate that images are being acquired. Green was chosen for the overlay image because it provides a stark visual contrast against tissue and does not contribute to the NIR fluorescence measurements. Single snapshot fluorescence measurements can also be recorded along with color and gray scale images by utilizing the projector's white light as illumination.

### *5.3.4 ICG Sensitivity Test*

In order to characterize the sensitivity of the fluorescence imaging system, ICG was diluted with water at concentrations of 10, 7, 5, 3, 1, 0.75, 0.5, 0.25, 0.10, 0.05, and 0 μM. At a volume of 250 μl per well, these values are equivalent to 7.75, 5.42, 3.87, 2.32, 0.77. 0.58, 0.39, 0.19, 0.08, 0.04, and 0 μg/ml respectively. Each sample was spaced about 2 cm apart from each other to prevent

signal contamination from the surrounding wells and imaged at a relatively short exposure time of 20 ms in order to prevent the CMOS detector from oversaturating.

### *5.3.5 Mouse ICG Tail-Vein Injection*

A total of four adult (8-12 week old) female CD1 wild-type mice (Charles River Laboratories, Wilmington MA) with average weights of 40 g were used in an ICG tail vein injection study aimed at validating the imaging system's performance *in vivo*. Housing and care for the animals were performed in accordance with the regulations described in the NIH Guide for the Care and Use of Laboratory Animals, and all experiments were performed under approval from the Vanderbilt University Medical Center's Institutional Animal Care and Use Committee (IACUC #M/15/111).

During this study, each mouse was anesthetized through a nose-cone delivery of 2% isoflurane mixed with 100% oxygen using a precision vaporizer (E-Z Anesthesia, Palmer, PA). Each anesthetized mouse was given a tail vein injection of 0.1 ml ICG at 10 μM concentration, which is approximately equivalent to a 0.5 mg/kg dosage and is well below the 2.0 mg/kg threshold for FDA-approved human clinical applications.[37] Ten minutes after imaging of tail vein injections, each mice was then euthanized using a primary overdose of isoflurane and subsequent cervical dislocation. Postmortem images of the liver were then acquired after exposing the abdominal cavity in order to confirm each successful tail vein injection.

### *5.3.6 Intraoperative STS Tumor Bed Autofluorescence Imaging*

In order to demonstrate the system's intraoperative performance, 15 subjects undergoing STS excision were recruited under approval of the Vanderbilt University Institutional Review Board (IRB #120813). Subject eligibility was determined during preoperative evaluation by a surgical oncologist and informed written consent was obtained from each subject prior to measurements.

Along with images of the exposed tumor mass, measurements were also acquired from within each patient's surgical cavity.

## 5.4 Results

### *5.4.1 Spatial Resolution*

The OTIS's maximum resolvable power was tested using a 1951 United States Air Force resolution test chart. This particular test target consist of reference bar patterns with well-defined thickness and spacings. By identifying the largest group and element pair of non-distinguishable bars, the maximum resolving power of a given optical system can be determined. The results of this test can be seen in Figure 5-3 in which two c-mounted iris lenses (12 mm and 50 mm focuses) equipped with 830 nm long-pass filters were tested under white light illumination. Line plots of each pattern's gray scale intensities are also included to better validate the resolving power limits. The 12 mm focus lens was found to have a maximum spatial resolution of 250 μm (Group 1, Element 1) and a maximum FOV of 15 x 15 $cm^2$ while the 50 mm focus lens was shown to have a maximum spatial resolution of 78.75 μm (Group 2, Element 5) and a maximum FOV 4.3 x 4.3 $cm^2$.

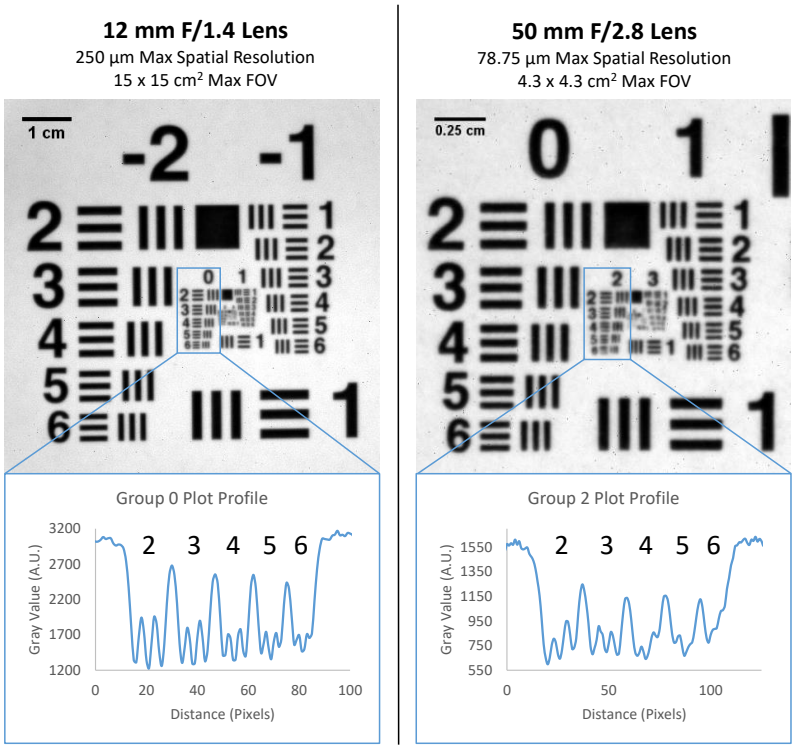


(a) (b)

Figure 5-3: Resolving power of the fluorescence imaging system as tested by a United States Airforce 1951 resolution test chart with two different iris lens. Top images are of the targets, while bottom images are the line plots through each element of a particular target group. Limits of resolving power was determined by the largest group and element pair in which the spacing pattern is no longer discernable within the line plot. (a) Resolving power under a 12 mm focal length lens. (b) Resolving power under a 50 mm focal length lens.

### *5.4.2 Reference Calibration*

Flat-field correction was validated using two small pheophorbide-a phantoms with slightly different optical properties confirmed with a probe based spectrometer.[13,35] The samples were imaged in the center of the 15 x 15 cm$^2$ FOV and then positioned on the far edge for another measurement. The results of the flat-field correction method can be seen in Figure 5-4. Before

calibration, the samples measured at the FOV's far edge exhibited a 38% decrease in fluorescence intensity than when measured at the FOV's center. After calibration using Equation 5-1, the samples measured at the FOV's far edge exhibited a 2% difference than when measured at the FOV's center. An intensity cross section of the imaging surface before and after calibration can also be seen in Figure 5-5.

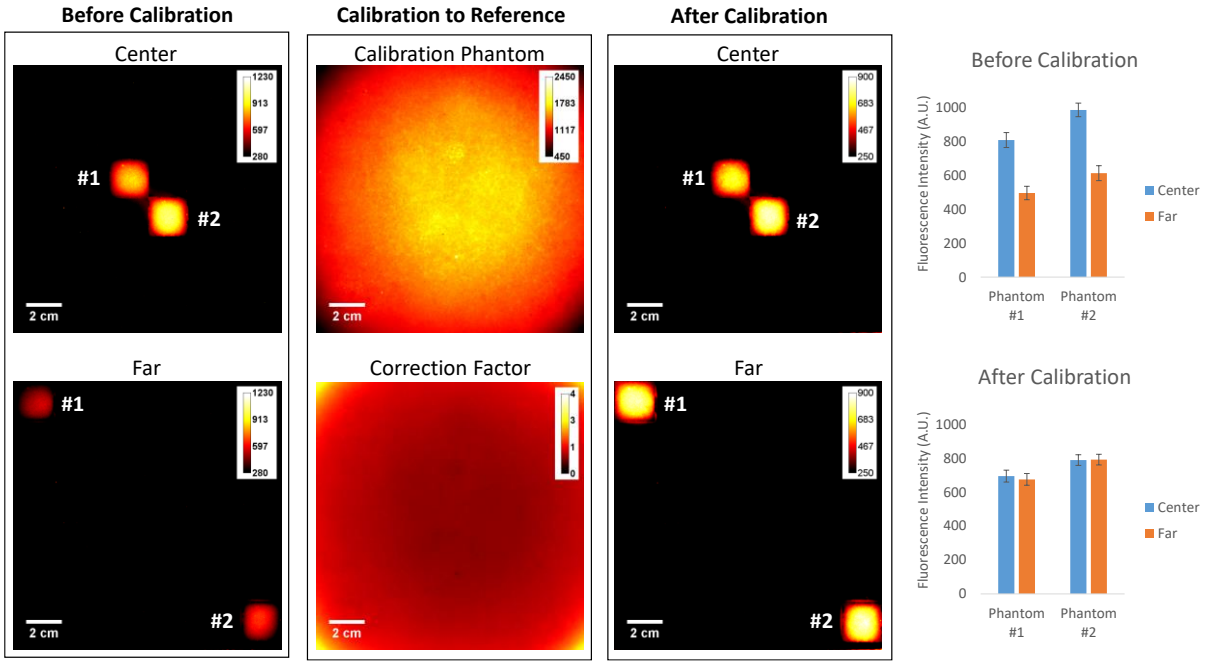


(a) (b) (c) (d)

Figure 5-4: Validation of flat-field correction: (a) Raw fluorescence images of two miniature phantoms measured at the center and far edge of the 15 x 15 $cm^2$ FOV prior to calibration. (b) Raw image of the reference calibration phantom (top) and the correction image derived from it (bottom). (c) Fluorescence images of the two miniature phantoms after calibration. (d) Bar plots of averaged sample intensities with standard deviations.

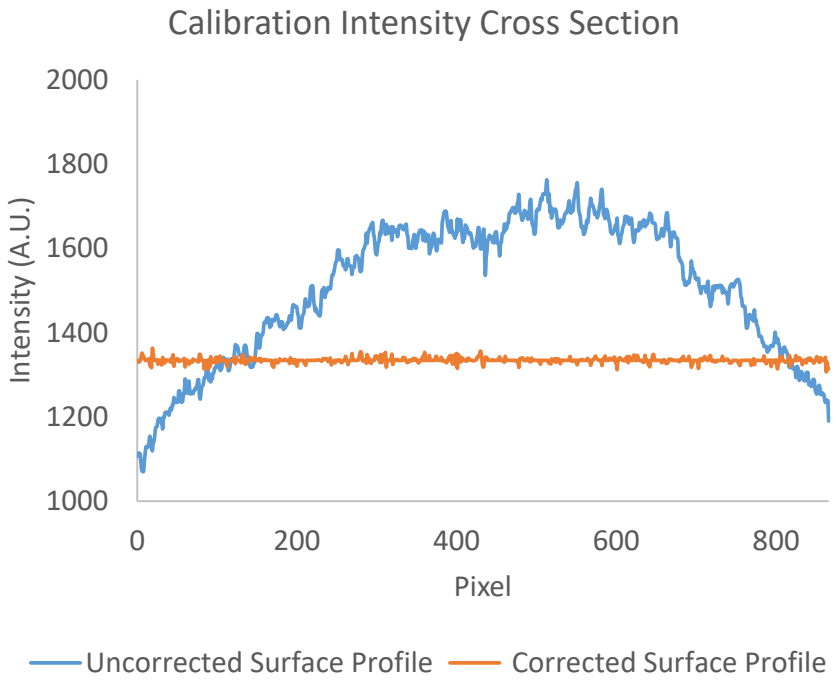


Figure 5-5: Line plot cross section of a measured surface before and after reference calibration.

### *5.4.3 ICG Sensitivity*

The results of the ICG sensitivity test can be seen in Figure 5-6 where the ICG fluorescence signal is observed to decrease with lower concentrations following a second degree polynomial ($R^2$ = 0.99). In terms of a signal-to-noise ratio (SNR) as defined as the ratio of sample mean intensity to the standard deviation of the background noise, a clinically relevant ICG concentration of 10 µM demonstrated a SNR of 531 as seen in Figure 5-6(d). At the lowest concentration of 0.05 µM, the signal could still be measured with a SNR of 5.6 at an exposure time of 20 ms.

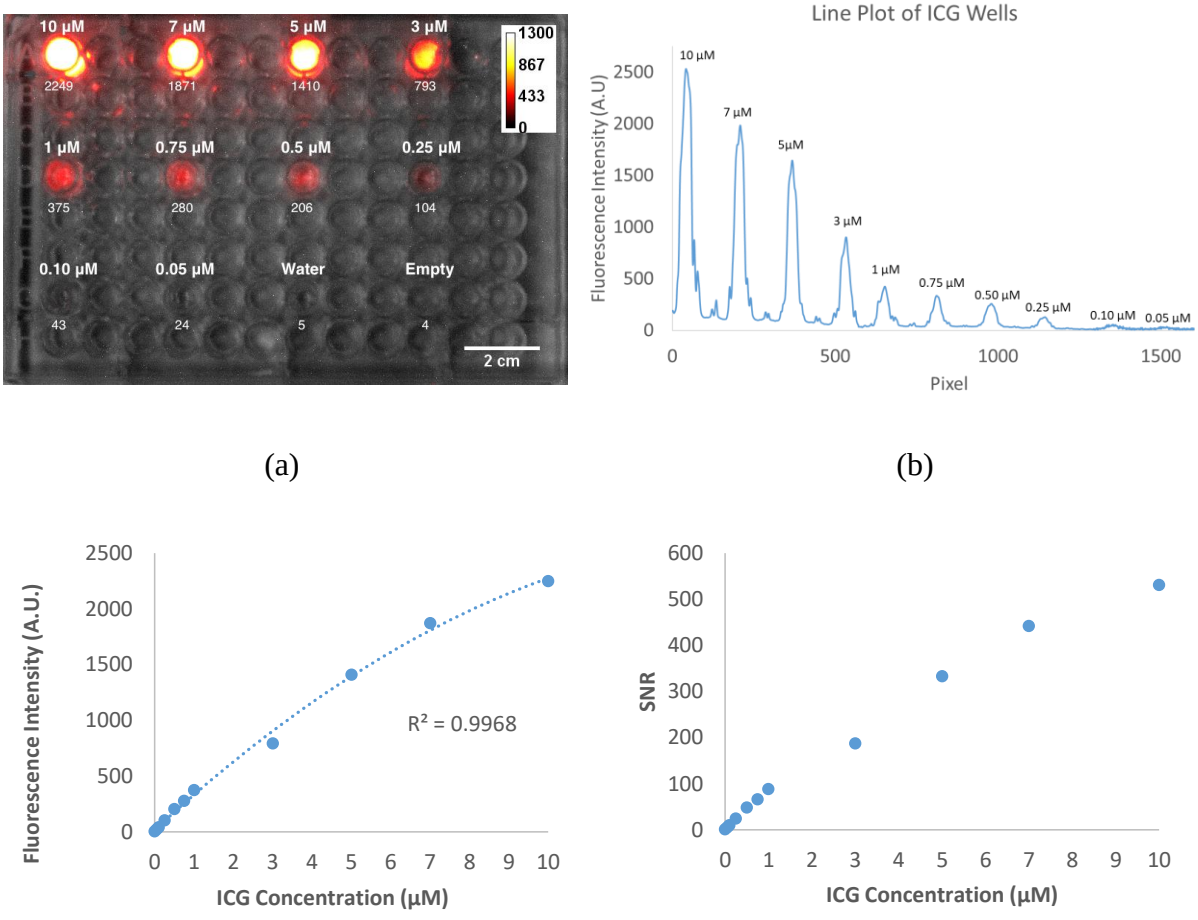


(a) (b)

(c) (d)

Figure 5-6: Results of ICG sensitivity tests using a 785 nm excitation and 800 nm long-pass filter configuration at a 20 ms exposure. (a) Combined grayscale and NIR fluorescence intensity image of ICG samples, their concentrations (top), and averaged intensity values (bottom). (b) Intensity line plots across each well with ICG concertations labeled at the top. (c) Plot of average ICG fluorescence intensity at each measured concentration of ICG. (d) Plot of SNR at each measured concentration of ICG.

### *5.4.4 Projection Overlay*

To demonstrate the ability of OTIS for simultaneous acquisition and projection overlay, 30 gelatin capsules filled with pheophorbide-a were scattered in random orientations across a 15 x 15 $cm^2$ area and imaged by the system along with an *ex vivo* STS tumor margin. After thresholding, the binary image was then cast back onto the FOV using the digital light projector as seen in Figure 5-7. In both cases, fluorescence measurements and data processing were accomplished simultaneously and projected onto the sample in real time. At a 30 ms exposure time, the acquisition and projection frame rate is approximately 33 frames per seconds (fps). Additional tests were also able to demonstrate a projection accuracy within 0 to 1 mm and a maximum projection resolution of approximately 2 mm when imaging at the 35 cm distance focal plane.

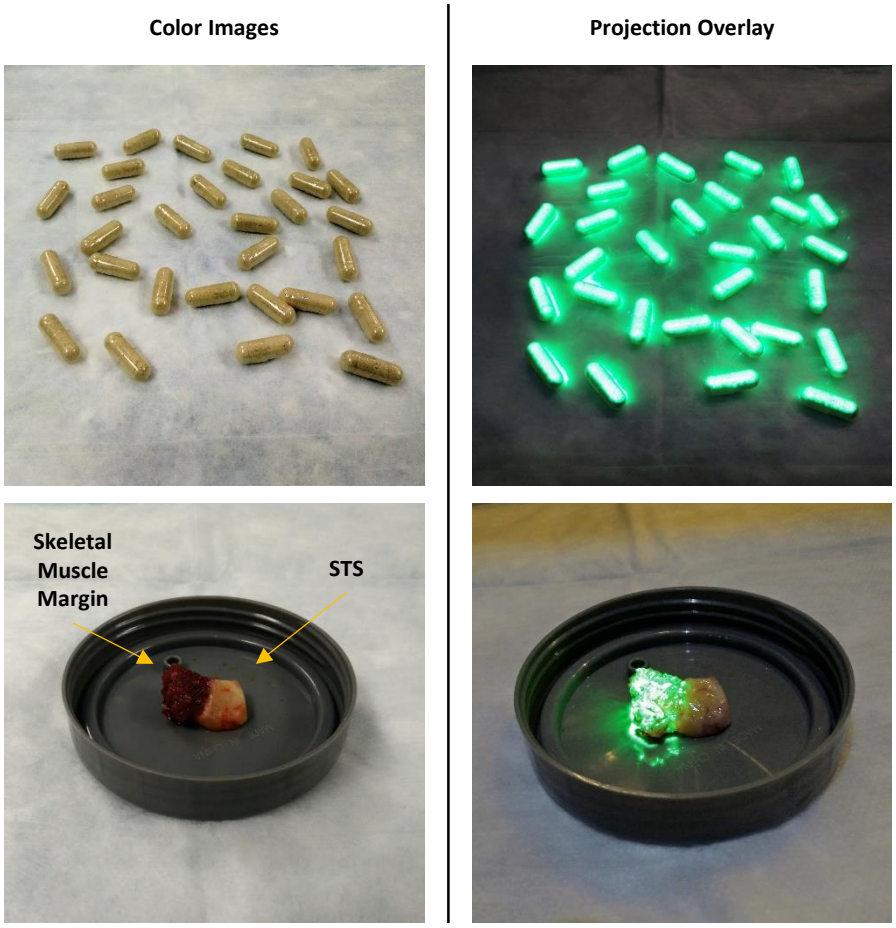


(a) (b)

Figure 5-7: Example of real time projection overlay at 33 fps using a random arrangement of pheophorbide-a capsules within a 15 x 15 $cm^2$ area (top) and an *ex vivo* STS tumor margin (bottom). (a) Color images before projection overlay (b) Projection overlay in effect.

### *5.4.5 Mouse ICG Tail Vein Injection*

An ICG tail injection experiment was carried out to demonstrate the performance of OTIS in an *in vivo* animal model. In these experiments, each mouse was given a tail vein injection of 0.1 ml ICG at 10 μM concentration prior to imaging at a 30 ms exposure time. Ten minutes after tail vein

imaging, the mouse was then euthanized and postmortem images of the liver were acquired after opening the abdominal cavity in order to confirm the success of each injection by imaging the final accumulation of ICG in the liver. Representative results of this study can be seen in Figure 5-8 with similar outcomes in all mice. With the background set as an adjacent non-fluorescing portion of the mouse, the SNR of the ICG tail vein injection measurement was approximately 22.9 while the SNR of the postmortem liver measurement was approximately 90.7.

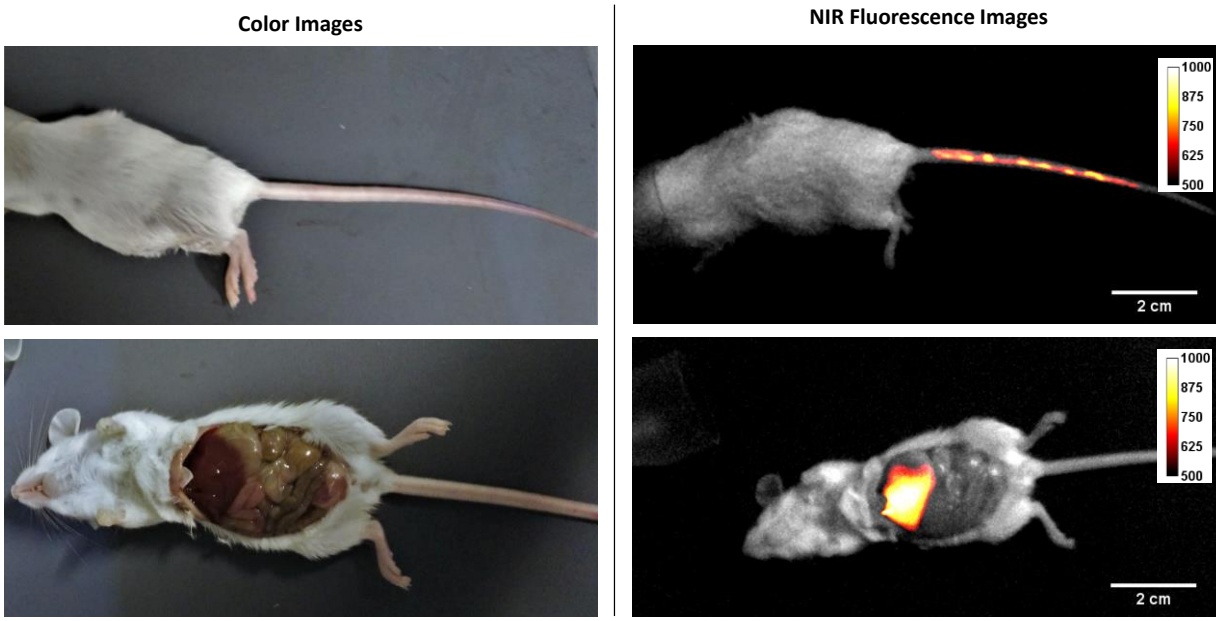


(a) (b)

Figure 5-8: Mouse ICG tail-vein injection study as measured by the fluorescence imaging system at a 30 ms exposure. Images at the top correspond to a representative ICG tail vein injection measurement, while images at the bottom correspond to post-mortem abdominal imaging of ICG accumulation in the liver within the same mouse after 10 min. (a) Color images of mouse tail and abdominal cavity. (b) NIR fluorescence images of ICG injected mouse tail (SNR: 22.9) and abdominal cavity with ICG accumulation within the liver. (SNR: 90.7)

### *5.4.6 In vivo Soft Tissue Sarcoma Imaging*

The fluorescence imaging system was finally demonstrated in an intraoperative environment through measurements of human STS and tumor bed autofluorescence acquired during STS excision surgeries. No exogenous contrast agents were utilized. Following excision of the STS tumor mass from the body, images were collected from the tumor bed *in vivo* before further measurements were acquired from the resected mass with the tumor exposed. Figure 5-9(a) shows a color image of an intraoperatively excised leiomyosarcoma mass with the underlying tumor exposed from its surrounding skeletal muscle margin, and Figure 5-9(b) shows the NIR autofluorescence image of the same tumor mass. Here, a noticeably strong signal can be observed from the skeletal muscle margin while the exposed tumor itself exhibits a significantly decreased signal. In addition to the STS mass, an example of tumor bed autofluorescence imaging can be seen in Figure 5-10. Figure 5-10(a) shows a white light image of the right thigh tumor bed while its NIR autofluorescence map can be seen in Figure 5-10(b). Again, skeletal muscle is observed to have high signal compared to everything else in the tumor bed including fat, bone, skin, and the blood vessel sheath running through the center of the thigh. Figure 5-10(c) shows a color image of the tumor bed and Figure 5-10(d) shows the real-time projection overlay technique in effect.

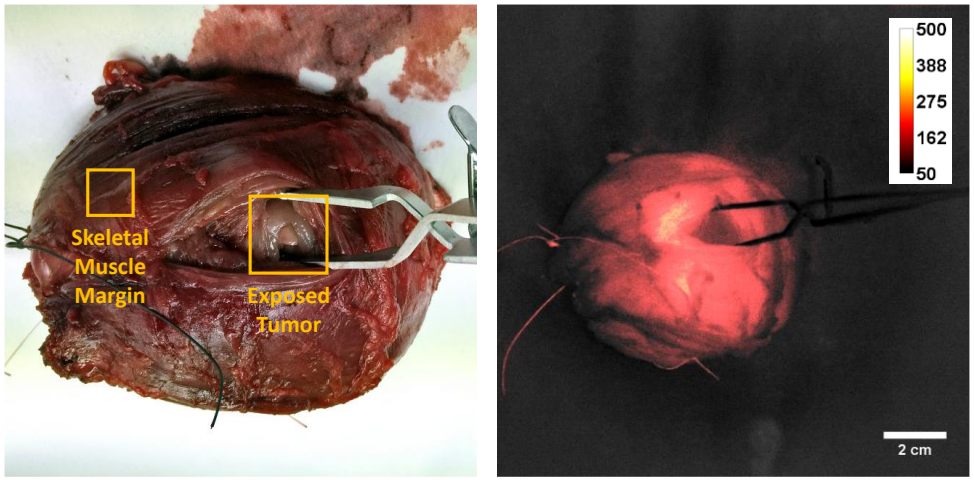


(a) (b)

Figure 5-9: Intraoperative autofluorescence imaging of an excised STS mass with the tumor exposed. (a) Color image of the STS mass. (b) NIR autofluorescence image of the same STS mass.

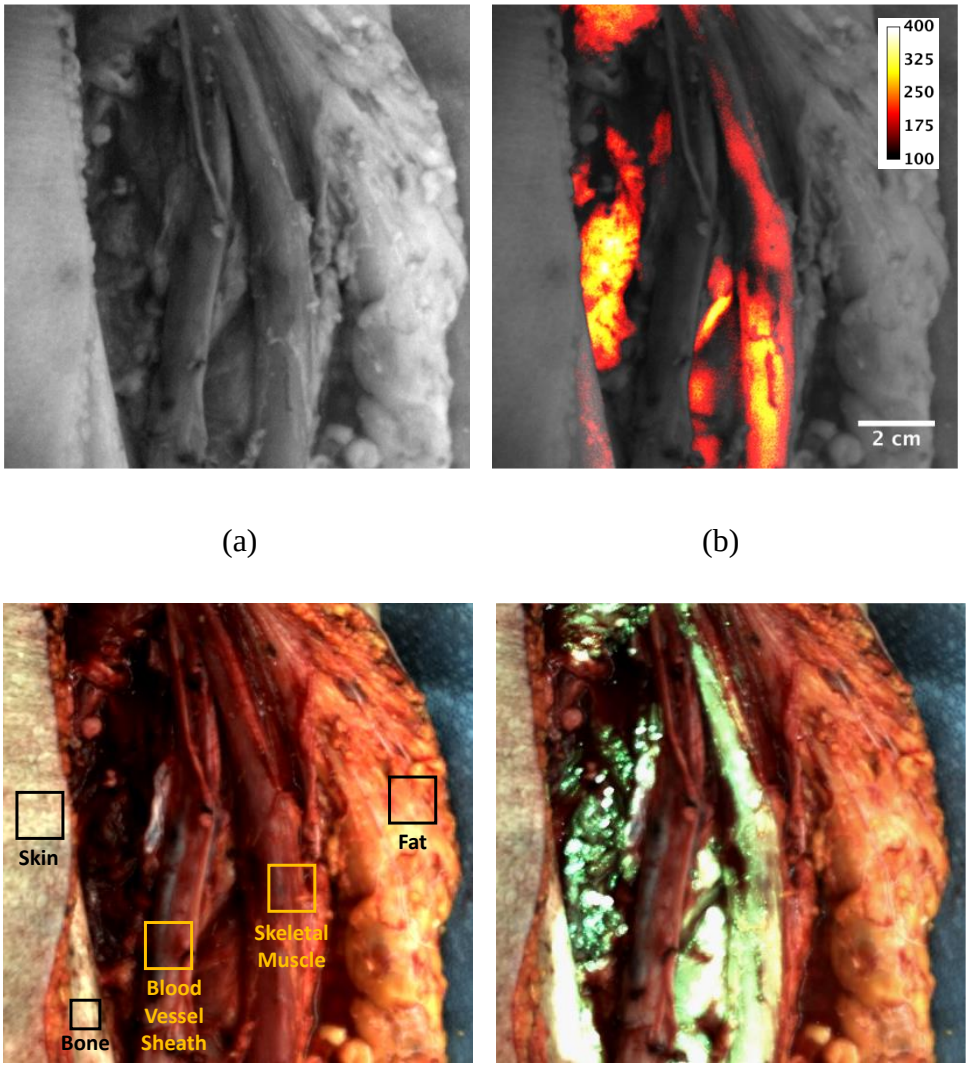


Figure 5-10: Intraoperative NIR autofluorescence imaging of an STS tumor bed. (a) White light image (b) Composite image of quantitative NIR autofluorescence map and white light image. (c) Color image of tumor bed. (d) Real-time projection overlay of the NIR autofluorescence map directly into the tumor bed.

## 5.5 Discussion

In this paper, we have developed an intraoperative ready wide-field fluorescence imaging system, referred to as OTIS, which is comprised of readily available commercial components and features a modular layout that can be to be adapted to various applications in both laboratory research and clinical use. Furthermore, the system features an alternative visualization strategy for image guided surgery by projecting fluorescence maps directly onto the imaging surface and can thus be used to intuitively track the location of both exogenous and endogenous fluorophores in real time without the use of external monitors and the associated need for mental co-registration. The 12-bit CMOS detector with analog gain does not require active temperature control, has a manageable spectral response from 400 to 850 nm, and can be fitted with any standardized c-mount lens and filter setup. This, along with the flexibility to accept any fiber coupled light source, allows the OTIS to accommodate a wide range of spectral, FOV, and spatial resolution requirements without the need for dedicated instrumentation. Through the use of a hybrid long pass filter design, the OTIS is capable of imaging a 15 x 15 $cm^2$ FOV at a 250 μm resolution from a working distance of 35 cm away as seen in Figure 5-3(a) without severe spectral short-shifting. This is comparable to many of the higher-end light emitting diode (LED) array based systems[29] that require further working distances. Unlike these systems, however, the OTIS can easily be modified to a 4.3 x 4.3 $cm^2$ FOV at 78.75 μm resolution as seen in Figure 5-3(b) which may be useful for precision sensitive operations such as glioma resection. As seen in Figure 5-1, most of the optical components are compact, portable, and can be contained within a single unit mountable on to an articulated arm for flexible and mobile use by both clinicians and researchers.

As seen in Figure 5-7, the system features a visualization strategy for fluorescence guided surgery that allows for hands-free continuous image collection and overlay similar to previously described research systems.[30-32] Additional research based approaches for improving image visualization have been based on heads-up displays, either in the form of microscope oculars,[38] semi-transparent mirror,[39,40] or wearable goggles.[41] By leveraging the computer's GPU for parallel processing of basic arithmetic functions, the OTIS is able to perform real-time NIR fluorescence imaging, thresholding, and projection of images simultaneous with acquisition. This serves a dual purpose of intuitively displaying fluorescence maps to the surgeon with minimal disruption to workflow and amplifying the naked-eye detection of low-level fluorescence signal that may not be apparent due to intensity scaling.

While the system is capable of many different configurations, for validation purposes, an ICG targeted setup was used for comparisons to other currently existing intraoperative fluorescence imaging on the market. As seen in Figure 5-4, the OTIS is capable of spatially corrected quantitative measurements with the use of calibration phantoms. Additionally, the *ex vivo* sensitivity tests seen in Figure 5-6 demonstrate the system's capability to measure ICG with a non-linear trend consistent with previous literature[42] down to 0.05 μM concentration with a SNR of 5.6 at an exposure time of 20 msec. In the same figure, quantitative variations in intensity across each ICG well due to the meniscus's effect on ICG self-shielding and re-absorption can also be observed. Further imaging capabilities were subsequently demonstrated in the *in vivo* results seen in Figure 5-8 in which the system was able to track mice tail vein injections of ICG at a dosage level well below the 2.0 mg/kg threshold for FDA-approved human applications.[37] While the system's relatively low optical irradiance in the current configuration limits its dynamic range and prevents it from measuring pM concentrations with the 1 ms exposure times of other devices, the

fluorescence imaging system presented here is regardless more than capable of measuring clinically relevant concentrations of ICG in real time at approximately 33 fps which is comparable to many other commercial fluorescence imaging systems.[29]

The OTIS was intraoperatively evaluated with contrast agent free measurements of *in vivo* human STS and tumor bed NIR autofluorescence as seen in Figure 5-9 and Figure 5-10. These results, along with the tumor margin seen in Figure 5-7, are consistent with previous probe-based studies in which normal skeletal muscle was found to have a stronger NIR autofluorescence signal compared to normal fat and STS.[13] This is most apparent in the tumor mass images seen in Figure 5-9 from which the exposed tumor incision exhibits a significantly decreased signal compared to the surrounding skeletal muscle margin. The tumor bed image in Figure 5-10 also exhibits a strong NIR autofluorescent signal from the surrounding skeletal muscles along with some weak reflections from bone. Through the use of a real time projection overlay system, these regions of high NIR autofluorescence could then be highlighted using a visible color to demonstrate the system's potential for real-time and automated feedback for intraoperative applications such as tumor margin assessment during STS excision.

As a preliminary research device, the current OTIS implementation is not without its limitations, many of which are directly related to the additional challenges associated with wide-field imaging. The biggest issue is associated with quantitative measurement and projection of samples with varying surface topography. In its current form, OTIS field co-registration is accomplished by having the fluorescence imaging and projection maps aligned along a single plane of focus 35 cm away from the imaging head. Within that plane, the flat-calibration method helps to correct for non-homogenous lighting conditions and detector response. Additionally at that plane, the

projection co-registration is accurate from 0 to 1 mm and its maximum resolvable resolution is 2 mm, sufficient for tumor margin assessment applications where biopsies are often 5 mm wide or larger. While adequate for relatively flat imaging surfaces and samples as seen in Figure 5-7, most intraoperative surfaces cannot reliably be assumed to be flat. An example of a topographic effect can be seen in Figure 5-9(b) where the apex of the tumor mass's skeletal muscle margin exhibits a relatively high autofluorescence signal compared to the lower regions near the edges. While a method for planar image correction was developed, an additional method for surface topography and correction must also implemented in order to ensure accurate quantitative measurements and projection mapping. In particular, a benchtop fiducial based image registration algorithm that corrects for distance, imaging angle, and surface curvature has been demonstrated previously by Gan *et al.*[32] Because the OTIS is equipped with a digital light projector, a potential intraoperative solution may exist in fiducial free fringe-phase profilometry for the generation of topographic maps for height intensity calibrations.[43,44]

Another limitation of the OTIS configuration used in this study is the low surface irradiance of the 785 nm illumination light source at the imaging surface. At a distance of 35 cm away and an illumination diameter of over 15 cm, the recorded irradiance at the sample's surface is only 0.7 $mW/cm^2$ despite the laser diode itself outputting over 500 mW of power. While the theoretical interrogation depth of a 785 nm light source should be greater than that of the visible or ultraviolet light commonly used in fluorescence imaging due to the low absorption and scattering of NIR light in tissue, a low irradiance may still confine OTIS measurements to a superficial portion of the sample. This factor in combination with the challenges posed by varying surface topography within a surgical FOV as described earlier, might account for the increase in SNR when imaging ICG perfused mice liver as compared to the tail (Figure 5-8). This may also explain why certain

regions of skeletal muscle within the tumor bed in Figure 5-10 have little to no autofluorescence values as they may be surrounded by a thin layer of fascia or connective tissue. However, because the OTIS was designed to be modular, the laser diode currently being used could potentially be replaced with much more powerful light source for future studies.

The fluorescence imaging system (OTIS) presented here is currently a research prototype designed to demonstrate the concept of a modular intraoperative imaging platform and surgical navigation method. With the many advances in the development of exogenous fluorophores and the utilization of fluorescence imaging as a non-invasive surgical guidance tool, the adaptability of the OTIS allows it to be easily customized for numerous applications. In addition, its ability to simultaneously detect and display fluorescence to the surgeon in a direct and intuitive manner presents an enhancement for the adoption of image guided surgery.

## 5.6 Conclusion

In this paper we have developed and validated a multi-purpose wide-field fluorescence imaging system for intraoperative surgical guidance that is comprised of commercially available standardized components. Its modular layout allows it to accommodate for a broad range of optical properties, FOV, and spatial resolution needs while maintaining a portable design for intraoperative use. Measurements are automatic, quantitative, and feature a real-time projection overlay technique that intuitively displays fluorescence maps directly onto the interrogation surface without the use of remote monitors.

## 5.7 Disclosures

No conflicts of interest, financial or otherwise, are declared by the authors.

## 5.8 Acknowledgements

This work was supported by the National Cancer Institute (NCI) (1F31CA200358), Orthopaedic Research and Education Foundation/Musculoskeletal Tumor Society Clinical Research Grant in Orthopaedic Oncology, and the Vanderbilt Orthopaedic Institute. The content is solely the responsibility of the authors and does not necessarily represent the official views of the sponsors.

## 5.9 References


1. Sevick-Muraca, E. M. & Rasmussen, J. C. Molecular imaging with optics: primer and case for near-infrared fluorescence techniques in personalized medicine. *Journal of biomedical optics* **13**, 041303, doi:10.1117/1.2953185 (2008).
2. Hadjipanayis, C. G., Jiang, H., Roberts, D. W. & Yang, L. Current and future clinical applications for optical imaging of cancer: from intraoperative surgical guidance to cancer screening. *Seminars in oncology* **38**, 109-118, doi:10.1053/j.seminoncol.2010.11.008 (2011).
3. Hollon, T., Hervey-Jumper, S. L., Sagher, O. & Orringer, D. A. Advances in the Surgical Management of Low-Grade Glioma. *Seminars in radiation oncology* **25**, 181-188, doi:10.1016/j.semradonc.2015.02.007 (2015).
4. Stummer, W. *et al.* Fluorescence-guided surgery with 5-aminolevulinic acid for resection of malignant glioma: a randomised controlled multicentre phase III trial. *The Lancet. Oncology* **7**, 392-401, doi:10.1016/S1470-2045(06)70665-9 (2006).
5. Mothes, H. *et al.* Indocyanine-green fluorescence video angiography used clinically to evaluate tissue perfusion in microsurgery. *The Journal of trauma* **57**, 1018-1024 (2004).
6. Brunworth, L. S., Samson, M. C., Newman, M. I. & Ramirez, J. R. Nipple-areola complex evaluation in long pedicled breast reductions with real-time fluorescent videoangiography. *Plastic and reconstructive surgery* **128**, 585-586; author reply 586-587, doi:10.1097/PRS.0b013e31821e71f6 (2011).
7. Adams, K. E. *et al.* Comparison of visible and near-infrared wavelength-excitable fluorescent dyes for molecular imaging of cancer. *Journal of biomedical optics* **12**, 024017, doi:10.1117/1.2717137 (2007).
8. Cheng, Z., Wu, Y., Xiong, Z., Gambhir, S. S. & Chen, X. Near-infrared fluorescent RGD peptides for optical imaging of integrin alphavbeta3 expression in living mice. *Bioconjugate chemistry* **16**, 1433-1441, doi:10.1021/bc0501698 (2005).
9. Funovics, M., Montet, X., Reynolds, F., Weissleder, R. & Josephson, L. Nanoparticles for the optical imaging of tumor E-selectin. *Neoplasia* **7**, 904-911 (2005).
10. Wang, W. *et al.* Near-infrared optical imaging of integrin alphavbeta3 in human tumor xenografts. *Molecular imaging* **3**, 343-351, doi:10.1162/1535350042973481 (2004).

11. Yang, L. *et al.* Molecular imaging of pancreatic cancer in an animal model using targeted multifunctional nanoparticles. *Gastroenterology* **136**, 1514-1525 e1512, doi:10.1053/j.gastro.2009.01.006 (2009).
12. Lakowicz, J. R. *Principles of Fluorescence Spectroscopy*. (Plenum Press, 1983).
13. Nguyen, J. Q. *et al.* Near-infrared autofluorescence spectroscopy of in vivo soft tissue sarcomas. *Optics letters* **40**, 5498-5501, doi:10.1364/OL.40.005498 (2015).
14. Lin, W. C., Toms, S. A., Motamedi, M., Jansen, E. D. & Mahadevan-Jansen, A. Brain tumor demarcation using optical spectroscopy; an in vitro study. *Journal of biomedical optics* **5**, 214-220, doi:10.1117/1.429989 (2000).
15. Lin, W. C., Toms, S. A., Johnson, M., Jansen, E. D. & Mahadevan-Jansen, A. In vivo brain tumor demarcation using optical spectroscopy. *Photochemistry and photobiology* **73**, 396-402 (2001).
16. Chung, Y. G., Schwartz, J. A., Gardner, C. M., Sawaya, R. E. & Jacques, S. L. Diagnostic potential of laser-induced autofluorescence emission in brain tissue. *Journal of Korean medical science* **12**, 135-142 (1997).
17. Bottiroli, G. *et al.* Brain tissue autofluorescence: an aid for intraoperative delineation of tumor resection margins. *Cancer detection and prevention* **22**, 330-339 (1998).
18. Zellweger, M. *et al.* In vivo autofluorescence spectroscopy of human bronchial tissue to optimize the detection and imaging of early cancers. *Journal of biomedical optics* **6**, 41-51, doi:10.1117/1.1332774 (2001).
19. Richards-Kortum, R. *et al.* Spectroscopic diagnosis of colonic dysplasia. *Photochemistry and photobiology* **53**, 777-786 (1991).
20. Ramanujam, N. *et al.* Cervical precancer detection using a multivariate statistical algorithm based on laser-induced fluorescence spectra at multiple excitation wavelengths. *Photochemistry and photobiology* **64**, 720-735 (1996).
21. D'Hallewin, M. A., Baert, L. & Vanherzeele, H. Fluorescence imaging of bladder cancer. *Acta urologica Belgica* **62**, 49-52 (1994).
22. Panjehpour, M. *et al.* Spectroscopic diagnosis of esophageal cancer: new classification model, improved measurement system. *Gastrointest Endosc* **41**, 577-581 (1995).

23. Chwirot, B. W., Chwirot, S., Redzinski, J. & Michniewicz, Z. Detection of melanomas by digital imaging of spectrally resolved ultraviolet light-induced autofluorescence of human skin. *European journal of cancer* **34**, 1730-1734 (1998).
24. Gupta, P. K., Majumder, S. K. & Uppal, A. Breast cancer diagnosis using N2 laser excited autofluorescence spectroscopy. *Lasers in surgery and medicine* **21**, 417-422 (1997).
25. Warren, S. *et al.* Combined ultrasound and fluorescence spectroscopy for physico-chemical imaging of atherosclerosis. *IEEE transactions on bio-medical engineering* **42**, 121-132, doi:10.1109/10.341824 (1995).
26. Berguer, R. Surgery and ergonomics. *Archives of surgery* **134**, 1011-1016 (1999).
27. Stone, R. & McCloy, R. Ergonomics in medicine and surgery. *Bmj* **328**, 1115-1118, doi:10.1136/bmj.328.7448.1115 (2004).
28. Griffiths, M., Chae, M. P. & Rozen, W. M. Indocyanine green-based fluorescent angiography in breast reconstruction. *Gland surgery* **5**, 133-149, doi:10.3978/j.issn.2227-684X.2016.02.01 (2016).
29. AV, D. S., Lin, H., Henderson, E. R., Samkoe, K. S. & Pogue, B. W. Review of fluorescence guided surgery systems: identification of key performance capabilities beyond indocyanine green imaging. *Journal of biomedical optics* **21**, 80901, doi:10.1117/1.JBO.21.8.080901 (2016).
30. Ringhausen, E., Wang, T., Pitts, J., Sarder, P. & Akers, W. J. Evaluation of Dynamic Optical Projection of Acquired Luminescence for Sentinel Lymph Node Biopsy in Large Animals. *Technology in cancer research & treatment* **15**, 787-795, doi:10.1177/1533034615604978 (2016).
31. Sarder, P. *et al.* Dynamic optical projection of acquired luminescence for aiding oncologic surgery. *Journal of biomedical optics* **18**, 120501, doi:10.1117/1.JBO.18.12.120501 (2013).
32. Gan, Q. *et al.* Benchtop and Animal Validation of a Projective Imaging System for Potential Use in Intraoperative Surgical Guidance. *PloS one* **11**, e0157794, doi:10.1371/journal.pone.0157794 (2016).
33. Zhu, B., Rasmussen, J. C., Lu, Y. & Sevick-Muraca, E. M. Reduction of excitation light leakage to improve near-infrared fluorescence imaging for tissue surface and deep tissue imaging. *Medical physics* **37**, 5961-5970, doi:10.1118/1.3497153 (2010).

34. Ayers, F., Grant, A., Kuo, D., Cuccia, D. J. & Durkin, A. J. Fabrication and characterization of silicone-based tissue phantoms with tunable optical properties in the visible and near infrared domain. *Proc. of SPIE* **6870**, doi:10.1117/12.764969 (2008).
35. Nguyen, J. Q. *et al.* Intraoperative Raman spectroscopy of soft tissue sarcomas. *Lasers in surgery and medicine* **48**, 774-781, doi:10.1002/lsm.22564 (2016).
36. Otsu, N. A threshold selection method from gray-level histograms. *IEEE transactions on systems, man, and cybernetics* **9**, 62-66 (1979).
37. Alford, R. *et al.* Toxicity of organic fluorophores used in molecular imaging: literature review. *Molecular imaging* **8**, 341-354 (2009).
38. Killory, B. D. *et al.* Prospective evaluation of surgical microscope-integrated intraoperative near-infrared indocyanine green angiography during cerebral arteriovenous malformation surgery. *Neurosurgery* **65**, 456-462; discussion 462, doi:10.1227/01.NEU.0000346649.48114.3A (2009).
39. Watson, J. R. *et al.* Augmented microscopy: real-time overlay of bright-field and near-infrared fluorescence images. *Journal of biomedical optics* **20**, 106002, doi:10.1117/1.JBO.20.10.106002 (2015).
40. Blackwell, M., Nikou, C., DiGioia, A. M. & Kanade, T. An image overlay system for medical data visualization. *Medical image analysis* **4**, 67-72 (2000).
41. Mondal, S. B. *et al.* Binocular Goggle Augmented Imaging and Navigation System provides real-time fluorescence image guidance for tumor resection and sentinel lymph node mapping. *Scientific reports* **5**, 12117, doi:10.1038/srep12117 (2015).
42. Yuan, B., Chen, N. & Zhu, Q. Emission and absorption properties of indocyanine green in Intralipid solution. *Journal of biomedical optics* **9**, 497-503, doi:10.1117/1.1695411 (2004).
43. Srinivasan, V., Liu, H. C. & Halioua, M. Automated phase-measuring profilometry of 3-D diffuse objects. *Applied optics* **23**, 3105 (1984).
44. Gioux, S. *et al.* Three-dimensional surface profile intensity correction for spatially modulated imaging. *Journal of biomedical optics* **14**, 034045, doi:10.1117/1.3156840 (2009).

# CHAPTER 6

# PORPHYRIN TAIL-END FLUORESCENCE BEYOND 800 NM AS A SPECTRAL MARKER FOR DIFFERENTIATING BETWEEN SOFT TISSUE SARCOMAS AND NORMAL HUMAN SKELETAL MUSCLE

John Quan Nguyen[1], Giju Thomas[1], Wilson R. Adams,[1] Bruce Damon[2], Ginger Holt[3], Anita Mahadevan-Jansen[1]

[1]Vanderbilt University, Biophotonics Center, Nashville, TN, USA, 37232

[2]Vanderbilt University Medical Center, Institute of Imaging Science, Nashville, TN, USA 37232

[3]Vanderbilt University Medical Center, Department of Orthopaedic Surgery and Rehabilitation, Nashville, TN, USA 37232

## 6.1 Abstract

In a previous study, skeletal muscle was found to have a high near infrared (NIR) autofluorescence signal compared to soft tissue sarcomas (STS) and normal fat within the surgical bed. While it was postulated that the negative-contrast in autofluorescence could be utilized for tumor margin assessment and guidance during surgical resections, the biological source of this autofluorescence is currently unknown and was hypothesized to be a spectral tail-end signal from a small molecule known as protoporphyrin IX (PpIX). To explore this hypothesis, we performed a variety of different experiments on *ex vivo* human tissues and heme byproducts in order to characterize and identify the unknown fluorophore. PpIX NIR autofluorescence was verified, and various experiments were able to determine that the unknown fluorophore is a robust small molecule with a fluorescence profile in the visible wavelength regime similar to known spectra for PpIX, a similar molecular weight as PpIX, and fragments on a molecular level similar to PpIX. In addition, the fluorophore was found to be negatively affected by the same degradation processes that occur to heme and PpIX products *in vivo*. Conversely, methods to revert heme products back to PpIX were found to restore NIR fluorescence. Microscopy, immunohistochemistry, and flow cytometry studies suggest that the fluorescence signal is localized within cellular mitochondria where PpIX is known to be synthesized, however, a correlation between mitochondria content and PpIX concentration was not found. Despite the various evidence across multiple modalities strongly suggesting that the NIR autofluorescence signal from skeletal muscle originates from PpIX, investigation of the hypothesis is still inconclusive but at least confirms a porphyrin origin.

## 6.2 Introduction

Fluorescence spectroscopy is a well-established optical modality for measuring the spectral light emissions resulting from fluorescent compounds when excited by a light source. Within the past decade, there has been a wide-spread adoption of fluorescence based techniques in biology and medicine due to its potential to provide quick, automated, and non-destructive assessment of tissue health. While much of the research emphasis has been focused on the angiographic applications of exogenous dyes such as indocyanine green (ICG), fluorescein, and methylene blue,[1-4] a smaller subset of research has been aimed at leveraging naturally occurring endogenous autofluorescence within tissues. For example, autofluorescence has been shown to differ between normal and neoplastic tissues due to changes in fluorophore concentration or environment related to disease progression and has been researched as a diagnostic method in various organ systems including the brain,[5-8] bronchus,[9] colon,[10] cervix,[11] bladder,[12] esophagus,[13] skin,[14] breast,[15] and arterial wall.[16]

Recently, near-infrared (NIR) autofluorescence was found to have a potential for tumor margin assessment and surgical guidance during soft tissue sarcoma (STS) resections.[17] In this intraoperative study, a portable probe based spectroscopy system utilizing a 785 nm excitation source and an integrated emission collection between 810 to 918 nm was able to differentiate between STS and the surrounding normal skeletal muscle and fat commonly encountered within a surgical bed with accuracies of 93%, 92%, and 88% respectively. The key observation that allowed for the development of the classification algorithm was that normal skeletal muscle exhibited a much stronger NIR autofluorescence signal compared to normal fat or any STS subtype. Correspondingly, STS was found to have NIR autofluorescence signals that ranged

between normal skeletal muscle and fat depending on subtype. This trend was consistent even after the data was standardized to account for inter-patient variability and suggests that there may be an endogenous fluorophore present in the tumor bed that could be used as a marker for differentiating tissue types during *in vivo* margin assessments.

Despite these promising results, the basis for the NIR autofluorescence differences within human skeletal muscle, fat, and STS is currently unknown. Other known sources of endogenous fluorescence include aromatic amino acids such as tryptophan, tyrosine, and phenylalanine; enzyme cofactors such as nicotinamide adenine dinucleotide (NADH), flavin adenine dinucleotide (FAD), and pyridoxal phosphate, and whole tissue components such as collagen, elastin, and lipofuscins.[18-20] However, all of these fluorophores can be ruled out as potential candidates as they all have well-characterized excitation and emission peaks ranging from the ultraviolet to visible wavelengths.

Porphyrin derivatives are currently known to be the longest emitting endogenous fluorophores and have often been hypothesized to be the main NIR fluorophore responsible for differentiation in many other cancer studies.[21-25] This is peculiar as the longest emitting endogenous porphyrin, protoporphyrin IX (PpIX), is known to have excitation and emission peaks that are confined to the visible wavelengths up to 700 nm,[19] which is why many of these prior studies have suggested that a NIR residual "tail-end" autofluorescence from the furthest emission peak may be responsible. Despite this long standing hypothesis, no group has yet proven the culpability of PpIX.

PpIX ($C_{34}H_{34}N_4O_4$), is an organic compound consisting of a tetrapyrrole ring surrounded by four methyl, two propionic, and two vinyl side chains.[26-28] As a naturally occurring isomer, it is an intermediate in heme biosynthesis by complexing with ferrous iron to form the heme prosthetic

group of hemoglobin and myoglobin. Apart from being a heme precursor, PpIX is also a photosensitizer notable for its role in photodynamic therapy in which administration of 5-aminoaevlunic acid (ALA) is used to selectively accumulate large concentrations of PpIX in tumor cells and elicit cell death through the production of reactive oxygen species when excited by a light source.[29-32] While many clinical applications require the augmentation of PpIX concentration through exogenous sources, PpIX by itself has been shown to exist at a baseline level correlated with mitochondrial density as it is a an essential precursor in natural heme synthesis.[33] In terms of autofluorescence properties, PpIX is known to have a strong Soret band absorption peak at 405 nm and four weaker Q band absorption peaks at 510, 545, 584, and 635 nm.[34] Fluorescence emission is known to occur at a broad emission peak between 635 and 705 nm while studies beyond 800 nm are currently non-existent.

In this study, we explore the hypothesis that NIR tail-end fluorescence from PpIX beyond 800 nm may be the biological basis behind the spectral marker that allows for the differentiation of STS from the normal muscle and fat as observed in a previous study.[17] Protein denaturation studies were conducted in order to determine if the basis for the fluorescence is protein or small molecule based. From there, a combination of fluorescence and immunohistochemistry microscopy was conducted in order to localize the cellular location of the fluorophore, and high performance liquid chromatography (HPLC) and mass spectroscopy was used to confirm the relative concentrations of PpIX and its precursors within various tissue samples. Mitochondria isolation and flow cytometry measurements were conducted in order to investigate the correlation between cellular mitochondria and PpIX concentration. In parallel with these studies, experiments were conducted in order verify the existence of NIR PpIX tail-end fluorescence past 800 nm, quench the signal

through chemical disruption of the porphyrin ring, and recreating the signal by converting heme samples into its PpIX precursor.

## 6.3 Materials and Methods

### *6.3.1 Sample Acquisition*

Unless specifically stated, all flash frozen *ex vivo* tissue samples were procured from the Cooperative Human Tissue Network (CHTN) – Western Division at the Vanderbilt University Medical Center under approval of the Vanderbilt Institutional Review Board (IRB# 120813). Tissues used in this study include de-identified human STS (undifferentiated pleomorphic sarcomas) samples along with disease-free human skeletal muscle, uterine smooth muscle, ventricular cardiac muscle, and fat tissue.

Liquid samples of PpIX solubilized in a 1:1 mixture of dimethylformamide (DMF) and methanol (MeOH), lyophilized human hemoglobin solubilized in water, lyophilized porcine hemoglobin solubilized in water, lyophilized horse myoglobin solubilized in water, hemin, and biliverdin hydrochloride were used to study the effects of altering the molecular structure of PpIX. All items were purchased from Sigma-Aldrich (St. Louis, MO) and were used as received.

### *6.3.2 Immunohistochemistry and Autofluorescence Microscopy*

Human skeletal muscle, STS, fat, cardiac muscle, and smooth muscle were fixed in 10% formalin before being embedded in paraffin, sectioned into 5 μm thick slices, and placed on glass slides. Unstained slides were used for autofluorescence microscopy while hematoxylin and eosin (H&E) stained slides were used for morphological studies. Mouse monoclonal anti-succinate dehydrogenase (SDH) antibody (Abcam, Cambridge, MA) was used to stain for mitochondrial

membranes and mouse monoclonal anti-slow skeletal myosin heavy chain (MYH7) antibody (Abcam, Cambridge, MA) was used to stain for muscle fiber type.

Autofluorescence microscopy was accomplished using a Zeiss Axiovert 135 (Carl Zeiss, Oberkochen, DE) microscope equipped with a PhotonMax 512B (Princeton Instruments, Trenton, NJ) charge coupled device (CCD) camera cooled to -70°C. Images of unstained slides were first collected under transmission bright field illumination before a 785 nm long pass filter (Semrock, Rochester, NY) was used to acquire corresponding autofluorescence images under illumination from a dispersed 785 nm diode laser source (Innovative Photonic Solutions, Monmouth Junction, NJ). 10x magnification (Carl Zeiss) NIR Images were acquired using WinView/32 software (Roper Scientific, Sarasota, FL) and generated from the average of 5 accumulations at 5 sec per image. Bright field color images of HE stained were acquired by an EVOS XL Core Imaging System (Thermo Fisher Scientific, Waltham, MA). Image analysis was performed in FIJI.[35]

Preliminary studies on -80°C frozen-sectioned optimal cutting temperature (OCT) compound embedded samples demonstrated that the fluorescence signal being investigated was not affected by formalin fixation or paraffin embedding.

### *6.3.3 Tissue Protein Denaturation and Cell Lysis Protocol*

200 mg each of flash frozen human skeletal muscle, STS, and fat samples were pulverized into fine powders using a mortar and pestle precooled in liquid nitrogen. For protein denaturation, the powder was homogenized in a Potter-Elvehjem tissue grinder (Wheaton Industries, Inc.) with a solution of 1 ml 2% sodium dodecyl sulfate (SDS) and 0.1 ml of 160 mM dithiothreitol (DTT) before being heated in a 69°C water bath for 10 minutes. At the end of a 24 hour incubation period,

the homogenate was centrifuged at 10,000 g for 10 minutes before the supernatant was extracted for analysis.

For cell lysis, a control sample of 200 mg flash frozen pulverized muscle sample was homogenized in 1 ml of radioimmunoprecipitation assay (RIPA) buffer (Sigma-Aldrich, St Louis, Missouri) consisting of 150 mM NaCl, 1.0% IGEPAL CA-630, 0.5% sodium deoxycholate, 0.1% SDS, 50mM Tris, and a protease inhibitor (Roche, Mannheim, DE, Cat. No. 05892970001) maintained at a pH of 8.0.

Preliminary studies was performed to verify that each reagent was not fluorescent in the NIR.

### *6.3.4 Sodium Dodecyl Sulfate Polyacrylamide Gel Electrophoresis (SDS-PAGE)*

*Ex* vivo human skeletal muscle samples were homogenized using the cell lysis protocol described earlier and incubated for 24 hours. Following incubation, the sample was cleared by centrifugation at 10,000 g for 15 minutes and mixed with a LDS sample buffer (Invitrogen, Carlsbad, CA) for 15 minutes and heated at 95°C for 5 minutes. Each tissue sample, PpIX controls, and molecular weight standards (Bio-Rad, Hercules, CA) were run at 100 V until the tracking dye reached the bottom of the well. Gels were stained with Coomassie Brilliant Blue dye to ensure proper running of the sample. Each gel was then imaged using a Li-Cor Odyssey Clx fluorescence scanner (Li-Cor Bioscience, Lincoln, NE) at two excitation and emission channels: 1.) 685 nm excitation and 700 nm emission. 2.) 785 nm excitation and 800 nm emission.

### *6.3.5 Generation of PpIX from Hemoglobin and Myoglobin*

Conversion of hemoglobin and myoglobin samples into their PpIX precursor was accomplished through a one-pot, single phase chemical reduction approach as described by Sayyad *et al.*[36] In this process, 0.5 ml of each hemoglobin and myoglobin sample was mixed with 0.5 ml of pyridine

and 0.15 ml of DTT at room temperature, mixed for 1 hour, and incubated for 72 hours. Preliminary studies on individual samples of pyridine and DTT did not exhibit inherent NIR fluorescence

### *6.3.6 Quenching of PpIX NIR Autofluorescence*

Studies of PpIX autofluorescence quenching was carried out by mixing 0.5 ml of PpIX with 0.5 ml of hydrogen peroxide ($H_2O_2$). In addition, another method of autofluorescence quenching was studied by mixing 0.5 ml of PpIX with a bleach sodium hypochlorite solution. Both solutions were incubated for 24 hours. Preliminary studies on individual samples of hydrogen peroxide and the bleach sodium hypochlorite solution did not exhibit inherent NIR fluorescence.

### *6.3.7 Autofluorescence Imaging*

NIR fluorescence imaging was accomplished using device described in the previous chapter. In short, the system consists of a 785 nm diode laser source (Innovative Photonic Solutions, Monmouth Junction, NJ) dispersed across as 15 x 15 $cm^2$ area at an irradiance of approximately 0.6 $mW/cm^2$. Image collection was accomplished using a 12-bit NIR complementary metal-oxide-semiconductor (CMOS) camera (Baslar, Ahrensburg, DE) equipped with a 12 mm focal length manual iris lens (Ricoh, Tokyo, JP) and a machine vision 830 nm long pass filter. Imaging was performed as an averaged accumulation of 10 images each at an exposure time of 0.3 sec.

### *6.3.8 Spectrofluorimetry*

Excitation emission matrix (EEM) measurements of protein denatured skeletal muscle samples was accomplished using a Jobin Yvon Fluorolog-3 FL3-111 spectrofluorometer (Horiba, Tokyo, JP) equipped with a xenon arc lamp light source, double Czerny-Turner based monochromators for wavelength selection, and a R928P photomultiplier (PMT) based detector (Hamamatsu

Photonics, Hamamatsu, JP). Samples were placed into quartz cuvettes during measurements. EEMs were generated at 5 nm intervals of excitations between 350 to 600 nm, and emissions between 600 and 850 nm. These were performed as single measurement scans at 0.1 sec exposures. The excitation profile was generated by measuring the emission values at 630 nm while scanning the sample with excitations between 350 and 600 nm at a 1 nm interval. The emission profile was generated by exciting the sample at 405 nm and measuring the emission spectra between 600 and 850 at a 1 nm interval. Both the excitation and emission spectra were acquired using an averaged measurement of 3 accumulations a 0.1 sec exposure. Data analysis was performed using MATLAB (Natick, MA).

### *6.3.9 High-performance liquid chromatography (HPLC) and Mass Spectroscopy*

HPLC-mass spectroscopy was performed on samples of protein denatured skeletal muscle, STS, smooth muscle, and PpIX Me:OH solution. HPLC separation measurements were acquired on a HSS C18 column (Waters, Milford, MA) and mass detection was accomplished using a LTQ Orbitrap (Thermo Fisher Scientific, Waltham, MA) equipped with a standard electrospray ionization source at a mass resolution of 30,000 at a m/z of 400 Da. The mobile phases were made up of 0.1% HCOOH in $H_2O$ (A) and 0.1% HCOOH in $CH_3CN$ (B). Gradient conditions were as follows: 0-1 min, 50% B, 7-10 min, 100% B, 10.5 to 15 min, 50% B.

Mass spectroscopy measurements were performed at two detection modes: full scan high resolution mass spectroscopy and selected reaction monitoring mass spectroscopy. In the full scan method, the Orbitrap was scanned over a range of 200 to 800 m/z and monitored for the exact mass of PpIX (563.2653 m/z) over time.[37] In the selected reaction monitoring method, the molecular ion of PpIX was isolated in the trap and dissociated by collision to yield a characteristic fragment

ion. The intensity of the fragment ion (504.33 m/z) was then monitored over time within all the protein denatured tissue samples.

### *6.3.10 Mitochondria Isolation and Staining*

Mitochondria isolation was performed on a set of STS and normal muscle samples. 200 mg of whole tissue was washed in phosphate buffered saline (PBS) before being cut into small pieces and incubated on ice in a 0.3 mg/ml solution of trypsin and PBS for three minutes. 800 µl of a 4 mg/ml solution of PBS and bovine serum albumin (BSA) was then added to quench the proteolytic activity of trypsin. The samples were then individually disrupted using a Potter-Elvehjem Tissue Grinder (Wheaton Industries, Millville, NJ, Item# 358003) while on ice. Five strokes were chosen to obtain a homogenous suspension. From there, the mitochondrial and cytosolic fractions were separated by differential centrifugation using a reagent based Mitochondria Isolation Kit for Tissue (Thermo Fisher Scientific, Waltham, MA, Catalog #: 89801) in accordance to the manufacturer's protocol. Following mitochondria isolation, samples where then stained with a 50 nM solution of Mitotracker Green FM (Invitrogen, Waltham, MA, Catalog #: M-7514) and PBS for about 30 minutes. After staining was complete, the cells were re-pelleted by centrifugation at 12,000 x g for 5 minutes and resuspend in 2 ml of PBS.

### *6.3.11 Flow Cytometry*

Flow cytometry event measurements and scatterer value gating was performed using a 3-Laser BD LSRII flow cytometer (BD Biosciences, Franklin Lakes, NJ) in conjunction with BD FACSDiva Software (BD, San Jose, CA) and data analysis was accomplished using FlowJo (FlowJo, Ashland, OR). Prior to measurements, each mitochondrial sample prepared from skeletal muscle and STS was vortexed until the pellet was re-solubilized. PpIX targeted measurements were performed

using an excitation of 405 nm and its fluorescence was recorded at 650 nm. Mitotracker Green FM targeted measurements were performed using an excitation of 488 nm and its fluorescence was recorded at 530 nm. For these experiments, a 50 µM solution of PpIX solubilized in DMF:MEOH and a 50 nM solution of Mitotracker Green FM were used as a positive controls for gating purposes while a hydrogen peroxide quenched sample and an unstained mitochondria sample were used as control negatives.

### *6.3.12 Two Photon Excitation Microscopy*

Multiphoton imaging was performed on a custom multimodal imaging system (Thorlabs Imaging Research, Newton NJ). Briefly, the output beam from a broadly tunable femtosecond laser source (~150fs, 80MHz, Insight DS+, Spectra-Physics, Santa Clara, CA) was implemented in a point-scanning configuration via a pair of scanning galvanometer mirrors. The galvanometer mirrors were magnified and imaged onto the rear aperture of an objective lens (Olympus XLUMPlanFLN, 20X, 1.0NA, water immersion). Using 800 nm excitation, 1248 by 1248 pixel images were acquired with 5 µs pixel dwell times using a bi-direction scanning pattern. Average powers at the sample were approximately 18mW at 800nm. Fluorescence was measured in an epi-detection configuration by placing a 680 nm long-pass filter (Semrock, Rochester, NY) in the beam path prior to the objective. Sample fluorescence was relayed onto a GaAsP photomultiplier tube (Thorlabs, Newton, NJ) with a 625 nm centered, 90 nm bandwidth emission filter (Semrock, Rochester, NY) at both 800 nm excitation. All images were acquired with ThorImageLS 2.4 imaging software (Thorlabs, Newton, NJ). Images were post-processed in FIJI.[35]

## 6.4 Results

Whole tissue samples of normal human skeletal muscle, STS, and normal fat tissues were measured using a wide-field autofluorescence imaging system at an excitation of 785 nm and an integrated fluorescence signal beyond 800 nm. The images in Figure 6-1 confirms the existence of an NIR autofluorescence signal that is significantly higher in human skeletal muscle than in STS and fat.

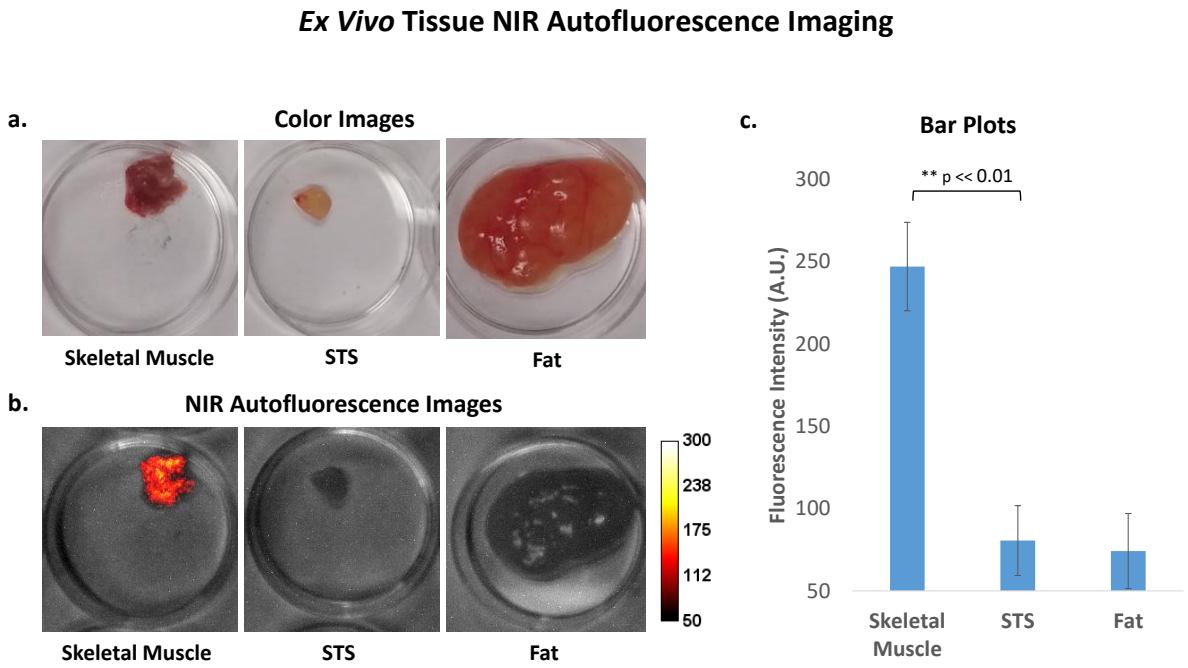


Figure 6-1: Autofluorescence imaging of *ex vivo* tissue samples as measured by a custom designed fluorescence imaging system. (a) Color images of each tissue sample. (b) NIR autofluorescence images of each tissue sample. (c) Bar plot of average NIR autofluorescence intensities within each tissue sample.

The same NIR autofluorescence imaging system was then used to image *ex vivo* samples of PpIX in order to confirm the existence of an NIR autofluorescence signal beyond 800 nm. Hemin, a

heme b analogue consisting of PpIX with a ferric ion and chloride ligand, and biliverdin was used as a negative controls. As seen in Figure 6-2, PpIX exhibits a significant increase in NIR autofluorescence that is about 31 times stronger than the hemin and biliverdin samples.

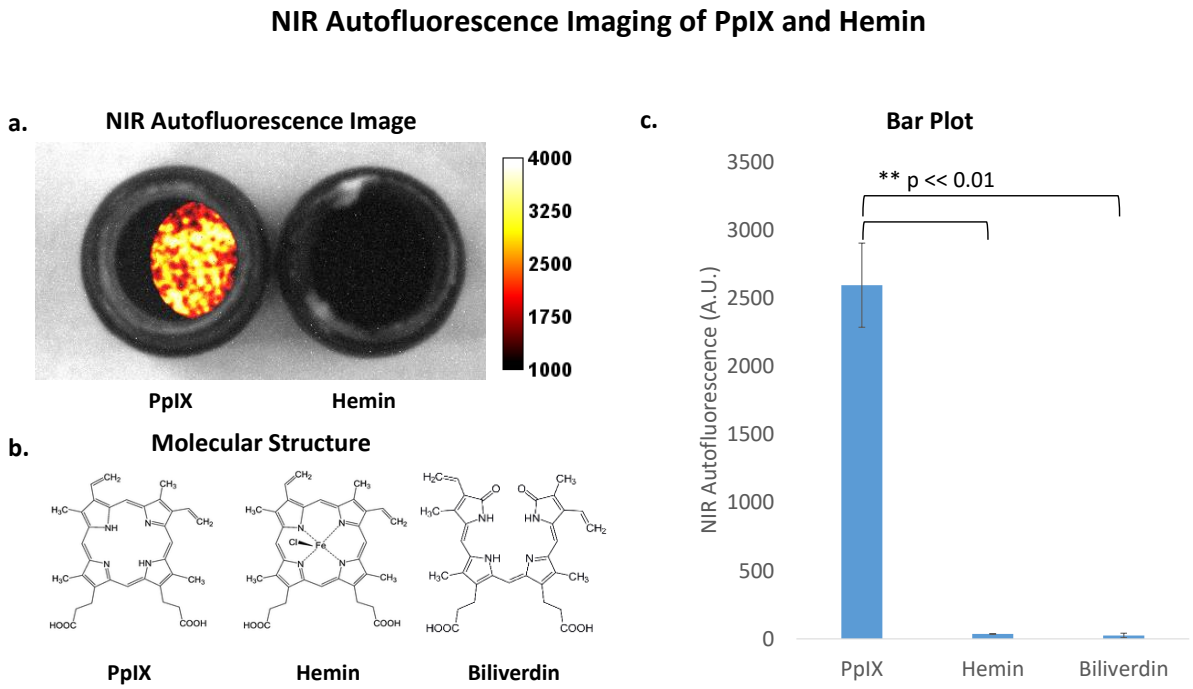


Figure 6-2: NIR autofluorescence imaging of PpIX and hemin as measured by a custom designed fluorescence imaging system (a.) NIR autofluorescence images of each sample. (b.) Molecular structure of PpIX and hemin. (c.) Bar plot of average NIR autofluorescence intensities within each sample.

As PpIX is a small molecule, it was necessary to confirm whether the NIR autofluorescence signal from the tissue samples were protein or small molecule based. To test this, *ex vivo* skeletal muscle samples were subjected to a protein denaturation protocol consisting of SDS, DTT, heating, and 24 hour incubation. In parallel, a control sample was subjected to a RIPA cell lysis protocol that included a protease inhibitor. The differences between both protocols can be seen in Figure 6-3

where the protocol consisting of SDS, DTT, and heating was found to have a significantly higher NIR autofluorescence approximately 1.6 times greater compared to the protocol consisting of a RIPA cell lysis buffer and protease inhibitor.

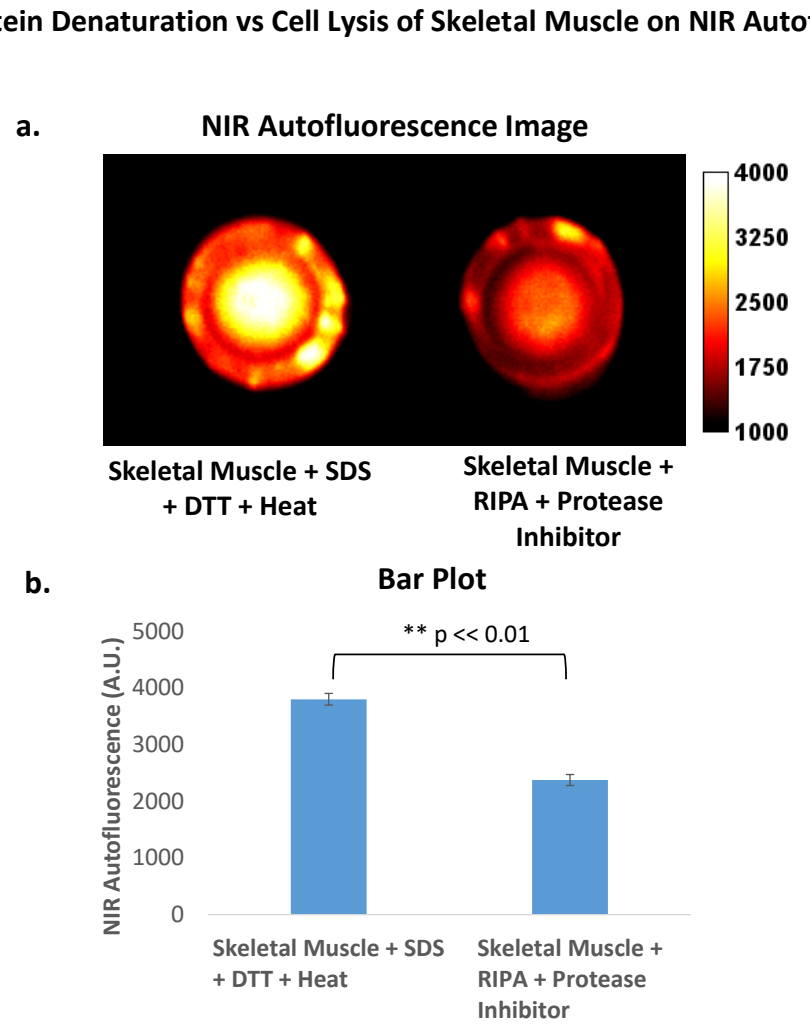


Figure 6-3: NIR autofluorescence of human skeletal muscle following a protein denaturation protocol consisting of SDS, DTT, and heating and a cell lysis protocol consisting of RIPA buffer and protease inhibitor as measured by a custom designed fluorescence imaging system. (a.) NIR autofluorescence image of both samples. (b.) Bar plot of average NIR autofluorescence intensities within each sample.

The same protein denaturation protocol was then applied to *ex vivo* samples of human skeletal muscle, STS, and fat. The results of this can be seen in Figure 6-4 where significant differences could be observed across all three tissue samples with skeletal muscle exhibiting the highest NIR autofluorescence signal followed by STS then fat.

**NIR Autofluorescence Imaging of Protein Denatured *Ex Vivo* Tissue Samples**

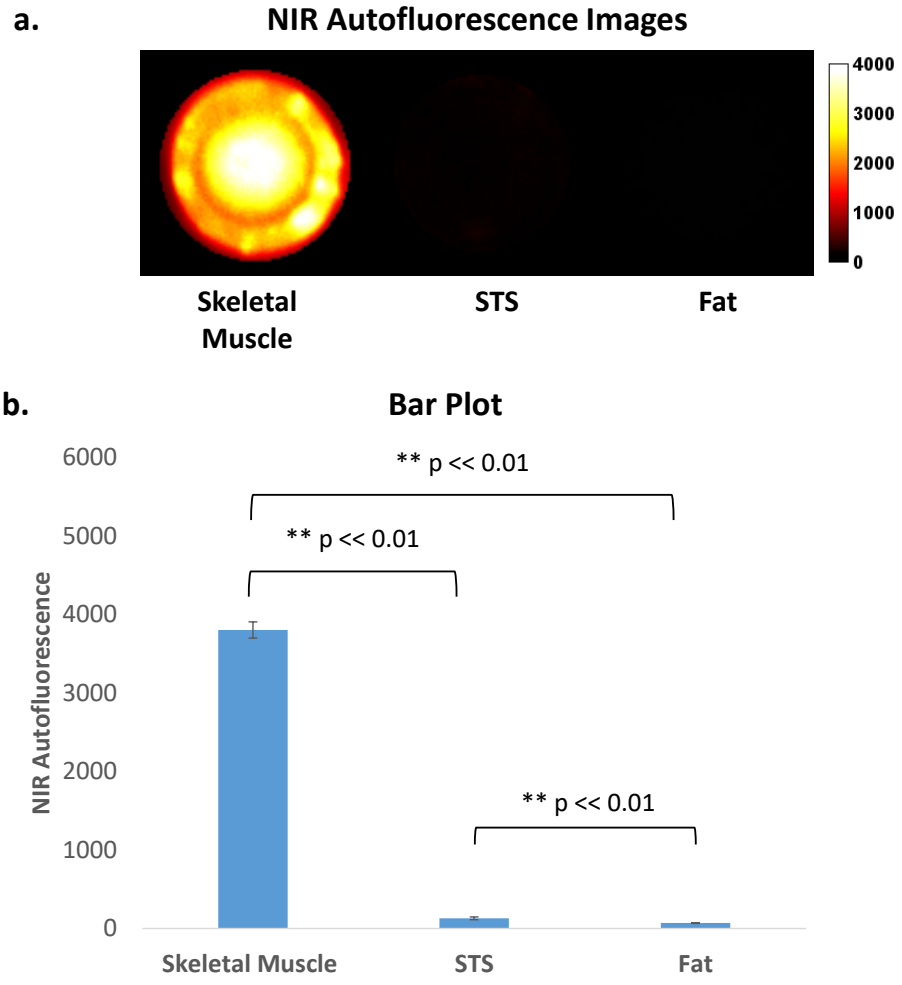


Figure 6-4: NIR autofluorescence imaging of human skeletal muscle, STS, and fat following protein denaturation as measured by a custom designed fluorescence imaging system (a.) NIR autofluorescence images. (b.) Bar plots of average NIR autofluorescence intensities within each sample.

In addition to the protein denaturation experiments, SDS-PAGE was also performed on cell lysed skeletal muscle samples to re-confirm the protein or small molecule basis for the fluorophore. The results of these experiments can be seen in Figure 6-5 where the 700 nm emission channel for both

the skeletal muscle and PpIX samples show no distinctive banding outside of a general streak of fluorescence across each lane. The 800 nm emission channel, however, shows no fluorescence in the skeletal muscle samples, but streaking is still apparent in the PpIX sample.

**Gel Electrophoresis Fluorescence Imaging**

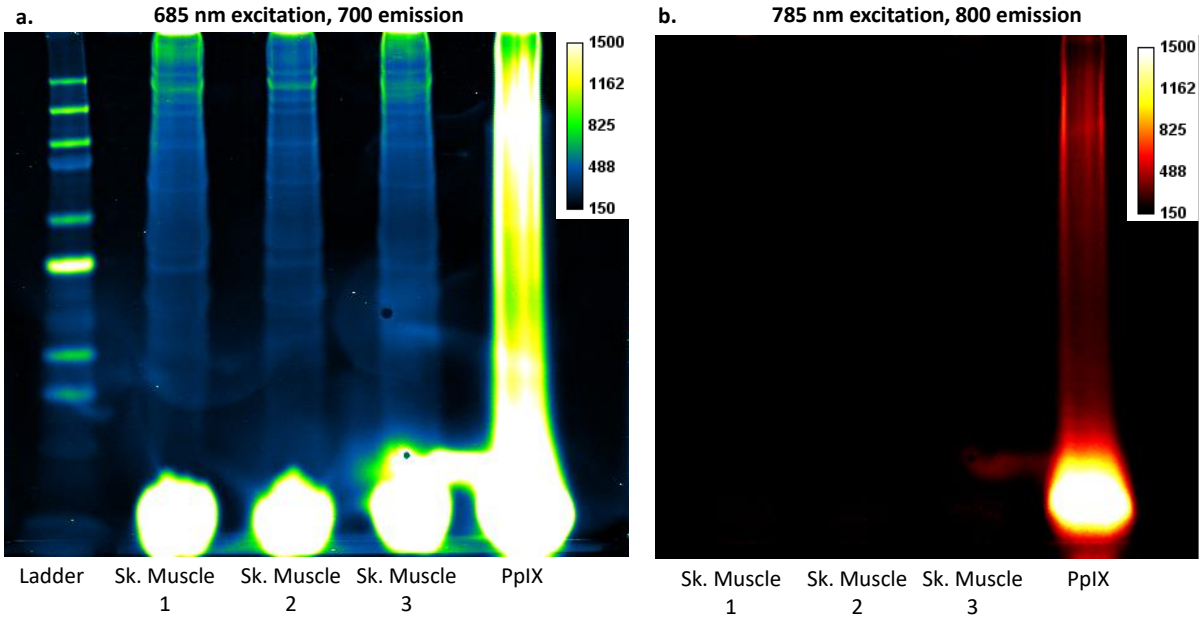


Figure 6-5: Imaging of skeletal muscle gel electrophoresis samples as measured on a LI-COR CLx fluorescence imager. (a.) 685 nm excitation; 700 emission channel. (b.) 785 nm excitation, 800 emission channel.

In order to identify the fluorescence peak excitation and emission profiles, protein denatured skeletal muscle supernatant samples were measured using a spectrofluorometer as seen in Figure 6-6. From the results, it can be observed that the skeletal muscle sample has a large excitation peak at 410 followed by three other peaks at 510, 545, and 580 nm along with two emission peaks at 645 and 696 nm.

**Spectrofluorimetry of Protein Denatured Human Skeletal Muscle Supernatant**

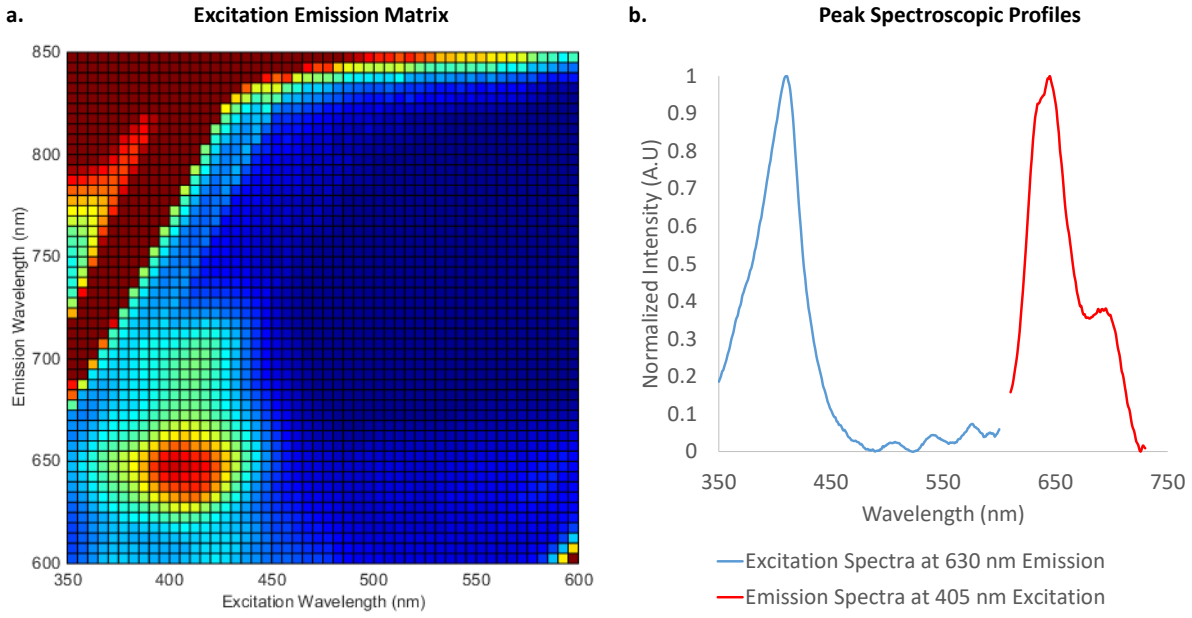


Figure 6-6: Spectrofluorimetry of protein denatured human skeletal muscle supernatant as measured on an Yvon Fluorolog-3 FL3-111 spectrofluorometer. (a.) Excitation emission matrix. (b.) Plot of excitation spectra when measured at a 630 nm emission along with a plot of emission spectra when measured at a 405 nm excitation.

HPLC and mass spectroscopy measurements were performed on protein denatured human skeletal muscle sample along with STS, a PpIX control positive, and a uterine smooth muscle sample as a negative control. The results of these measurements can be seen in the chromatograms in Figure 6-7 and in Table 6-1. PpIX was observed to have a retention time of 8.52 minutes and the skeletal muscle sample was observed to have a retention time of 8.64 min. Both the smooth muscle samples and the STS samples could not be detected via chromatography and within the full scan extracted ion response. When measured using selected reaction monitoring, the skeletal muscle

sample was found to have a higher intensity compared both the STS and uterine smooth muscle samples.

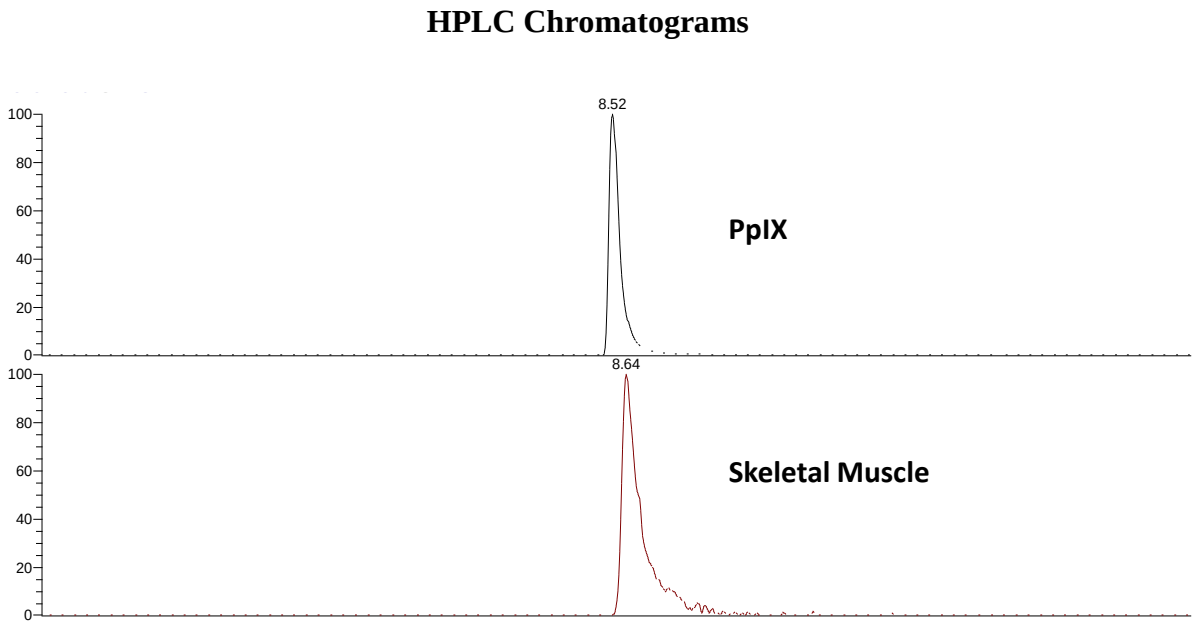


Figure 6-7: HPLC chromatograms of PpIX and protein denatured skeletal muscle supernatant as measured by a LTQ Orbitrap HPLC Column.

| Sample | Full Scan Extracted Ion Response (Current Intensity) | Selected Reaction Monitoring (Current Intensity) |
|---|---|---|
| PpIX | 116,000,000 | 6,530,000 |
| Skeletal Muscle | 1,930,000 | 106,000 |
| STS | ND | 2,060 |
| Uterine Smooth Muscle | ND | 1,760 |

Table 6-1: Measurements at two detection modes: full scan high resolution mass spectroscopy and selected reaction monitoring mass spectroscopy.

Immunohistochemistry and NIR autofluorescence microscopy were performed on a set of cut formalin fixed human tissue samples in order to localize the spatial source of autofluorescence. From the results in Figure 6-8, it can be seen that skeletal muscle exhibits granular NIR autofluorescence throughout each muscle fiber with a high concentration accumulated within the outer edge of the sarcoplasm. A high autofluorescence signal was also observed within cardiac muscle, but to a much lesser degree in the STS, fat, and smooth muscle samples. SDH antibody was used to stain for mitochondrial density while MYH7 antibody was used to stain for myosin heavy chain.

**Immunohistochemistry and NIR Autofluorescence Microscopy**

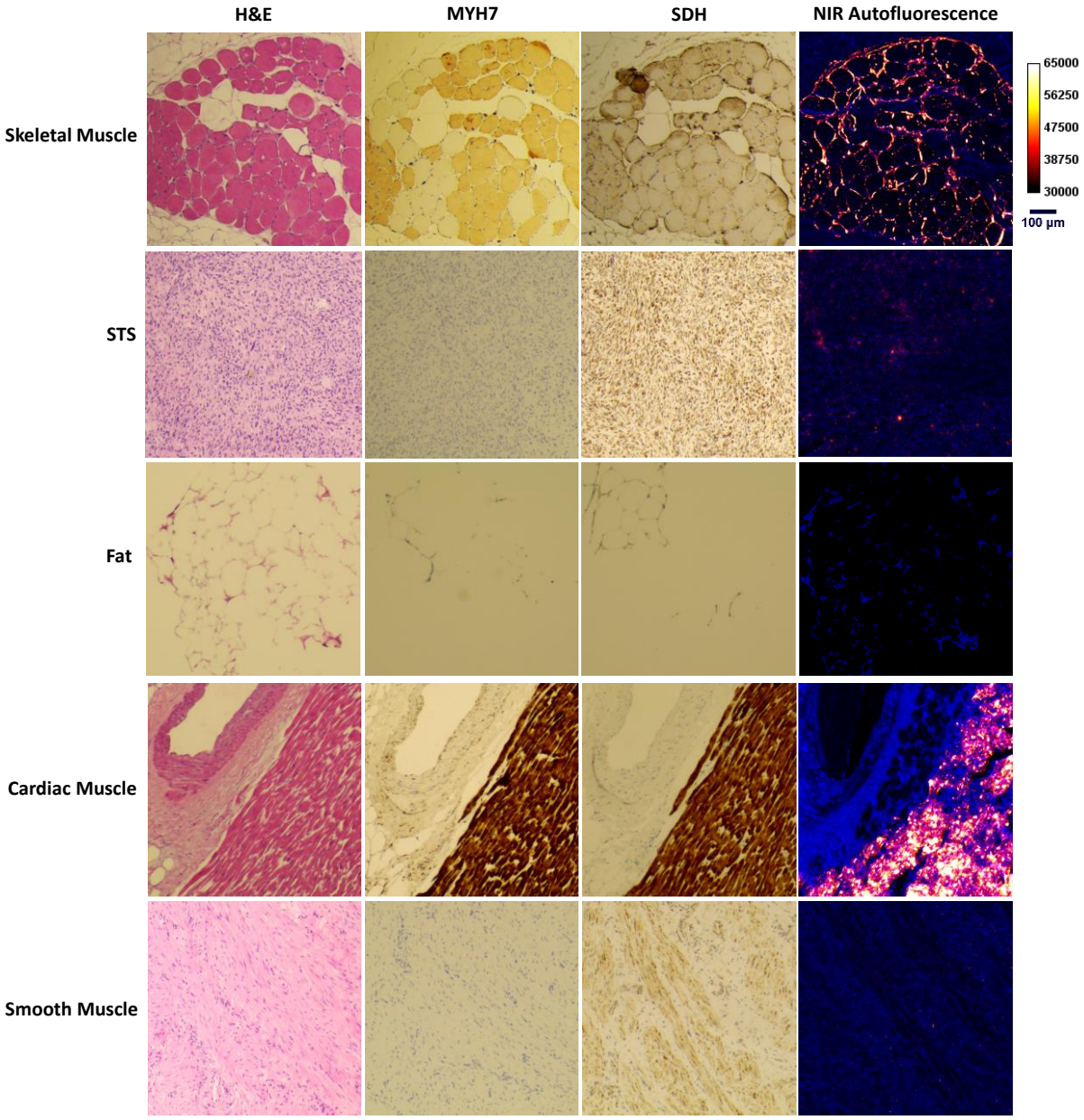


Figure 6-8: Immunohistochemistry and NIR autofluorescence microscopy of various *ex vivo* human tissue samples as measured on a custom designed NIR fluorescence microscope. MYH7 and SDH antibodies stain for myosin heavy chain and mitochondrial oxidative capacity.

The same unstained tissue slides were then imaged using two-photon excitation microscopy at 800 nm excitation and emission collection at 625 nm. The results can be seen in Figure 6-9. Despite the larger magnification, a pattern of fluorescence similar to those in Figure 6-8's NIR microscopy images can be observed with an additional fluorescence signal from the artery adjacent to the cardiac muscles.

**Two Photon Excitation Microscopy**

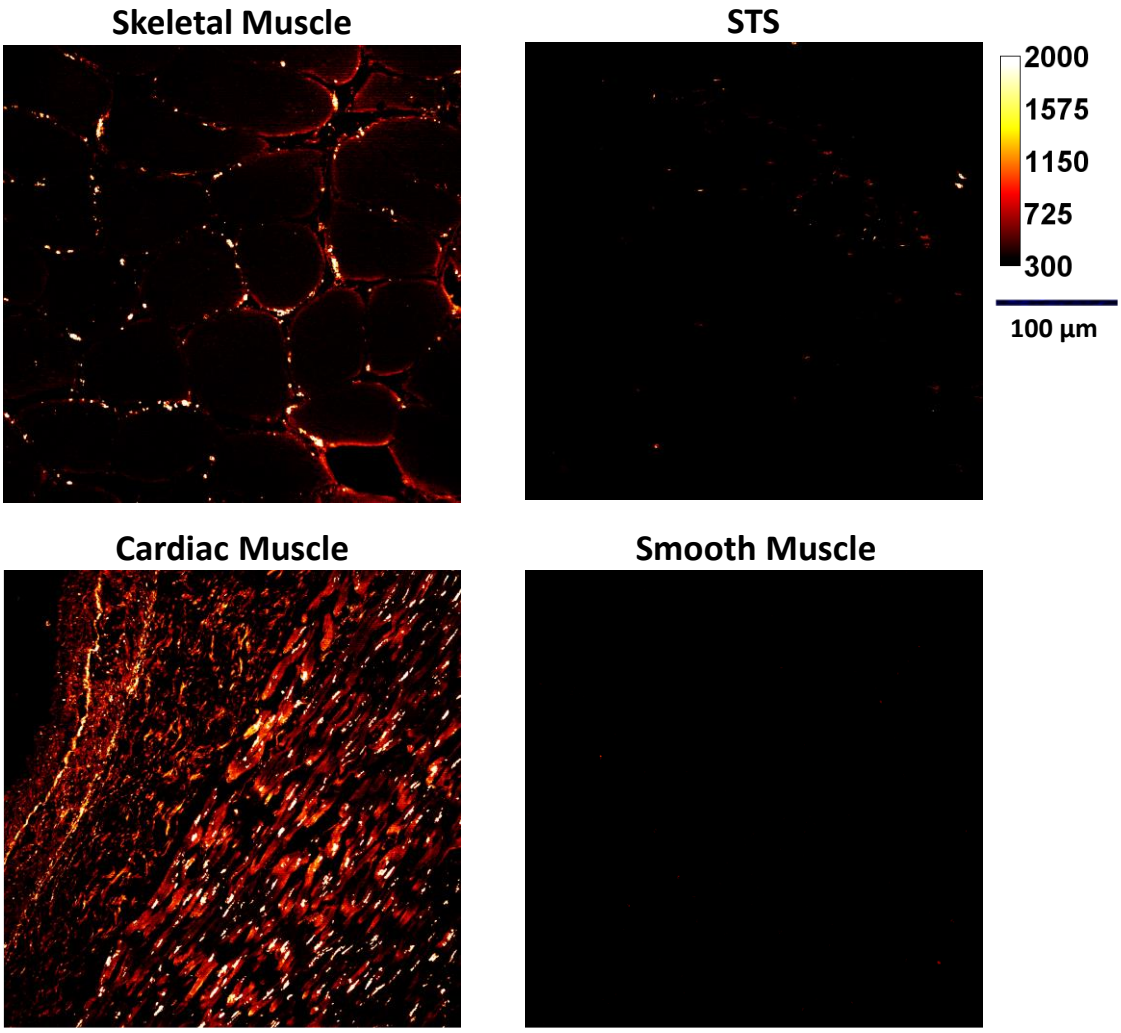


Figure 6-9: Two photon microscopy of paraffin fixed samples of *ex vivo* skeletal muscle, STS, cardiac muscle, and smooth muscle at 800 nm excitation and emission collection at 625 nm.

Flow cytometry measurements were performed on Mitotracker Green stained mitochondria isolated samples from *ex vivo* human skeletal muscle and STS samples in order to determine if a correlation existed between a sample's mitochondria and its autofluorescence signal at excitation and emission wavelengths correlating with known PpIX spectra. The results can be seen in Figure

6-10 in which STS was observed to have higher mitochondria stained fluorescence than skeletal muscle, but intrinsic fluorescence was higher in skeletal muscle than in STS.

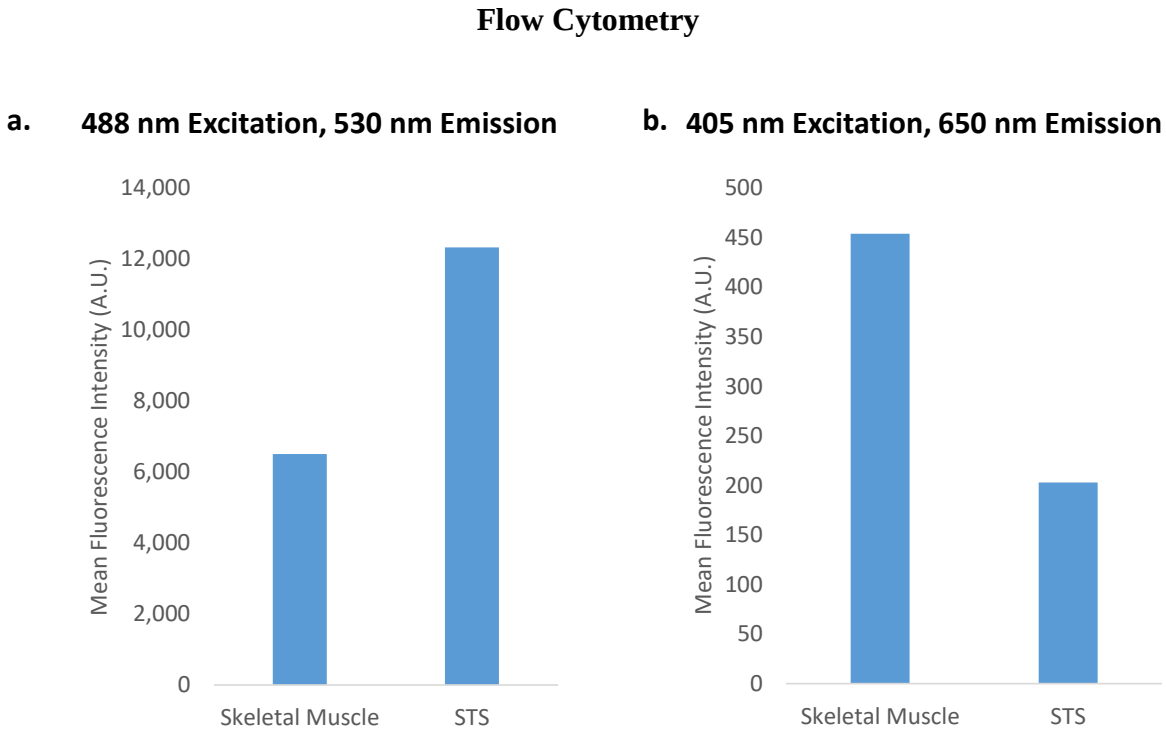


Figure 6-10: Flow cytometry mean fluorescence of mitochondria stained skeletal muscle and STS as measured on a BD LSRII flow cytometer. (a.) Measurements of samples at 488 nm excitation and 530 nm emission for the detection of Mitotracker mitochondria stain. (b.) Measurements of samples at 488 nm excitation and 530 nm excitation.

Further experiments were performed to investigate the hypothesis of PpIX NIR fluorescence. This included an experiment to disrupt PpIX's porphyrin structure through exposure to bleach and $H_2O_2$. The results of this experiment can be seen in Figure 6-11 where PpIX solubilized in DMF:MeOH were exposed to bleach and $H_2O_2$ solutions and were observed to exhibit significantly decreased fluorescence intensities compared to their original samples.

**NIR Fluorescence Imaging of PpIX Degradation**

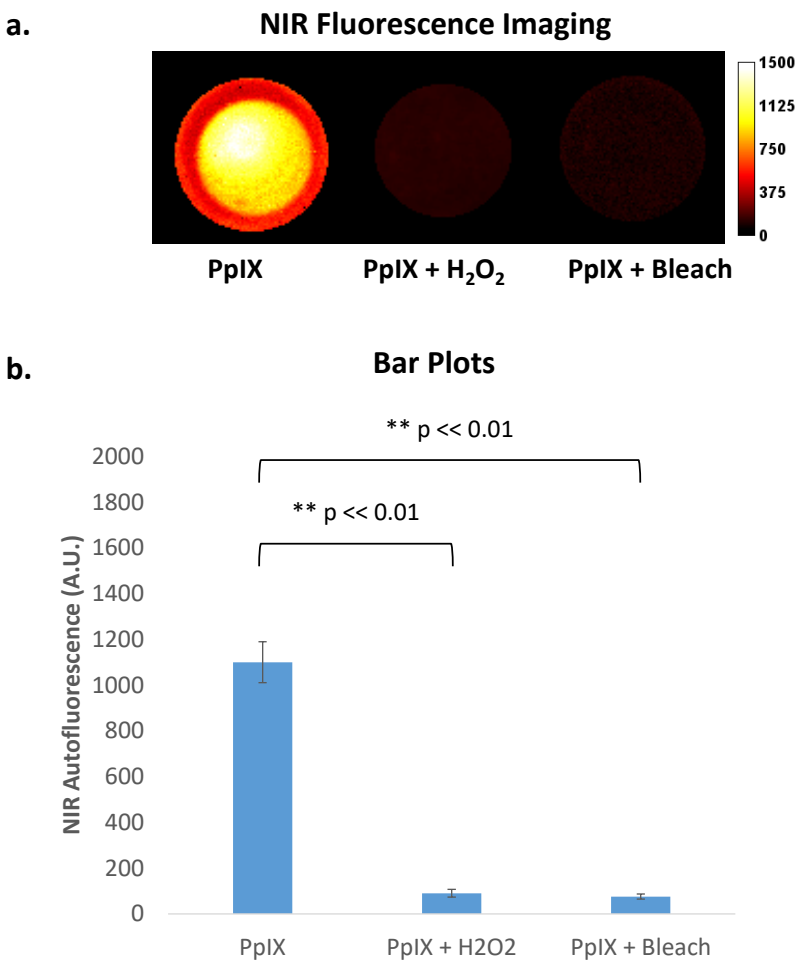


Figure 6-11: NIR fluorescence imaging of a PpIX DMF:MeOH solution when exposed to bleach and $H_2O_2$ as measured by a custom designed fluorescence imaging system. (a.) NIR autofluorescence images of each sample. (b.) Bar plot of average NIR autofluorescence intensities within each sample.

The same experiment was then repeated with protein denatured human skeletal muscle supernatant samples. The results can be seen in Figure 6-12 where the skeletal muscle samples that were exposed to bleach and $H_2O_2$ exhibited a significant decrease in NIR autofluorescence compared to the original sample.

**NIR Fluorescence Imaging of Porphyrin Degradation in Skeletal Muscle Samples**

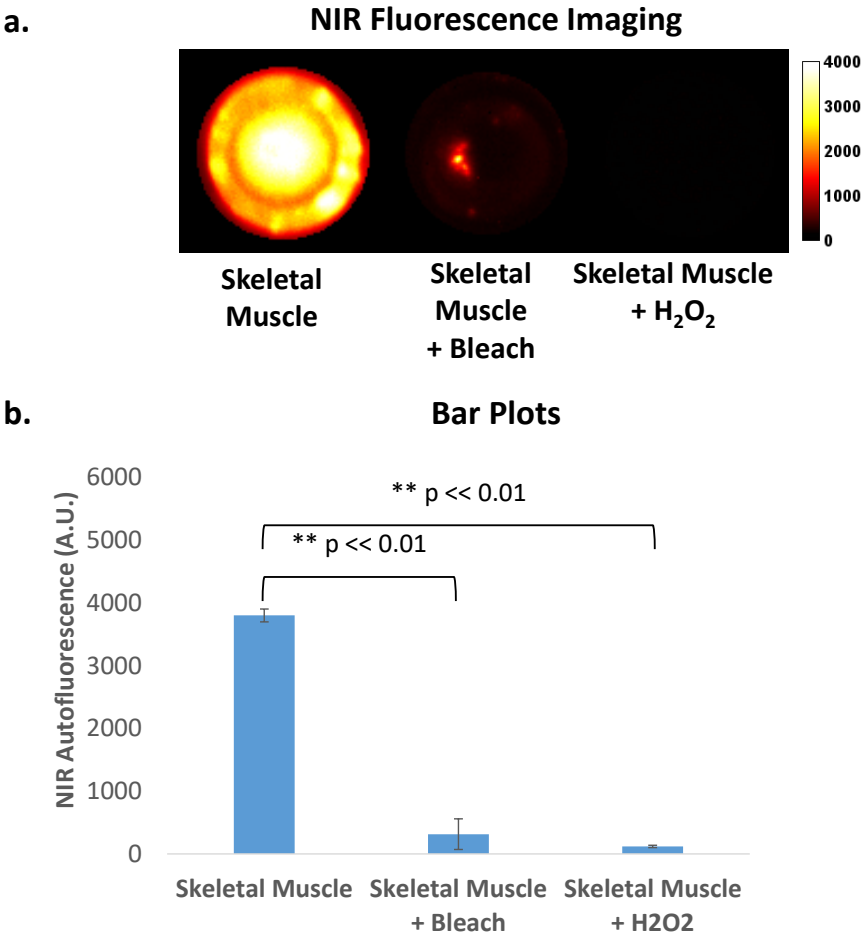


Figure 6-12: NIR fluorescence imaging of protein denatured skeletal muscle supernatant when exposed to bleach and $H_2O_2$ as measured by a custom designed fluorescence imaging system. (a.) NIR autofluorescence image of both samples. (b.) Bar plot of average NIR autofluorescence intensities within each sample.

An experiment was also performed in order to convert hemoglobin and myoglobin into PpIX through the synthesis of iron nanoparticles from exposure to pyridine and DTT, and measure the changes in NIR autofluorescence. The results of this can be seen in Figure 6-13 where the

hemoglobin and myoglobin samples begin with minimal NIR autofluorescence, but exhibit significant increases when converted to PpIX.

**NIR Fluorescence Imaging of PpIX Generated from Hemoglobin and Myoglobin**

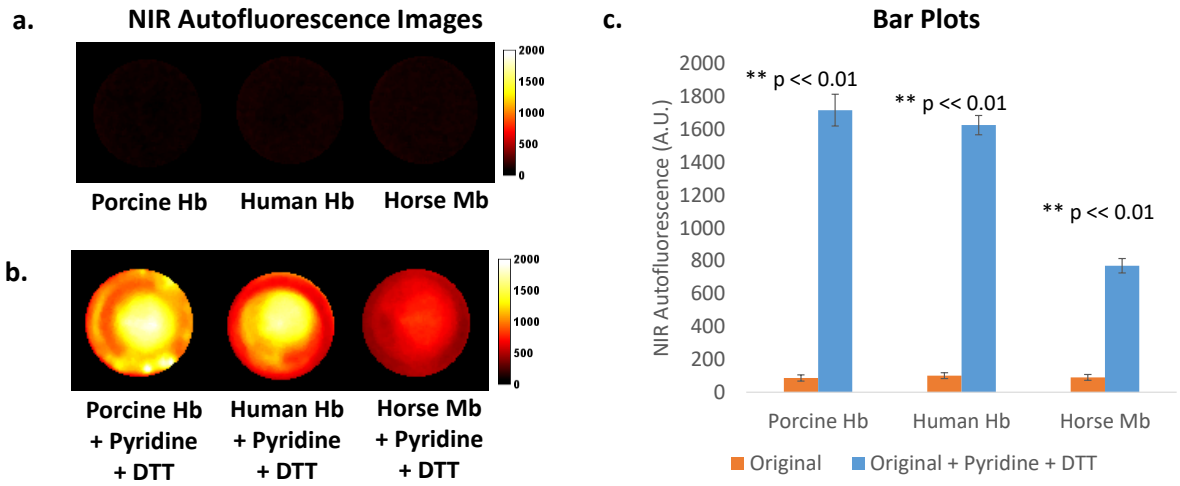


Figure 6-13: NIR fluorescence imaging of PpIX generated from porcine hemoglobin, human hemoglobin, and horse myoglobin when incubated with pyridine and DTT as measured by a custom designed fluorescence imaging system. (a.) NIR autofluorescence image of samples before incubation. (b.) NIR autofluorescence image of samples after incubation. (c.) Bar plot of average NIR autofluorescence intensities within each sample before and after iron removal.

## 6.5 Discussion

The results described in this manuscript is an extension of a previous study which demonstrated the potential of intraoperative NIR autofluorescence measurements for tumor margin assessment and surgical guidance during STS resections.[17] The key observation from the previous study was that normal skeletal muscle surrounding STS's exhibited a significantly higher autofluorescence signal compared to the STS and normal fat found within the tumor bed. At the time, the biological

basis for the autofluorescence signal was unknown and was hypothesized to be a porphyrin derivative. In this study, various experiments were conducted to characterize the unknown NIR fluorophore in tissues and investigate a hypothetical origin in PpIX.

In our first set of experiments, seen in Figure 6-1, whole *ex vivo* tissue samples including human skeletal muscle, STS, and fat were imaged using a previously described wide-field NIR fluorescence imaging system at an excitation of 785 nm and an integrated emission collection beyond 800 nm. From the results in Figure 6-1 it can be observed that the human skeletal muscle sample has a significantly higher NIR autofluorescence intensity compared to both the STS and normal fat samples. This result confirms the existence of a strong NIR autofluorescence signal within human skeletal muscle and is consistent with our previous *in vivo* findings in human patients measured with a probe based spectroscopy system.[17]

From there, the same wide-field NIR fluorescence imaging system was used to measure *ex vivo* samples of PpIX, hemin, and biliverdin. From the results in Figure 6-2, it can be observed that PpIX exhibits a significantly higher NIR autofluorescence intensity compared to both the hemin and biliverdin sample while the biliverdin and hemin samples do not exhibit a significant intensity difference between each other. These findings are interesting in that it verifies the existence of PpIX NIR autofluorescence despite a lack of a literature evidence beyond the visible wavelengths.[34] Both the hemin and biliverdin results are consistent with literature that suggests that their non-protein bounded states are confined to the ultraviolet (UV) to visible (VIS) wavelengths with a sorbet excitation peak between 375 and 400 nm and emission peaks between 400 and 500 nm.[38,39] During the heme synthesis pathway,[40] the enzyme ferrochelatase catalyzes the insertion of ferrous iron into PpIX and converts it into heme. When heme is not bound to a

protein such as globin, the ferrous $Fe^{2+}$ component can oxidize into its $Fe^{3+}$ state and the molecule is known as hemin. A lack of fluorescence in the hemin sample is consistent with prior studies that found that the binding of iron to porphyrins can induce fluorescence quenching, whereas the binding of zinc or tin induces a partial loss.[41] During *in vivo* heme catabolism, heme oxygenase catalyzes the degradation of heme into biliverdin, ferrous iron, and carbon monoxide.[42] From the results of this experiment, PpIX is the only component that exhibits a NIR autofluorescence signal past 800 nm when excited at 785 nm.

Protein denaturation studies were performed in order to evaluate whether the skeletal muscle NIR autofluorescence was protein based. To do this, *ex vivo* human skeletal muscle samples were incubated in a SDS DTT solution for 24 hours with prior heat treatment. In parallel, another sample of skeletal muscle sample from the same tissue was incubated in a RIPA cell lysis buffer with a protease inhibitor. Accelerated by heat, SDS breaks up the two- and three-dimensional structures of proteins by adding a negative charge to amino acids while DTT helps to disrupt protein tertiary and quaternary structure through reduction of sulfide bonds. In contrast, the RIPA buffer and protease inhibitor cocktail aims for efficient cell lysis and protein solubilization while avoiding protein degradation and interference with protein immunoreactivity and biological activity. The results of this experiment can be seen in Figure 6-3 where the skeletal muscle sample processed for protein denaturation via SDS DTT exhibits a significantly stronger NIR autofluorescence signal than the sample incubated in the RIPA protease inhibitor solution. Because the signal is the strongest within the protein denatured protocol, these results suggests a small molecule basis for the NIR fluorescence signal.

The protein denaturation protocol was then repeated with additional *ex vivo* tissues including human skeletal muscle, STS, and fat. The results in Figure 6-4 are consistent with those seen in Figure 6-1 and suggests that the protein denaturation protocol is adequate for preparing liquefied tissue samples that retain NIR autofluorescence along with the unknown fluorophore.

As an additional check to see if the fluorescence is protein or small molecule based, *ex vivo* human skeletal muscle samples were prepared using the cell lysis protocol and processed through gel electrophoresis. Each gel was then imaged using a fluorescence scanner at two different wavelength regimes. The results of this experiment can be seen in Figure 6-5, where the 685 / 700 nm excitation / emission channel exhibits smearing across all the lanes containing skeletal muscle and PpIX samples. The 785 / 800 nm excitation / emission channel however did not exhibit a signal across all the skeletal muscle samples despite further smearing from the PpIX control positive sample. The lack of skeletal muscle signal in this channel despite a signal in the PpIX lane suggests that the fluorophore concentration in the skeletal muscles samples may be too small to detect as PpIX's fluorescence intensity is higher in the 685 / 700 nm channel. In total, none of the samples analyzed exhibited discrete banding across either measurement channels which further suggests that the fluorophore is a small molecule capable of quickly precipitating through the gel.

The discovery that NIR fluorescence was retained after protein denaturation and centrifugation allowed for the preparation of liquid tissue samples that could then be analyzed using a spectrofluorometer in order to determine the excitation and emission profiles of the fluorophore within the UV-VIS wavelength range of the device. The results of this study can be seen in Figure 6-6 where the skeletal muscle sample exhibits a similar EEM, absorption, and emission spectra to that of PpIX. Literature values of PpIX excitation peaks indicate a strong Soret band at 405 nm

followed by four weaker Q bands at 510, 545, 584, and 635 nm with two emission peaks at 635 and 705 nm.[34] In this spectrofluorimetry experiment, protein denatured human skeletal muscle samples were found to have excitation peaks at 410, 510, 545, and 580 nm along with two emission peaks at 645 and 696. A fourth excitation was not observed in our study because of its overlap with the 645 nm emission peak, but regardless, these results further support the hypothesis for PpIX being the fluorophore of interest.

From the results presented earlier, it was apparent that while PpIX does not have a fluorescence emission peak beyond 800 nm, a trailing tail-end signal may be responsible for the observed NIR signals in the skeletal muscle samples. The next step was to investigate whether or not PpIX is actually present within human skeletal muscle. Towards this goal, HPLC-mass spectroscopy was utilized to specifically isolate and measure the amount of PpIX within a set of *ex vivo* human tissue samples including skeletal muscle, STS, a smooth muscle negative control, and a PpIX DMF:MeOH positive control. In liquid chromatography, small molecules are physically separated and characterized by their retention time. From the results seen in Figure 6-7, the retention time and profile of the skeletal muscle samples and PpIX positive control were similar at 8.64 and 8.52 min respectively. The STS and smooth muscle samples did not exhibit retention within range of the PpIX control positive which suggests that little to no PpIX was present in those samples. Also seen in Figure 6-7 are the mass spectroscopy results using two different methods. In the full scan high resolution method, the samples were monitored for the exact mass of PpIX[37] (563.2653 m/z) over time and were found to be present in both the skeletal muscle and positive control samples while undetected in the STS and smooth muscle samples. In the selected reaction monitoring method, molecules was isolated and dissociated in order to yield and detect characteristic fragment ions of PpIX at (504.33 m/z). Here, the levels of PpIX in the skeletal muscle samples were about

50 times greater than STS and about 60 times greater than the smooth muscle sample. These results, along with being consistent with one another, confirms the presence of PpIX within the skeletal muscle samples that is much higher than STS or smooth muscle. In addition, these results along with the results seen in the previous results suggests that a tissue's NIR autofluorescence signal may be directly related to the amount of PpIX within the sample.

Apart from confirming the existence of PpIX NIR fluorescence signal and confirming its presence within tissues, a microscopy and immunohistochemistry study was performed on a set of *ex vivo* tissue samples including human skeletal muscle, STS, fat, cardiac muscle, and smooth muscle in order to spatially localize the NIR fluorescence signal. Prior experiments had shown that the fluorophore was not heat or formalin fixation sensitive, and further experiments were also able to demonstrate that the fluorophore was resilient even to the ethanol treatment and heating conditions required in paraffin processing.[43] As PpIX is a precursor within the heme synthesis pathway that occurs in and around mitochondria,[36,40,44] there was interest in investigating whether the fluorescence would be localized near cellular mitochondria and whether or not muscle fiber types could be a predictor of mitochondria content and NIR fluorescence intensity. For this purpose, tissues were serially sliced and stained with H&E, MYH7 antibody, and SDH antibody in addition to an unstained slide for NIR fluorescence microscopy. MYH7 antibody stain aims to identify heavy myosin chains associated with slow twitch muscle fiber types that are commonly rich in mitochondria and myoglobin.[45] Additionally, the SDH antibody stain was used to identify mitochondria by staining for the enzyme within the inner membranes.[46] From the NIR autofluorescence images shown in Figure 6-8, it can be observed that fluorescence within the skeletal muscle is generally localized near the perimeter of each myocyte's sarcolemma with an occasional speckle of signal within each myocyte. These regions correlate well to the regions of

the tissues that stain for anti-SDH indicative of mitochondrial location, but do not correlate well to the anti-MYH7 stain for muscle fiber types. The inconsistencies between the SDH and MYH7 stains may be related to other past studies which have shown that fiber type composition and metabolic activity are not perfectly correlated[47-49] due to the existence of two mitochondrial subpopulations in skeletal and cardiac[50-52] muscle including subsarcolemmal and intermyofibrillar mitochondria.[49,53-55] Subsarcolemmal mitochondria comprise about 5 to 40% of the total skeletal muscle mitochondria and are known to have a large lamellar shape that is correlated with endurance training with increasing mitochondrial oxidative capacity towards enhanced fatty acid metabolism.[50] They have also been found to have higher SDH activity compared to intermyofibrilla mitcohonia,[49,53-55] which is directly involved with contractile activity.[51] The results in Figure 6-8 suggests that there may be a correlation between high oxidative capacity subsarcolemmal mitochondria and NIR fluorescence. This is again consistent with the microscopy and immunohistochemical results from the cardiac tissue sample. The STS and smooth muscle samples, while relatively mitochondria rich according to the SDH stain, did not exhibt significant PpIX fluorescence which is consistent with previous results. The same could be said of the fat tissue sample which does not exhibit significant fluorescence nor mitochondiral staining. These results as a whole suggest that the NIR fluorescence signal is likely to be localized within skeletal and cardiac muscle subsarcolemmal mitochondria and support the hypothesis that specialized mitochondrial populations may exist due to location, metabolite production, and proximity to capillaries.[52,54,56-58] As subsarcolemmal mitochondria are known to have high oxidative capacity, fatty acid metabolism, and iron per milligram protein,[59] it could be hypothesized that these mitochondria will produce more succinyl-CoA for use in producing PpIX during heme synthesis due to an abundance of precursors. Conversely, defects in insulin signaling and glucose transport

related to diseases such as obesity and insulin resistant diabetes type 2 may also be attributed to mitochondrial dysfunction[60] and can potentially be identified indirectly by a lack of PpIX in patients. However, exploring that hypothesis is outside the scope of this manuscript and will be explored further in the future.

Interestingly, the two-photon excitation microscopy images in Figure 6-9 are quite similar to the NIR fluorescence images seen in Figure 6-8 for the skeletal muscle, STS, and smooth muscle samples. The two-photon excitation cardiac muscle image includes extra fluorescence in the within the artery region which may be due to background elastin fluorescence as the 800 nm excitation is equivalent to a 400 nm excitation and emission collection at 625 nm. Large blood vessels such as arteries often consist of a tunica adventitia layer which is predominantly elastin based, and a tunica media layer which is comprised of a combination of smooth muscle and elastin. As a whole, these results help to confirm and complement the findings from Figure 6-8.

Because the results from the NIR microscopy and immunohistochemistry studies did not show a direct correlation between mitochondrial density and NIR autofluorescence, another study was performed in order to verify these findings with further emphasis on human skeletal muscle and STS. In this experiment, mitochondria isolated samples from *ex vivo* human skeletal muscle and STS samples were stained with a mitochondria stain, Mitotracker Green, and measured using flow cytometry. Here, both mitotracker stained and unstained samples from the same tissue block were measured at two excitation emission channels. The first channel consisting of a 488 nm excitation and fluorescence measurements at 530 nm was used to specifically target Mitotracker Green fluorescence, while the 2$^{nd}$ channel consisting of a 405 nm excitation and 650 nm emission was used to target PpIX fluorescence.[34] From the results seen in Figure 6-10, it can be seen that the

STS sample actually exhibited a higher fluorescence intensity in the 488 nm excitation channel which suggests a higher mitochondrial concentration in the STS compared to skeletal muscle. Conversely, the skeletal muscle sample exhibited a higher fluorescence signal in the 405 nm excitation channel which suggests that skeletal muscle may have a higher PpIX concentration than STS if PpIX is truly the fluorophore of interest. Both results are consistent with those seen earlier in Figure 6-1, Figure 6-4, Figure 6-7, and Figure 6-8 that have suggested a higher NIR autofluorescence in skeletal muscle despite a higher mitochondria density in STS and further provides evidence of PpIX related NIR autofluorescence.

With many of the results described earlier providing evidence towards the PpIX hypothesis, further experiments were done with the intent of affecting the NIR autofluorescence signal. In the first set of experiments, a PpIX DMF:MeOH sample was separately incubated in a solution of $H_2O_2$ and a solution of bleach while measured by NIR autofluorescence imager. As seen in Figure 6-11, the PpIX sample originally exhibited a strong NIR autofluorescence signal. After 24 hours of incubation with $H_2O_2$ and bleach, there was a significant decrease in NIR signal from the original starting value, suggesting that PpIX NIR autofluorescence can be negatively affected by both solutions separately. This procedure was then repeated with protein denatured skeletal muscle which resulted in similar results as seen in Figure 6-12 in which a strong NIR autofluorescence was originally observed but was significantly decreased after incubation with bleach or $H_2O_2$. It is known that in an *in vivo* environment, heme degradation occurs via two pathways: an enzymatic pathway through heme oxygenase, and a non-enzymatic pathway mediated by a reactive oxygen species such as $H_2O_2$ [61] or hypochlorous acid, which sodium hypochlorite is a major component of bleach.[62] In both scenarios, the degradation occurs through the production of reactive oxygen species that unselectively cleaves any of the four meso-carbon bridges inherent to the PpIX

structure. HOCl, in particular, is known to oxidatively cleave carbon-carbon double bonds in the pyrrole ring itself, causing an opening or forming the corresponding mono and dipyrrole derivatives.[62] While reactive oxygen species can cause damage to many other things including DNA, RNA, lipids, and proteins, the results presented here are still supportive of the PpIX hypothesis as it demonstrates that the NIR fluorescence signal can be chemically deactivated despite the unknown fluorophore's robustness to formalin, proteinase, heating, and ethanol.

Finally, an experiment was performed to study the NIR fluorescence effects of removing the iron ion present in hemoglobin and myoglobin and reverting the samples back to their PpIX precursor. To do this, a "one-pot single-phase" method described by Sayyad *et al* was utilized. Through this method, the water-pyridine solvent mixture dissociates the iron ions from the pockets of the porphyrin rings along with the globular proteins. The results of this experiment can be seen in Figure 6-13 where porcine hemoglobin, human hemoglobin, and horse myoglobin samples originally begin with low NIR autofluorescence intensities, but exhibit a significant increase in signal following incubation in the pyridine and DTT solution, further providing evidence for the PpIX hypothesis. Interestingly, the intensities of the porcine and human hemoglobin samples are similar to one another, but the horse myoglobin signal is nearly half of the hemoglobin samples despites all samples being prepared at the same concentration. This is may be due to hemoglobin having four heme groups whereas myoglobin only has one. Whether or not the NIR fluorescence of PpIX scales linearly with concentration or is subject to a self-shielding[63] "inner-cell-effect" is currently unknown, but the significant difference between fluorescence signals generated from hemoglobin and myoglobin samples after iron removal further suggests that the unknown NIR fluorophore is PpIX as there are few other differences between hemoglobin and myoglobin.

As a whole, the results presented above provide multiple evidence supporting the hypothesis that PpIX fluorescence beyond 800 nm maybe the biological basis behind the spectral marker that was previously used to differentiate between STS from the normal muscle and fat as observed in a previous study.[17] These evidence, however, are not concrete as each experiment and device used in this study are inherently limited in their scope of measurement. Instruments such as the wide-field fluorescence imager can only excite at a single wavelength and gather spectrally integrated measurements in the NIR, while other systems such as the gel fluorescence scanner and the spectrofluorometer have excitations and detections that are much more sensitive to the visible regime. Modalities such as HPLC and mass spectroscopy can be used to specifically detect PpIX in samples, but does not simultaneously verify its NIR fluorescence. Thus while each independent modality can verify the existence of PpIX in one way another, there currently does not exist a single modality that can measure every single needed parameter at the same time to simultaneously correlate the visible to NIR spectral profile, spatial location, and molecular weight required to confirm the PpIX hypothesis. This is further complicated by the heterogeneity of both skeletal muscle and STS subtypes as previous studies have shown that their NIR fluorescence signals can be quite variable.[17] For this reason, future studies would have to be tightly controlled to a limited number of tissue samples. For example, utilizing the methods used in this manuscript for studying the effects of Abcb10[64] knockout and ALA on PpIX accumulation may provide a more conclusive evidence of PpIX NIR autofluorescence. For the time being, however, the fluorescence differences can be confidently attributed to endogenous hematoporphyrins including PpIX.

## 6.6 Conclusion

The results presented in this study confirm the findings from previous work that human skeletal muscle has a high NIR autofluorescence signal compared to STS or fat and provides evidence across multiple modalities that the source of the signal may be from mitochondrial PpIX. Our study shows that *ex vivo* samples of PpIX does indeed fluorescence in the near infrared, while other products of heme synthesis including heme and biliverdin do not. In addition, the fluorophore was shown to be robust and most likely small molecule-based, allowing for the study of liquid protein denatured samples through modalities such as spectrofluorimetry, HPLC, mass spectroscopy, and flow cytometry. All of these studies provide evidence pointing towards the PpIX hypothesis based on similarities in spectra and molecular mass. Immunohistochemistry and microscopy studies were able to show that the fluorescence signal most likely originates from cellular mitochondria, which is where PpIX synthesis occurs. However, no relation was found between mitochondria concentration and PpIX fluorescence intensity. Finally, experiments were also able to demonstrate the how fluorescence signals could be decreased through porphyrin degradation. It was also demonstrated that non-fluorescing hemoglobin and myoglobin samples could be made to fluoresce by reverting the samples back to its PpIX precursor. While many of these studies are highly suggestive of confirming the PpIX hypothesis, it is not certain enough to identify PpIX as the source of NIR autofluorescence differences between human skeletal muscle, STS, and fat but at least suggests a hematoporphyrin origin.

## 6.7 Acknowledgements

We would like to acknowledge the staff at the Vanderbilt University Medical Center Translational Pathology Shared Resource for their assistance regarding the immunohistochemistry used in his study. We would also like to acknowledge Dr. Wade Calcutt from the Vanderbilt University Medical Center's Mass Spectrometry Core for his assistance and expert advice regarding the HPLC and mass spectroscopy measurements. Finally, we would like to thank Mr. Christian M. Warren from the Vanderbilt University Flow Cytometry Shared Resource for his assistance and expert advice regarding the flow cytometry measurements.

## 6.8 Funding Sources

National Cancer Institute (NCI) (1F31CA200358); Orthopaedic Research and Education Foundation/Musculoskeletal Tumor Society Clinical Research Grant in Orthopaedic Oncology; Vanderbilt Orthopaedic Institute.

## 6.9 References


1. Hollon, T., Hervey-Jumper, S. L., Sagher, O. & Orringer, D. A. Advances in the Surgical Management of Low-Grade Glioma. *Seminars in radiation oncology* **25**, 181-188, doi:10.1016/j.semradonc.2015.02.007 (2015).
2. Stummer, W. *et al.* Fluorescence-guided surgery with 5-aminolevulinic acid for resection of malignant glioma: a randomised controlled multicentre phase III trial. *The Lancet. Oncology* **7**, 392-401, doi:10.1016/S1470-2045(06)70665-9 (2006).
3. Mothes, H. *et al.* Indocyanine-green fluorescence video angiography used clinically to evaluate tissue perfusion in microsurgery. *The Journal of trauma* **57**, 1018-1024 (2004).
4. Brunworth, L. S., Samson, M. C., Newman, M. I. & Ramirez, J. R. Nipple-areola complex evaluation in long pedicled breast reductions with real-time fluorescent videoangiography. *Plastic and reconstructive surgery* **128**, 585-586; author reply 586-587, doi:10.1097/PRS.0b013e31821e71f6 (2011).
5. Lin, W. C., Toms, S. A., Motamedi, M., Jansen, E. D. & Mahadevan-Jansen, A. Brain tumor demarcation using optical spectroscopy; an in vitro study. *Journal of biomedical optics* **5**, 214-220, doi:10.1117/1.429989 (2000).
6. Lin, W. C., Toms, S. A., Johnson, M., Jansen, E. D. & Mahadevan-Jansen, A. In vivo brain tumor demarcation using optical spectroscopy. *Photochemistry and photobiology* **73**, 396-402 (2001).
7. Chung, Y. G., Schwartz, J. A., Gardner, C. M., Sawaya, R. E. & Jacques, S. L. Diagnostic potential of laser-induced autofluorescence emission in brain tissue. *Journal of Korean medical science* **12**, 135-142 (1997).
8. Bottiroli, G. *et al.* Brain tissue autofluorescence: an aid for intraoperative delineation of tumor resection margins. *Cancer detection and prevention* **22**, 330-339 (1998).
9. Zellweger, M. *et al.* In vivo autofluorescence spectroscopy of human bronchial tissue to optimize the detection and imaging of early cancers. *Journal of biomedical optics* **6**, 41-51, doi:10.1117/1.1332774 (2001).
10. Richards-Kortum, R. *et al.* Spectroscopic diagnosis of colonic dysplasia. *Photochemistry and photobiology* **53**, 777-786 (1991).

11. Ramanujam, N. *et al.* Cervical precancer detection using a multivariate statistical algorithm based on laser-induced fluorescence spectra at multiple excitation wavelengths. *Photochemistry and photobiology* **64**, 720-735 (1996).
12. D'Hallewin, M. A., Baert, L. & Vanherzeele, H. Fluorescence imaging of bladder cancer. *Acta urologica Belgica* **62**, 49-52 (1994).
13. Panjehpour, M. *et al.* Spectroscopic diagnosis of esophageal cancer: new classification model, improved measurement system. *Gastrointest Endosc* **41**, 577-581 (1995).
14. Chwirot, B. W., Chwirot, S., Redzinski, J. & Michniewicz, Z. Detection of melanomas by digital imaging of spectrally resolved ultraviolet light-induced autofluorescence of human skin. *European journal of cancer* **34**, 1730-1734 (1998).
15. Gupta, P. K., Majumder, S. K. & Uppal, A. Breast cancer diagnosis using N2 laser excited autofluorescence spectroscopy. *Lasers in surgery and medicine* **21**, 417-422 (1997).
16. Warren, S. *et al.* Combined ultrasound and fluorescence spectroscopy for physico-chemical imaging of atherosclerosis. *IEEE transactions on bio-medical engineering* **42**, 121-132, doi:10.1109/10.341824 (1995).
17. Nguyen, J. Q. *et al.* Near-infrared autofluorescence spectroscopy of in vivo soft tissue sarcomas. *Optics letters* **40**, 5498-5501, doi:10.1364/OL.40.005498 (2015).
18. Richards-Kortum, R. & Sevick-Muraca, E. Quantitative optical spectroscopy for tissue diagnosis. *Annual review of physical chemistry* **47**, 555-606, doi:10.1146/annurev.physchem.47.1.555 (1996).
19. Lakowicz, J. R. *Principles of Fluorescence Spectroscopy*. 3rd edn, (Springer US, 2006).
20. Smith, K. C. *The Science of Photobiology*. Second edn, (Plenum Press, 1989).
21. Zhang, G., Demos, S. G. & Alfano, R. R. Far-red and NIR spectral wing emission from tissues under 532 and 632 nm photo-excitation. *Lasers in the Life Sciences* **9**, 1-16 (1999).
22. Demos, S. G., Bold, R., White, R. V. & Ramsamooj, R. Investigation of near-infrared autofluorescence imaging for the detection of breast cancer. *IEEE Journal of Selected Topics in Quantum Electronics* **11**, 791 - 798, doi:10.1109/JSTQE.2005.857682 (2005).
23. Huang, Z., Lui, H., McLean, D. I., Korbelik, M. & Zeng, H. Raman spectroscopy in combination with background near-infrared autofluorescence enhances the in vivo assessment

of malignant tissues. *Photochemistry and photobiology* **81**, 1219-1226, doi:10.1562/2005-02-24-RA-449 (2005).

24. Fournier, L. S. *et al.* In-vivo NIR autofluorescence imaging of rat mammary tumors. *Optics express* **14**, 6713-6723 (2006).
25. Shao, X., Zheng, W. & Huang, Z. Near-infrared autofluorescence spectroscopy for in vivo identification of hyperplastic and adenomatous polyps in the colon. *Biosensors & bioelectronics* **30**, 118-122, doi:10.1016/j.bios.2011.08.040 (2011).
26. Wishart, D. S. *et al.* HMDB 3.0--The Human Metabolome Database in 2013. *Nucleic acids research* **41**, D801-807, doi:10.1093/nar/gks1065 (2013).
27. Wishart, D. S. *et al.* HMDB: a knowledgebase for the human metabolome. *Nucleic acids research* **37**, D603-610, doi:10.1093/nar/gkn810 (2009).
28. Wishart, D. S. *et al.* HMDB: the Human Metabolome Database. *Nucleic acids research* **35**, D521-526, doi:10.1093/nar/gkl923 (2007).
29. Kennedy, J. C., Marcus, S. L. & Pottier, R. H. Photodynamic therapy (PDT) and photodiagnosis (PD) using endogenous photosensitization induced by 5-aminolevulinic acid (ALA): mechanisms and clinical results. *Journal of clinical laser medicine & surgery* **14**, 289-304, doi:10.1089/clm.1996.14.289 (1996).
30. Peng, Q. *et al.* 5-Aminolevulinic acid-based photodynamic therapy. Clinical research and future challenges. *Cancer* **79**, 2282-2308 (1997).
31. Peng, Q., Berg, K., Moan, J., Kongshaug, M. & Nesland, J. M. 5-Aminolevulinic acid-based photodynamic therapy: principles and experimental research. *Photochemistry and photobiology* **65**, 235-251 (1997).
32. Brown, S. B., Brown, E. A. & Walker, I. The present and future role of photodynamic therapy in cancer treatment. *The Lancet. Oncology* **5**, 497-508, doi:10.1016/S1470-2045(04)01529-3 (2004).
33. Gibbs, S. L. *et al.* Protoporphyrin IX level correlates with number of mitochondria, but increase in production correlates with tumor cell size. *Photochemistry and photobiology* **82**, 1334-1341, doi:10.1562/2006-03-11-RA-843 (2006).
34. Valentine, R. M., Ibbotson, S. H., Wood, K., Brown, C. T. & Moseley, H. Modelling fluorescence in clinical photodynamic therapy. *Photochemical & photobiological sciences :*

*Official journal of the European Photochemistry Association and the European Society for Photobiology* **12**, 203-213, doi:10.1039/c2pp25271f (2013).

35. Schindelin, J. *et al.* Fiji: an open-source platform for biological-image analysis. *Nature methods* **9**, 676-682, doi:10.1038/nmeth.2019 (2012).
36. Sayyad, A. S. *et al.* Synthesis of iron nanoparticles from hemoglobin and myoglobin. *Nanotechnology* **23**, 055602, doi:10.1088/0957-4484/23/5/055602 (2012).
37. Stein, S. E. in *NIST Chemistry WebBook, NIST Standard Reference Database Number 69* (eds P.J. Linstrom & W.G. Mallard) (National Institute of Standards and Technology).
38. Ghosh, S. *et al.* Blue protein with red fluorescence. *Proceedings of the National Academy of Sciences of the United States of America* **113**, 11513-11518, doi:10.1073/pnas.1525622113 (2016).
39. Zhang, Y., Li, B. & Jin, Y. Label-free fluorescent detection of thrombin using G-quadruplex-based DNAzyme as sensing platform. *The Analyst* **136**, 3268-3273, doi:10.1039/c1an00002k (2011).
40. Ajioka, R. S., Phillips, J. D. & Kushner, J. P. Biosynthesis of heme in mammals. *Biochimica et biophysica acta* **1763**, 723-736, doi:10.1016/j.bbamcr.2006.05.005 (2006).
41. Albani, J. R. *Structure and Dynamics of Macromolecules: Absorption and Fluorescence Studies*. (Elsevier Science, 2004).
42. Maines, M. D. Overview of heme degradation pathway. *Current protocols in toxicology* **Chapter 9**, Unit 9 1, doi:10.1002/0471140856.tx0901s00 (2001).
43. Bancroft, J. D. & Gamble, M. *Theory and Practice of Histological Techniques*. 6th edn, (Churchill Livingstone, 2007).
44. Ryter, S. W. & Tyrrell, R. M. The heme synthesis and degradation pathways: role in oxidant sensitivity. Heme oxygenase has both pro- and antioxidant properties. *Free radical biology & medicine* **28**, 289-309 (2000).
45. Weiss, A. *et al.* Organization of human and mouse skeletal myosin heavy chain gene clusters is highly conserved. *Proceedings of the National Academy of Sciences of the United States of America* **96**, 2958-2963 (1999).

46. Horak, V. A successive histochemical staining for succinate dehydrogenase and "reversed"-ATPase in a single section for the skeletal muscle fibre typing. *Histochemistry* **78**, 545-553 (1983).
47. Nemeth, P. & Pette, D. Succinate dehydrogenase activity in fibres classified by myosin ATPase in three hind limb muscles of rat. *The Journal of physiology* **320**, 73-80 (1981).
48. Koves, T. R. *et al.* Subsarcolemmal and intermyofibrillar mitochondria play distinct roles in regulating skeletal muscle fatty acid metabolism. *American journal of physiology. Cell physiology* **288**, C1074-1082, doi:10.1152/ajpcell.00391.2004 (2005).
49. Jonkers, R. A. *et al.* Myofibrillar distribution of succinate dehydrogenase activity and lipid stores differs in skeletal muscle tissue of paraplegic subjects. *American journal of physiology. Endocrinology and metabolism* **302**, E365-373, doi:10.1152/ajpendo.00270.2011 (2012).
50. Palmer, J. W., Tandler, B. & Hoppel, C. L. Biochemical properties of subsarcolemmal and interfibrillar mitochondria isolated from rat cardiac muscle. *The Journal of biological chemistry* **252**, 8731-8739 (1977).
51. Riva, A. *et al.* Structure of cristae in cardiac mitochondria of aged rat. *Mechanisms of ageing and development* **127**, 917-921, doi:10.1016/j.mad.2006.09.002 (2006).
52. Moyes, C. D. & Hood, D. A. Origins and consequences of mitochondrial variation in vertebrate muscle. *Annual review of physiology* **65**, 177-201, doi:10.1146/annurev.physiol.65.092101.142705 (2003).
53. Freyssenet, D., Berthon, P. & Denis, C. Mitochondrial biogenesis in skeletal muscle in response to endurance exercises. *Archives of physiology and biochemistry* **104**, 129-141, doi:10.1076/apab.104.2.129.12878 (1996).
54. Hoppeler, H. Exercise-induced ultrastructural changes in skeletal muscle. *International journal of sports medicine* **7**, 187-204, doi:10.1055/s-2008-1025758 (1986).
55. Suarez, R. K. Upper limits to mass-specific metabolic rates. *Annual review of physiology* **58**, 583-605, doi:10.1146/annurev.ph.58.030196.003055 (1996).
56. Essig, D. A. Contractile activity-induced mitochondrial biogenesis in skeletal muscle. *Exercise and sport sciences reviews* **24**, 289-319 (1996).
57. Moyes, C. D., Battersby, B. J. & Leary, S. C. Regulation of muscle mitochondrial design. *The Journal of experimental biology* **201**, 299-307 (1998).

58. Collins, T. J., Berridge, M. J., Lipp, P. & Bootman, M. D. Mitochondria are morphologically and functionally heterogeneous within cells. *The EMBO journal* **21**, 1616-1627, doi:10.1093/emboj/21.7.1616 (2002).
59. Seo, A. Y. *et al.* Mitochondrial iron accumulation with age and functional consequences. *Aging cell* **7**, 706-716 (2008).
60. Patti, M. E. & Corvera, S. The role of mitochondria in the pathogenesis of type 2 diabetes. *Endocrine reviews* **31**, 364-395, doi:10.1210/er.2009-0027 (2010).
61. Nagababu, E. & Rifkind, J. M. Heme degradation by reactive oxygen species. *Antioxidants & redox signaling* **6**, 967-978, doi:10.1089/ars.2004.6.967 (2004).
62. Maitra, D. *et al.* Mechanism of hypochlorous acid-mediated heme destruction and free iron release. *Free radical biology & medicine* **51**, 364-373, doi:10.1016/j.freeradbiomed.2011.03.040 (2011).
63. Yuan, B., Chen, N. & Zhu, Q. Emission and absorption properties of indocyanine green in Intralipid solution. *Journal of biomedical optics* **9**, 497-503, doi:10.1117/1.1695411 (2004).
64. Yamamoto, M. *et al.* Abcb10 role in heme biosynthesis in vivo: Abcb10 knockout in mice causes anemia with protoporphyrin IX and iron accumulation. *Molecular and cellular biology* **34**, 1077-1084, doi:10.1128/MCB.00865-13 (2014).

# CHAPTER 7

# SUMMARY AND CONCLUDING REMARKS

## 7.1 Summary of Dissertation and Major Conclusions

Soft tissue sarcomas (STS) are a rare and heterogeneous group of malignant tumors that arise from mesenchymal progenitors for a variety of tissue types including muscle, fat, cartilage, blood vessels, and nerves.[1] Because of this, there are over 50 different subtypes of STS each with their own name, classification, and prognosis. Yet despite the vast heterogeneity of subtypes, many STS's often physically present in a similar manner as a localized mass that can develop anywhere in the body and is often treated through surgical resection and radiation. According to the American Cancer Society's report for 2017, there were 12,390 new cases of STS and about 4,990 deaths resulting from STS last year in the United States alone.[2] By the numbers, STS is a relatively rare disease that accounts for less than 1% of all new cancers each year which makes it a difficult disease to study *in vivo* without access to a National Cancer Institute (NCI) Designated Cancer Center. Regardless of its rate of incidence, STS poses an interesting problem in that since 1974, the overall 5 year survival rate of an STS patient following treatment has generally lingered around 60% while treatment methods have not dramatically changed.[3,4] Incomplete resection of STS has been shown to be a primary cause of local recurrence which can lead to amputations and overall decreased survival rates within patients. The problem, however, is that current margin assessment techniques are limited by time and spatial sampling errors with definitive margin statuses often being determined days to weeks after the actual surgery. This dissertation was proposed to address those aforementioned limitations through the development of an intraoperative optical system for

the quick, automated, cost effective, and non-destructive assessment of tumor beds during STS excisions.

The hypothesis that forms the basis of this dissertation is the idea that near-infrared (NIR) autofluorescence imaging in combination with Raman spectroscopy could provide differential diagnoses of STS and surrounding tissues with high sensitivity and specificity without the use of exogenous contrast agents and only relying on signals that naturally occur within the human body. Three specific aims were proposed and investigated. The first specific aim was to intraoperatively acquire measurements from patients undergoing STS resections in order to characterize the optical signatures of STS and surrounding tissues *in vivo*. From there, the results of specific aim 1 was used in specific aim 2 to guide the design and development of a new optical device for evaluating a large surface area within the tumor bed, and finally, a third specific aim was proposed in order to investigate the biological basis that allowed for spectral differentiation of tissue types as seen in specific aims 1 and 2.

The first specific aim was to characterize the optical signatures of STS and surrounding tissues *in vivo*. From the work described in Chapter 3, intraoperative probe-based NIR autofluorescence measurements were acquired from 30 patients undergoing STS resection and were characterized to differentiate between normal tissue and STS.[5] Overall, normal muscle and fat were observed to have the highest and lowest autofluorescence intensities, respectively, with STS falling in between. Using a multinomial logistic regression based on spectral features such as the area under the curve and general shape of the curvature, a classification algorithm was developed for differentiating tissue types which was then tested using a leave-one-patient-out validation technique. With that exclusion of well-differentiated liposarcomas, the algorithm's accuracy for classifying muscle, fat,

and STS was 93%, 92%, and 88% respectively. To our knowledge, this was the first ever NIR autofluorescence study of STS within human patients *in vivo*, and the findings demonstrate NIR autofluorescence spectroscopy's potential as a rapid and non-destructive surgical guidance tool that can inform surgeons of suspicious margins in need of immediate re-excision.

In Chapter 4, the optical signatures of *in vivo* STS and its surrounding tissues were characterized using Raman spectroscopy.[6] Twenty eight patients with confirmed malignant tumors were measured using a probe based Raman spectroscopy system. Due to the large amount of data acquired, an outlier detection algorithm was developed based on principal component analysis and Mahalanobis distance thresholding in order to automatically and non-subjectively exclude measurements with aberrant spectra. From there, a multivariate classification algorithm known as sparse multinomial logistic regression (SMLR) was utilized in order to perform spectral feature reduction, predictive classifier training, and cross validation. With the exclusion of well-differentiated liposarcomas, the algorithm was able to classify STS from the surrounding normal muscle and fat with a sensitive and specify of 89.5% and 96.4% respectively. In addition, SMLR was also used to generate a quantitative metric known as feature importance (FI) to assess the relative merit of the spectral features identified for classification. From this, it was found that Raman peaks near 1,643 and 1,265 $cm^{-1}$ along with the region between 750 and 876 $cm^{-1}$ could be potential indicators for protein differences between cancerous and non-cancerous tissue. Thanks to the number of subtypes measured, different Raman spectra could be observed for STS's at various phases of differentiation and further emphasizes the biochemical specificity of Raman spectroscopy. Most importantly however, this study along with the study in Chapter 4 further lead to the design and development of an intraoperative wide-field NIR fluorescence imaging

platform that could be combined with probe based Raman spectroscopy for the purpose of STS margin assessment.

The second specific aim, the work of which comprises Chapter 5, details the design, development, and testing of a modular fluorescence overlay tissue imaging system for wide-field intraoperative surgical guidance. Known as the Overlay Tissue Imaging System (OTIS), this tool was designed to expand upon the work detailed in Chapter 3 while creating a platform to support future endeavors in intraoperative fluorescence imaging, contrast agent based or otherwise. OTIS is comprised of commercially available standardized components and its modular layout allows for the accommodation of a broad range of fluorophores, field of views (FOV), and spatial resolutions while maintaining a portable design for intraoperative use. Measurements are automatic, quantitative, and feature a real-time projection overlay technique that intuitively displays fluorescence maps directly into a 15 x 15 $cm^2$ FOV from a working distance of 35 cm. At a 20 ms exposure time, 10 μM samples of indocyanine green (ICG) could be measured with high signal to noise which was then validated in an *in vivo* mouse model before finally being demonstrated for intraoperative autofluorescence imaging of human soft tissue sarcoma margins. The OTIS's modular design and ability to enable naked-eye visualization of fluorescence allows for the flexibility to adapt to numerous clinical applications including STS margin assessment, and can potentially extend the adoption of fluorescence imaging for intraoperative use.

The third specific aim, the work of which comprises Chapter 6, was to investigate the biochemical and morphological basis responsible for the differences in NIR autofluorescence intensities observed in the work presented in Chapters 3 and 4. While many other groups in the past have postulated that the spectral tail-end emission of protoporphyrin IX (PpIX) could be the source of

NIR autofluorescence in tissues, up till now, there has not been a single study aimed at evaluating the hypothesis. In Chapter 6, this hypothesis was explored through a variety of different experiments on *ex vivo* human tissues and heme byproducts in order to characterize the unknown NIR fluorophore and potentially confirm PpIX as the biological source of NIR autofluorescence differences between STS, normal muscle, and fat. PpIX NIR autofluorescence was verified, and various experiments were able to determine that the unknown fluorophore is a robust small molecule with a fluorescence profile in the visible wavelength regime similar to the known spectra for PpIX. The fluorescence intensity was shown to correlate with PpIX concentrations as determined by high pressure liquid chromatography, two different methods of mass spectroscopy, and flow cytometry. In addition, the fluorophore was found to be negatively affected by hydrogen peroxide and hypochlorous acid, both of which are involved in natural heme degradation. Conversely, methods to revert heme products back to PpIX were found to restore NIR fluorescence. Finally, microscopy and immunohistochemistry studies suggests that the fluorescence signal is localized within cellular mitochondria where PpIX is known to be synthesized, however, a correlation between mitochondria content and PpIX was not found. Despite the findings across multiple areas of research, it is still not conclusive if PpIX is truly the source of NIR autofluorescence observed in previous studies. At the very least, a porphyrin origin is suggested and further studies are required to determine a definitive answer.

The dissertation presented herein describes work and findings which help form the foundation of NIR Raman and autofluorescence spectroscopy as both a research and clinical tool for the investigation of STS margins without the use of exogenous contrast agents.

## 7.2 Recommendations and Future Directions

Throughout the process of developing and implementing the methodologies to accomplish the goals of this dissertation, various limitations were identified. With the groundwork already planted, the following recommendations represent a number of opportunities for future work and exploration that can offer opportunities for advancement in each area of study:

### *7.2.1 Intraoperative Raman and Autofluorescence Spectroscopy of STS*

As mentioned before, STS is a rare and heterogeneous group of malignant tumors with over 50 different subtypes each with their own classification and prognosis. In addition, tumor beds themselves are quite heterogeneous and can consist of nerves, large blood vessels, lymph nodes, and connective tissues in addition to the muscle and fat explored previously. Both these factors greatly complicate the development of a truly robust margin detection algorithm without a large representative training data for each tissue type along with STS at each stage of development. As the studies described in chapters 3 and 4 were not powered for subtype differentiation, the first major recommendation would be to continue intraoperative Raman and autofluorescence measurements in STS patients and maybe even explore the use of human sarcoma models in animals to help supplement the process. Human sarcoma models in animals would also help to verify intraoperative measurements since a major roadblock of the Raman spectroscopy study were related to the effects of outliers that may have been partially due to spatial sampling errors inherent to single spot probe based measurements .While time consuming, the acquisition of a larger data set would allow for the in-depth studies required for the differentiation between well-differentiated liposarcomas and normal fat that was shown to be difficult from our previous studies. From a

basic science standpoint, the acquisition of a larger data set would also allow for the investigation into the optical property changes during STS differentiation that was hinted towards in Chapter 4.

In order to take advantage of the tissue spectra database, it may also be beneficial to explore a more advanced method for tissue type classification. Complex multivariate and machine learning methods have been studied in the past including support vector machines[7] and neural network models.[8] Similar to SMLR, these techniques allow for the integration of non-Gaussian constraints and variable weighting to optimize classification performance. However, it is not yet clear if this could lead to significant improvements in diagnostic performance and training time compared to the methods used in this dissertation. In addition, it may be worthwhile to leverage the power of cluster computing services such as the Vanderbilt University Advanced Computing Center for Research & Education (ACCRE) in order to decrease the time limitations associated with model training and validation.

### *7.2.2 Advancement of the Overlay Tissue Imaging System (OTIS)*

The groundwork for the OTIS described in this dissertation was originally established by McWade *et al* and her work on intraoperative parathyroid imaging.[9] The original NIR autofluorescence imaging system developed for that project was constrained to a small FOV of approximately 5 by 5 $cm^2$. The system presented here has a much larger FOV at approximately 15 x 15 $cm^2$ which inherently brings additional challenges. While critical problems such as angle-of-incidence blue shifting, real-time computation requirements, and planar image correction have been addressed, there still exists a limitation associated with the measurement of samples with varying surface topography. In order to ensure artifact free quantitative measurements and projection mapping without the use of physical fiducials, it may be of interest to utilize OTIS's digital light projector

for a technique known as fringe-phase profilometry.[10,11] The topographic maps generated could then be utilized for height intensity and projection mapping correction.[12]

Another recommendation would also be to increase the excitation power of the illumination light source. At a distance of 35 cm away and an illumination diameter of over 15 cm, the recorded irradiance at the sample's surface is only 0.6 $mW/cm^2$ despite the laser diode itself outputting over 500 mW of power. While the theoretical interrogation depth of a 785 nm light source should be greater than that of the visible or ultraviolet light commonly used in fluorescence imaging due to the low absorption and scattering of NIR light in tissue, a low irradiance may still confine OTIS measurements to a superficial portion of the sample. This in combination with the challenges posed by varying surface topography can also effect the signal to noise ratio (SNR) for samples that are beyond the device's plane of focus. However, because the OTIS was designed to be modular, the laser diode currently being used could potentially be replaced with much more powerful light source such as an actively cooled LED array configured for homogenous illumination.

Another limitation of the OTIS is its inability for combined autofluorescence imaging and Raman spectroscopy in a timely manner. In its current iteration where each modality resides in two separate hardware and software configurations while occupying space on the same intraoperative platform, the time required to acquire a small set of combined measurements in the operating room is over 30 minutes and greatly restricts data collection even for research purposes. Due to the specialized equipment required for Raman spectroscopy, it may not be possible to design and build a single combined system in the short term. However, it may be possible to connect both instruments together using a single streamlined software to overcome the complexities associated with juggling two different acquisitions simultaneously.

### *7.2.3 Porphyrin NIR Tail-End Fluorescence*

The study described in Chapter 6 originally began as a fluorophore characterization before it eventually evolved into having a testable hypothesis in PpIX. Over the course of the study, there were a few major developments that made this possible. First was the design and construction of the wide-field NIR autofluorescence imaging system in specific aim 2 which allowed for the rapid and non-contact evaluation of samples as soon as they were prepared. The second most important discovery was that the unknown fluorophore was most likely a robust small molecule rather than a protein. This allowed for the development of a robust protocol for producing liquid fluorophore isolated samples from a variety of hard *ex vivo* tissues which could then be investigated using a myriad of techniques such as spectrofluorimetry, HPLC, two forms of mass spectroscopy, and flow cytometry. The third most important discovery was that the fluorophore was not affected by the formalin fixation and paraffin embedding process required for histopathology. This allowed for NIR fluorescence microscopy studies along with studies involving immunohistochemical staining.

Despite all the developments and discoveries made, it is still unclear if PpIX is definitively the source of NIR autofluorescence observed in previous studies. Each experiment and device used in this study was inherently limited in their scope of measurement. Instruments such as the wide-field fluorescence imager can only excite at a single wavelength and gather spectrally integrated measurements in the NIR, while other systems such as the gel fluorescence scanner and the spectrofluorometer have excitations and detections ranges that are much more sensitive within the ultraviolet to visible wavelength regimes. Modalities such as HPLC and mass spectroscopy can be used to specifically detect PpIX in samples based on molecular weight and fragmentation, but does not simultaneously verify its NIR fluorescence. Thus while each independent modality can

verify the existence of PpIX in one way another, there currently does not exist a single modality that can measure every needed parameter at the same time to simultaneously correlate the visible to near infrared spectral profile, spatial location, and molecular weight required to confirm the PpIX hypothesis. This is further complicated by the heterogeneity of both skeletal muscle and STS subtypes as previous studies have shown that their NIR fluorescence signals can be quite variable.[5] For this reason, future studies would have to be tightly controlled to a limited number of tissue. For example, utilizing the methods used in this manuscript for studying the effects of Abcb10[13] knockout and ALA on PpIX accumulation may provide a more conclusive evidence of PpIX NIR autofluorescence. In addition, it is highly recommended that future studies explore NIR autofluorescence properties of other endogenous porphyrins also involved in heme synthesis including coporphyrin III and uroporphyrinogen III, which like PpIX, are conventionally known to have fluorescence excitation and emissions in the visible wavelengths, but have not been characterized in the in the NIR past 800 nm.[14]

### 7.3 Contributions to the Field and Societal Impact

The work that comprises this dissertation is an accumulation of work aimed at the goal of rapid, accurate, and nondestructive intraoperative assessment of STS margins without the use of exogenous contrast agents.

From a biophotonics standpoint, the work presented in Chapters 3 and 4 represent the first ever *in vivo* study of NIR autofluorescence and Raman spectroscopy within patients undergoing STS resections. Due to the rarity of the disease, a large majority of STS optical analysis in the past was limited to *in vitro* and animal studies along with being limited to a single subtype. In addition, while various optical modalities have been explored for disease detection, NIR autofluorescence

has largely been ignored due to the lack of known biological fluorophores beyond the visible wavelengths. However, from the work presented above, the presence of NIR autofluorescence within the human body was observed which then lead to the development of an intraoperative wide-field NIR autofluorescence imaging system with the intent of exploiting that signal for tumor margin assessment. Not only was this signal observed, but was also found to be significantly higher in normal skeletal muscle compared to any other tissue within the tumor bed which allowed for the development of a simple multinomial logistic regression for identifying suspicious tumor margins.

The Raman spectroscopy study of *in vivo* STS tumor beds was also the first even investigation of its kind within human subjects. From the measurements, a multivariate classification algorithm was developed that could automatically identify a small number of spectral features for robustly differentiating between STS and surrounding normal muscle with high sensitivity and specificity. These results by themselves suggests that a device based on Raman spectroscopy could allow for highly specific intraoperative tumor margin assessment, but when combined with the knowledge from the autofluorescence study, helps to provide a basic frame work for approaching tumor bed margin assessment by leading to the development of an intraoperative wide-field NIR autofluorescence imager with the intent of identifying suspicious margins for secondary analysis using Raman spectroscopy. From a cancer research point of view, this study not only demonstrates the potential of vibrational spectroscopy for identifying spectral markers of malignancies, but also for tracking biochemical changes that occur during STS progression and de-differentiation.

The modular fluorescence overlay tissue imaging system for wide-field intraoperative surgical guidance known as OTIS was designed and built based on the findings of the previous

spectroscopic studies. It is unique in that it is capable of serving dual purpose as both a robust lab-based research platform and as an intraoperative surgical guidance tool. OTIS is comprised of affordable readily available standardized commercial components, and at its core, features a modular layout that can be adapted to various applications that are not necessarily related to STS such as indocyanine green monitoring during glioma resections or parathyroid detection during thyroidectomies. In addition, the system features a novel visualization strategy for image guided surgery by projecting fluorescence maps directly onto the imaging surface for the intuitive tracking of both exogenous and endogenous fluorophores in real time without the use of external monitors and the disruption of workflow often associated with it.

Finally, the fluorophore characterization studies represent the first ever investigation into the biological source of NIR autofluorescence within human skeletal muscle, STS, and fat. One of the key observations from our previous studies indicated that normal skeletal muscle exhibited a much stronger NIR autofluorescence signal compared to normal fat or any STS subtype. At the time, the source of the NIR autofluorescence signal was unknown, and porphyrin derivatives were discussed as a possible source since they are currently known to be the longest emitting endogenous fluorophores up to 700 nm. Porphyrin derivatives have been hypothesized to be responsible for differentiation in many other cancer studies,[15-19] yet despite its ubiquity, no group has yet to investigate the role of NIR porphyrin tail-end fluorescence until now. While the PpIX hypothesis originally proposed could not be verified with absolute certainty, the results strongly support the hypothesis or at least the porphyrin origins of the NIR fluorophore. The implications of this work could eventually lead to new applications in diagnostics, therapeutics, and basic science as endogenous porphyrins such as PpIX, coproporphyrin III, and uroporphyrinogen III are precursors in heme synthesis. Should the porphyrin hypothesis be eventually verified, much of

the work in this dissertation could then be used to study other disease and disorders outside the realm of STS where hemoglobin or myoglobin deficiencies may be present.

Throughout this thesis, I have actively studied the use of NIR Raman and autofluorescence spectroscopy for surgical STS margin assessment and have seen firsthand the challenges in translating laboratory research instruments into an intraoperative environment. I've worked with the wonderful orthopedic surgeons and residents of the Vanderbilt University Medical Center and have internalized much of their advice in order to design and build an intraoperative device of my own. As this work continues to develop and become clinically proven, its application could help guide STS resections so that immediate re-excision of suspicious margins can be performed, thus minimizing the necessity for multiple surgeries and their associated risks. In addition, the knowledge gathered from this study could revolutionize the way other sarcomas and tumors are excised by providing surgeons with a tool for accurately identifying and locating residual cancers in real time.

## 7.4 References


1. Demetri, G. D. *et al.* Soft tissue sarcoma. *Journal of the National Comprehensive Cancer Network : JNCCN* **8**, 630-674 (2010).
2. Cancer Facts & Figures 2016. (American Cancer Society, Atlanta, 2016).
3. Pritchard, D. J., Soule, E. H., Taylor, W. F. & Ivins, J. C. Fibrosarcoma--a clinicopathologic and statistical study of 199 tumors of the soft tissues of the extremities and trunk. *Cancer* **33**, 888-897 (1974).
4. Abraham, J. A., Baldini, E. H. & Butrynski, J. E. Management of adult soft-tissue sarcoma of the extremities and trunk. *Expert review of anticancer therapy* **10**, 233-248, doi:10.1586/era.09.193 (2010).
5. Nguyen, J. Q. *et al.* Near-infrared autofluorescence spectroscopy of in vivo soft tissue sarcomas. *Optics letters* **40**, 5498-5501, doi:10.1364/OL.40.005498 (2015).
6. Nguyen, J. Q. *et al.* Intraoperative Raman spectroscopy of soft tissue sarcomas. *Lasers in surgery and medicine* **48**, 774-781, doi:10.1002/lsm.22564 (2016).
7. Barman, I. *et al.* Application of Raman spectroscopy to identify microcalcifications and underlying breast lesions at stereotactic core needle biopsy. *Cancer research* **73**, 3206-3215, doi:10.1158/0008-5472.CAN-12-2313 (2013).
8. Vargis, E. *et al.* Effect of normal variations on disease classification of Raman spectra from cervical tissue. *The Analyst* **136**, 2981-2987, doi:10.1039/c0an01020k (2011).
9. McWade, M. A. *et al.* Label-free intraoperative parathyroid localization with near-infrared autofluorescence imaging. *The Journal of clinical endocrinology and metabolism* **99**, 4574-4580, doi:10.1210/jc.2014-2503 (2014).
10. Srinivasan, V., Liu, H. C. & Halioua, M. Automated phase-measuring profilometry: a phase mapping approach. *Applied optics* **24**, 185 (1985).
11. Srinivasan, V., Liu, H. C. & Halioua, M. Automated phase-measuring profilometry of 3-D diffuse objects. *Applied optics* **23**, 3105 (1984).
12. Gioux, S. *et al.* Three-dimensional surface profile intensity correction for spatially modulated imaging. *Journal of biomedical optics* **14**, 034045, doi:10.1117/1.3156840 (2009).

13. Yamamoto, M. *et al.* Abcb10 role in heme biosynthesis in vivo: Abcb10 knockout in mice causes anemia with protoporphyrin IX and iron accumulation. *Molecular and cellular biology* **34**, 1077-1084, doi:10.1128/MCB.00865-13 (2014).
14. Jope, E. M. & O'Brien J, R. Spectral absorption and fluorescence of coproporphyrin isomers I and III and the melting-points of their methyl esters. *The Biochemical journal* **39**, 239-244 (1945).
15. Zhang, G., Demos, S. G. & Alfano, R. R. Far-red and NIR spectral wing emission from tissues under 532 and 632 nm photo-excitation. *Lasers in the Life Sciences* **9**, 1-16 (1999).
16. Demos, S. G., Bold, R., White, R. V. & Ramsamooj, R. Investigation of near-infrared autofluorescence imaging for the detection of breast cancer. *IEEE Journal of Selected Topics in Quantum Electronics* **11**, 791 - 798, doi:10.1109/JSTQE.2005.857682 (2005).
17. Huang, Z., Lui, H., McLean, D. I., Korbelik, M. & Zeng, H. Raman spectroscopy in combination with background near-infrared autofluorescence enhances the in vivo assessment of malignant tissues. *Photochemistry and photobiology* **81**, 1219-1226, doi:10.1562/2005-02-24-RA-449 (2005).
18. Fournier, L. S. *et al.* In-vivo NIR autofluorescence imaging of rat mammary tumors. *Optics express* **14**, 6713-6723 (2006).
19. Shao, X., Zheng, W. & Huang, Z. Near-infrared autofluorescence spectroscopy for in vivo identification of hyperplastic and adenomatous polyps in the colon. *Biosensors & bioelectronics* **30**, 118-122, doi:10.1016/j.bios.2011.08.040 (2011).

# APPENDIX 1

## Unpublished Tissue Imaging Studies

### A1.1 Introduction

Over the course of forming a hypothesis for specific aim 3 and the work presented in Chapter 6, various imaging studies were performed on *ex vivo* animal samples. Measurements were acquired using the Overlay Tissue Imaging System (OTIS) developed in Chapter 5. The purpose of this appendix is to present those data and provide a discussion that may assist in future studies, particularly with respect to fluorescence differences between different muscle fiber types, groups, and inter-species heterogeneity.

Before delving into the results, it is important to understand the distinctions between different skeletal muscle fiber types and the role of protoporphyrin IX (PpIX). In general, there are two skeletal muscle fiber types: type I and type II.[1] Type I skeletal muscle fibers are oxidative and are known as "slow twitch" muscles that are highly resistant to fatigue. They are characterized by their high capacity for ATP production through oxidative phosphorylation, a dense capillary network, and high levels of intracellular myoglobin. For these reasons, type I skeletal muscle fibers tend to be red and are often utilized for repeated low-level contractions like walking. Based on the results from Chapter 7, it would be hypothesized that type I muscles would have higher concentrations of PpIX due to their myoglobin dependencies. Type II skeletal muscle fibers, on the other hand, are grouped into multiple subtypes that exhibit interspecies heterogeneity based on certain physiological properties. These include type IIA and type IIX in humans (or IIB in other animals). Type IIA, also known as fast oxidative fibers, have moderate resistance to fatigue and represent a

transition between type I and type IIX fiber types. While also mitochondrial rich, they do not contain as much myoglobin as type I fibers and therefore would not be expected to be PpIX rich in comparison. These fibers are often utilized for prolonged anaerobic activities with relatively high output. Finally, there are the fast glycolytic fibers known as type IIB. These skeletal muscle fibers are very sensitive to fatigue and are utilized for short anaerobic high force production activities but are low in mitochondrial and myoglobin content. For this reason, these fibers are often white in color and are not expected to be rich in PpIX.

## A1.2 Results and Discussion

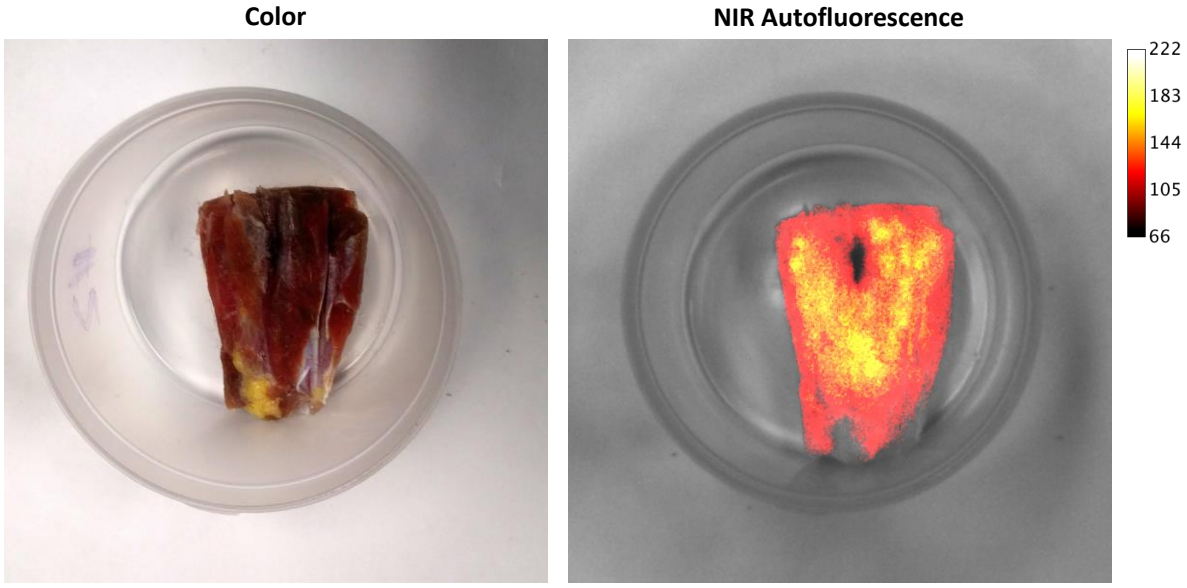


(a) (b)

Figure A1-1: NIR autofluorescence imaging of a squirrel monkey quadricep muscle as measured by OTIS. (a) Color image. (b) NIR autofluorescence image.

Figure A1-1 shows a freshly excised squirrel monkey quadricep muscle sample where it can be observed that the NIR autofluorescence intensity is relatively high throughout. Following formalin

fixation for 24 hours, the NIR autofluorescence was found to not exhibit significant differences, which further added to the small molecule hypothesis expanded upon in Chapter 6. From the literature, it can be generally agreed that squirrel monkeys have larger percentages of skeletal muscle type I fibers that can range up to 71% compared to humans which generally linger around 52% depending on age, health, and athleticism.[2-4] However, due to the similarities between human and primate skeletal muscles, these results suggests that squirrel monkey skeletal muscle samples could substitute if human muscle samples are not acquirable.

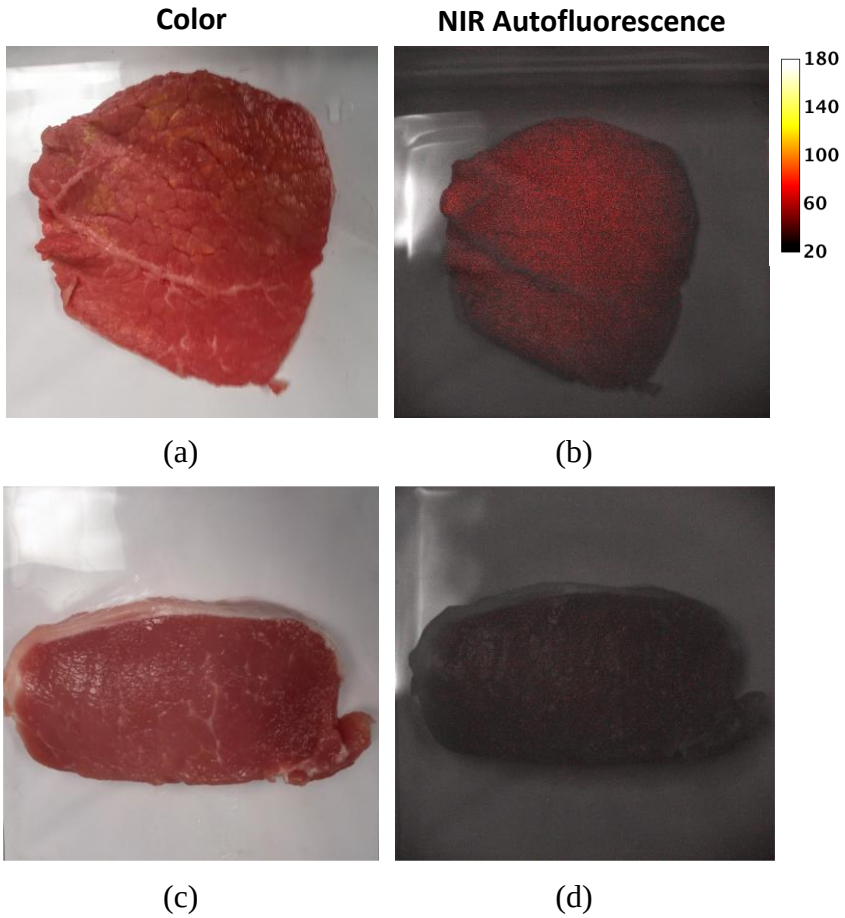


Figure A1-2: NIR autofluorescence imaging of store bought meats as measured by OTIS. (a) Color image of beef rib eye sample. (b) NIR autofluorescence image of beef rib eye sample. (c) Color image of pork loin sample. (d) NIR autofluorescence image of pork loin sample.

The results in Figure A1-2 show the NIR autofluorescence imaging results from two store bought meats from two different animals. Figure A1-2(a, b) were acquired from a beef rib eye sample which is comprised mainly of longissimus with complexus and spinalis muscles that, according to literature, should comprise of approximately 50% type I fiber types depending on animal health.[5] Figure A1-2(b and c) were acquired from a pork loin sample which should comprise mainly of longissimus dorsi muscle and has been estimated in the literature to be comprised of over 80%

type IIB muscle fiber types depending on animal health.[6] From the results seen above, the beef ribeye sample exhibits a much higher NIR autofluorescence compared to the pork loin sample which can probably be attributed to its higher average percentage of type I vs type IIB muscle fiber types. These results are also interesting in that they suggest that non-destructive PpIX measurements through OTIS could potentially be used to assess meat quality for consumption by providing an estimate of type I muscle fiber composition which has been correlated with higher meat quality in terms of flavor, tenderness, and drip loss.[5-9]

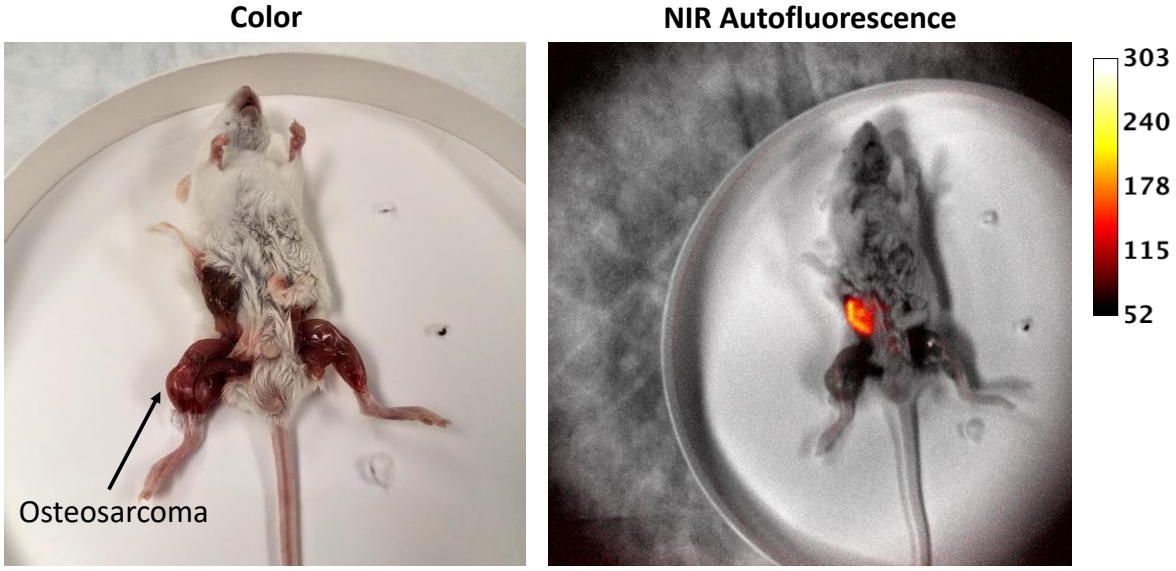


(a) (b)

Figure A1-3: NIR autofluorescence imaging of a mouse osteosarcoma model as measured by OTIS. (a) Color image of mouse sample. (b) NIR autofluorescence image of mouse.

The results in Figure A1-3 show the NIR autofluorescence imaging results from a mouse model grown with K7M human osteosarcoma as obtained from collaborators at the MD Anderson Cancer Center. The motivation for this study was to develop a controlled mouse sarcoma model that could

be used to guide the development of a combined approach to autofluorescence imaging and Raman spectroscopy. At about 4 weeks of age, each mouse was x-rayed to confirm tumor growth and then euthanized prior to dissection and imaging. In total, 6 mice were imaged with similar results to those seen in Figure A1-3 where little to no NIR autofluorescence can be observed in the mouse's exposed skeletal muscles, which greatly diminished the usefulness of the model for its original purpose. The NIR autofluorescence signal observed within the mouse's gastrointestinal region is most likely due to accumulation of pheophorbide a resulting from a chlorophyll rich diet.[10] On the other hand, the reason for the lack of NIR autofluorescence within the mice can possibly be attributed to previous observations from literature that mice are predominately composed of type IIB fiber types with the hind limbs in particular averaging about 76% of this particular fiber type[11] that should not exhibit NIR autofluorescence according to the PpIX hypothesis presented in Chapter 7. In addition, these type II fibers are mainly distributed throughout superficial layers of tissue[11] which are directly interrogated by the OTIS due to its low irradiance and low penetration depth. For these reasons, a mouse tumor model may not be ideal for developing NIR autofluorescence techniques for surgical guidance.

## A1.3 References


1. Jones, D., Round, J. & Haan, A. d. *Skeletal Muscle*. (Churchill Livingstone, 2004).
2. Pierce, L. M. *et al.* Levator ani muscle and connective tissue changes associated with pelvic organ prolapse, parity, and aging in the squirrel monkey: a histologic study. *American journal of obstetrics and gynecology* **197**, 60 e61-69, doi:10.1016/j.ajog.2007.02.037 (2007).
3. Johnson, M. A., Polgar, J., Weightman, D. & Appleton, D. Data on the distribution of fibre types in thirty-six human muscles. An autopsy study. *Journal of the neurological sciences* **18**, 111-129 (1973).
4. Coyle, E. F., Sidossis, L. S., Horowitz, J. F. & Beltz, J. D. Cycling efficiency is related to the percentage of type I muscle fibers. *Medicine and science in sports and exercise* **24**, 782-788 (1992).
5. Ozawa, S. *et al.* The characteristics of muscle fiber types of longissimus thoracis muscle and their influences on the quantity and quality of meat from Japanese Black steers. *Meat science* **54**, 65-70 (2000).
6. Lee, S. H. *et al.* The influence of pork quality traits and muscle fiber characteristics on the eating quality of pork from various breeds. *Meat science* **90**, 284-291, doi:10.1016/j.meatsci.2011.07.012 (2012).
7. Cameron, N. D., Warriss, P. D., Porter, S. J. & Enser, M. B. Comparison of Duroc and British landrace pigs for meat a and eating quality. *Meat science* **27**, 227-247, doi:10.1016/0309-1740(90)90053-9 (1990).
8. Ryu, Y. C. *et al.* Comparing the histochemical characteristics and meat quality traits of different pig breeds. *Meat science* **80**, 363-369, doi:10.1016/j.meatsci.2007.12.020 (2008).
9. Ozawa, S. *et al.* The characteristics of muscle fiber types of longissimus thoracis muscle and their influences on the quantity and quality of meat from Japanese Black steers. *Meat science* **54**, 65-70, doi:https://doi.org/10.1016/S0309-1740(99)00072-8 (2000).
10. Ashby, K. D. *et al.* Fluorescence of dietary porphyrins as a basis for real-time detection of fecal contamination on meat. *Journal of agricultural and food chemistry* **51**, 3502-3507, doi:10.1021/jf0211736 (2003).

11. Armstrong, R. B. & Phelps, R. O. Muscle fiber type composition of the rat hindlimb. *The American journal of anatomy* **171**, 259-272, doi:10.1002/aja.1001710303 (1984).

# APPENDIX 2

## MATLAB GUI and Code

### A2.1 Overlay Tissue Imaging System GUI

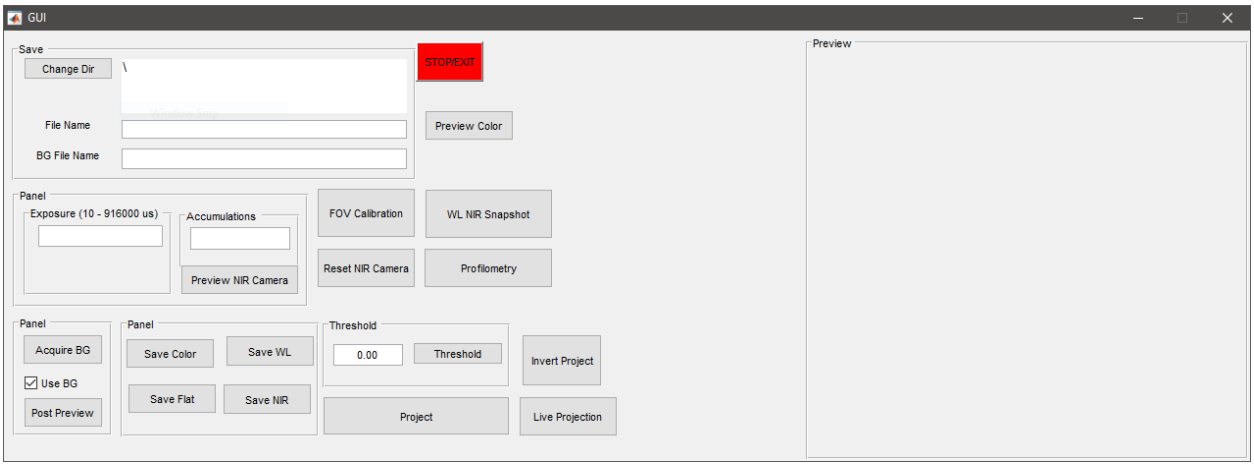


Figure A2-1: MATLAB user interface that allows the clinician to interact with the overlay tissue imaging system.

### A2.2 MATLAB Code

```
function varargout = GUI(varargin)
% GUI MATLAB code for GUI.fig
%      GUI, by itself, creates a new GUI or raises the existing
%      singleton*.
%
%      H = GUI returns the handle to a new GUI or the handle to
%      the existing singleton*.
%
%      GUI('CALLBACK',hObject,eventData,handles,...) calls the
local
%      function named CALLBACK in GUI.M with the given input
arguments.
%      GUI('Property','Value',...) creates a new GUI or raises
the
%      existing singleton*.  Starting from the left, property
value pairs are
%      applied to the GUI before GUI_OpeningFcn gets called.  An
```

```
%      unrecognized property name or invalid value makes
property application
%      stop.  All inputs are passed to GUI_OpeningFcn via
varargin.
%
%      *See GUI Options on GUIDE's Tools menu.  Choose "GUI
allows only one
%      instance to run (singleton)".
%
% See also: GUIDE, GUIDATA, GUIHANDLES

% Edit the above text to modify the response to help GUI

% Last Modified by GUIDE v2.5 06-Dec-2017 07:33:48

% Begin initialization code - DO NOT EDIT
gui_Singleton = 1;
gui_State = struct('gui_Name',       mfilename, ...
                   'gui_Singleton',  gui_Singleton, ...
                   'gui_OpeningFcn', @GUI_OpeningFcn, ...
                   'gui_OutputFcn',  @GUI_OutputFcn, ...
                   'gui_LayoutFcn',  [] , ...
                   'gui_Callback',   []);
if nargin && ischar(varargin{1})
    gui_State.gui_Callback = str2func(varargin{1});
end

if nargout
    [varargout{1:nargout}] = gui_mainfcn(gui_State,
varargin{:});
else
    gui_mainfcn(gui_State, varargin{:});
end
% End initialization code - DO NOT EDIT

% --- Executes just before GUI is made visible.
function GUI_OpeningFcn(hObject, eventdata, handles, varargin)
% This function has no output args, see OutputFcn.
% hObject    handle to figure
% eventdata  reserved - to be defined in a future version of
MATLAB
% handles    structure with handles and user data (see GUIDATA)
% varargin   command line arguments to GUI (see VARARGIN)
imaqreset; reset(gpuDevice);
clc;
```

```
global src src2 direct vid vid2 filename exposure accumulation
bgfilename hFig threshvalue
direct = 'C:\Users\BPL\Desktop\OTIS2 Data'; cd(direct); % set
default save directory
filename = 'test'; %set default file name
bgfilename = 'BG';
exposure = 10; % set default exposure
accumulation = 1;
threshvalue = 0.00;

imaqreset;
imaqhwinfo('gige')
% Initialize NIR Camera
vid = videoinput('gige', 2, 'Mono12'); % Create a Video Input
Output
src = getselectedsource(vid); % Get Camera Parameters
src.AcquisitionFrameRateEnable = 'False';
src.GainAuto = 'Off';
src.AllGainRaw = 0;
src.DigitalAllGainRaw = 0; %max = 95
src.DigitalShift = 0;
src.AnalogAllGainRaw = 3;
src.ExposureAuto = 'Off';
src.PacketSize = 9000;
vid.ROIPosition = [129 1 1025 1025];
vid.FramesPerTrigger = 1;
vid.timeout = 5000;

% Initialize Color Camera
vid2 = videoinput('gige', 1, 'BayerRG12'); % Create a Video
Input Output
src2 = getselectedsource(vid2); % Get Camera Parameters
src2.PacketSize = 9000;
src2.GainAuto = 'Once';
src2.ExposureAuto = 'off';
vid2.FramesPerTrigger = 1;
vid2.timeout = 5000;

% These can be commented out if needed
figure;
mp = get(0, 'MonitorPositions');
hFig = gcf;
hAx  = gca;
% set the figure to full screen
set(hFig,'Position',[mp(2,1)-1 mp(2,2)+1 mp(2,3) mp(2,4)]);
% set the axes to full screen
```

```
set(hAx,'Unit','normalized','Position',[0 0 1 1]);
% hide the toolbar
set(hFig,'menubar','none')
% to hide the title
set(hFig,'NumberTitle','off');
axis off;
set(gcf,'color','k');

% Choose default command line output for GUI
handles.output = hObject;
% Update handles structure
guidata(hObject, handles);
% UIWAIT makes GUI wait for user response (see UIRESUME)
% uiwait(handles.figure1);

% --- Outputs from this function are returned to the command
line.
function varargout = GUI_OutputFcn(hObject, eventdata, handles)
% varargout  cell array for returning output args (see
VARARGOUT);
% hObject    handle to figure
% eventdata  reserved - to be defined in a future version of
MATLAB
% handles    structure with handles and user data (see GUIDATA)
% Get default command line output from handles structure
varargout{1} = handles.output;

% --- Executes on button press in dir_push.
function dir_push_Callback(hObject, eventdata, handles)
% hObject    handle to dir_push (see GCBO)
% eventdata  reserved - to be defined in a future version of
MATLAB
% handles    structure with handles and user data (see GUIDATA)
global direct
direct2 = uigetdir;
if direct2 == 0;
    direct = direct;
else
    direct = direct2;
end
set(handles.dir_statictext, 'String', [direct '\'])
cd(direct);

% --- Executes on slider movement.
function exposure_slider_Callback(hObject, eventdata, handles)
% hObject    handle to exposure_slider (see GCBO)
```

```
% eventdata  reserved - to be defined in a future version of
MATLAB
% handles    structure with handles and user data (see GUIDATA)
% Hints: get(hObject,'Value') returns position of slider
%        get(hObject,'Min') and get(hObject,'Max') to determine
range of slider
global src exposure
set(handles.exposure_edit, 'String', get(hObject,'Value'));
exposure = round(get(hObject,'Value'));
src.ExposureTimeRaw = get(hObject,'Value');

% --- Executes during object creation, after setting all
properties.
function exposure_slider_CreateFcn(hObject, eventdata, handles)
% hObject    handle to exposure_slider (see GCBO)
% eventdata  reserved - to be defined in a future version of
MATLAB
% handles    empty - handles not created until after all
CreateFcns called
global exposure
set(hObject,'Min', 10);
set(hObject,'Max', 916000);
set(hObject, 'Value', exposure); % set default exposure
% Hint: slider controls usually have a light gray background.
if isequal(get(hObject,'BackgroundColor'),
get(0,'defaultUicontrolBackgroundColor'))
    set(hObject,'BackgroundColor',[.9 .9 .9]);
end

% --- Executes during object creation, after setting all
properties.
function exposure_edit_CreateFcn(hObject, eventdata, handles)
% hObject    handle to exposure_edit (see GCBO)
% eventdata  reserved - to be defined in a future version of
MATLAB
% handles    empty - handles not created until after all
CreateFcns called
% Hint: edit controls usually have a white background on
Windows.
%       See ISPC and COMPUTER.
global exposure
set(hObject, 'String', exposure); % set default exposure
if ispc && isequal(get(hObject,'BackgroundColor'),
get(0,'defaultUicontrolBackgroundColor'))
    set(hObject,'BackgroundColor','white');
end
```

```
function exposure_edit_Callback(hObject, eventdata, handles)
% hObject    handle to exposure_edit (see GCBO)
% eventdata  reserved - to be defined in a future version of
MATLAB
% handles    structure with handles and user data (see GUIDATA)
% Hints: get(hObject,'String') returns contents of exposure_edit
as text
%        str2double(get(hObject,'String')) returns contents of
exposure_edit as a double
global src exposure
set(handles.exposure_slider, 'Value',
str2double(get(hObject,'String')));
exposure = round(str2double(get(hObject,'String')));
src.ExposureTimeRaw = str2double(get(hObject,'String'));

function filename_edit_Callback(hObject, eventdata, handles)
% hObject    handle to filename_edit (see GCBO)
% eventdata  reserved - to be defined in a future version of
MATLAB
% handles    structure with handles and user data (see GUIDATA)
% Hints: get(hObject,'String') returns contents of filename_edit
as text
%        str2double(get(hObject,'String')) returns contents of
filename_edit as a double
global filename
filename = get(hObject,'String');

% --- Executes during object creation, after setting all
properties.
function filename_edit_CreateFcn(hObject, eventdata, handles)
% hObject    handle to filename_edit (see GCBO)
% eventdata  reserved - to be defined in a future version of
MATLAB
% handles    empty - handles not created until after all
CreateFcns called
% Hint: edit controls usually have a white background on
Windows.
%       See ISPC and COMPUTER.
if ispc && isequal(get(hObject,'BackgroundColor'),
get(0,'defaultUicontrolBackgroundColor'))
    set(hObject,'BackgroundColor','white');
end
global filename
set(hObject, 'String', filename); % set default save name
```

```
% --- Executes during object creation, after setting all
properties.
function dir_statictext_CreateFcn(hObject, eventdata, handles)
% hObject    handle to dir_statictext (see GCBO)
% eventdata  reserved - to be defined in a future version of
MATLAB
% handles    empty - handles not created until after all
CreateFcns called
global direct
set(hObject, 'String', [direct '\']); % set default save
directory

% --- Executes on button press in save_NIR.
function save_NIR_Callback(hObject, eventdata, handles)
% hObject    handle to save_NIR (see GCBO)
% eventdata  reserved - to be defined in a future version of
MATLAB
% handles    structure with handles and user data (see GUIDATA)
global vid direct filename accumulation bgfilename exposure
cd(direct);

bg=0;
if get(handles.usebg_checkbox, 'Value') == 1;
    bg = double(imread([direct '\' bgfilename '_exp'
num2str(exposure) '_accum' num2str(accumulation) '.tif']));
end
bg = gpuArray(bg);
accum = gpuArray(accumulation);

h = waitbar(0,'Please wait...');
vid.FramesPerTrigger = accumulation;
start(vid);

data = getdata(vid);
flushdata(vid);
stop(vid);
data = gpuArray(data);
data = sum(data,4)/accum;
data = data-bg;
data = gather(data);
close(h);
imwrite(uint16(data), [filename '_exp' num2str(exposure)
'_accum' num2str(accumulation) '.tif']);
imagesc(data, [0 max(max(data))]); axis image; colormap(gray);
axis off; colorbar;
```

```
clear -except vid direct filename accumulation bgfilename

% --- Executes during object creation, after setting all
properties.
function preview_axis_CreateFcn(hObject, eventdata, handles)
% hObject    handle to preview_axis (see GCBO)
% eventdata  reserved - to be defined in a future version of
MATLAB
% handles    empty - handles not created until after all
CreateFcns called
% Hint: place code in OpeningFcn to populate preview_axis
axis off

function accumulations_edit_Callback(hObject, eventdata,
handles)
% hObject    handle to accumulations_edit (see GCBO)
% eventdata  reserved - to be defined in a future version of
MATLAB
% handles    structure with handles and user data (see GUIDATA)
% Hints: get(hObject,'String') returns contents of
accumulations_edit as text
%        str2double(get(hObject,'String')) returns contents of
accumulations_edit as a double
global accumulation
accumulation = str2double(get(hObject,'String'));

% --- Executes during object creation, after setting all
properties.
function accumulations_edit_CreateFcn(hObject, eventdata,
handles)
% hObject    handle to accumulations_edit (see GCBO)
% eventdata  reserved - to be defined in a future version of
MATLAB
% handles    empty - handles not created until after all
CreateFcns called
% Hint: edit controls usually have a white background on
Windows.
%       See ISPC and COMPUTER.
global accumulation
set(hObject, 'String', num2str(accumulation));

if ispc && isequal(get(hObject,'BackgroundColor'),
get(0,'defaultUicontrolBackgroundColor'))
    set(hObject,'BackgroundColor','white');
end
```

```
% --- Executes on button press in NIR_push.
function NIR_push_Callback(hObject, eventdata, handles)
% hObject    handle to NIR_push (see GCBO)
% eventdata  reserved - to be defined in a future version of
MATLAB
% handles    structure with handles and user data (see GUIDATA)
% Hint: get(hObject,'Value') returns toggle state of NIR_push
global vid src accumulation
src.ExposureTimeRaw = get(handles.exposure_slider,'Value');
preview(vid);

% --- Executes on button press in bgsave_push.
function bgsave_push_Callback(hObject, eventdata, handles)
% hObject    handle to bgsave_push (see GCBO)
% eventdata  reserved - to be defined in a future version of
MATLAB
% handles    structure with handles and user data (see GUIDATA)
global vid direct bgfilename accumulation exposure
cd(direct);

h = waitbar(0,'Please wait...');
vid.FramesPerTrigger = accumulation;
start(vid);

data = gpuArray(getdata(vid));
flushdata(vid);
stop(vid);
data = sum(data,4)/accumulation;
data = gather(data);
close(h);
imwrite(uint16(data), [bgfilename '_exp' num2str(exposure)
'_accum' num2str(accumulation) '.tif']);
imagesc(data, [0 max(max(data))]); axis image; axis off;
colormap(gray); colorbar;
clear -except vid direct bgfilename accumulation;

function bgfilename_edit_Callback(hObject, eventdata, handles)
% hObject    handle to bgfilename_edit (see GCBO)
% eventdata  reserved - to be defined in a future version of
MATLAB
% handles    structure with handles and user data (see GUIDATA)
% Hints: get(hObject,'String') returns contents of
bgfilename_edit as text
%        str2double(get(hObject,'String')) returns contents of
bgfilename_edit as a double
global bgfilename
```

```
bgfilename = get(hObject,'String');


% --- Executes during object creation, after setting all
properties.
function bgfilename_edit_CreateFcn(hObject, eventdata, handles)
% hObject    handle to bgfilename_edit (see GCBO)
% eventdata  reserved - to be defined in a future version of
MATLAB
% handles    empty - handles not created until after all
CreateFcns called
% Hint: edit controls usually have a white background on
Windows.
%       See ISPC and COMPUTER.
if ispc && isequal(get(hObject,'BackgroundColor'),
get(0,'defaultUicontrolBackgroundColor'))
    set(hObject,'BackgroundColor','white');
end
global bgfilename
set(hObject, 'String', bgfilename); % set default save name

% --- Executes on button press in usebg_checkbox.
function usebg_checkbox_Callback(hObject, eventdata, handles)
% hObject    handle to usebg_checkbox (see GCBO)
% eventdata  reserved - to be defined in a future version of
MATLAB
% handles    structure with handles and user data (see GUIDATA)
% Hint: get(hObject,'Value') returns toggle state of
usebg_checkbox

% --- Executes on button press in preview_toggle.
function preview_toggle_Callback(hObject, eventdata, handles)
% hObject    handle to preview_toggle (see GCBO)
% eventdata  reserved - to be defined in a future version of
MATLAB
% handles    structure with handles and user data (see GUIDATA)
global vid accumulation direct bgfilename exposure

vid.FramesPerTrigger = accumulation;
accum = gpuArray(accumulation);

if get(handles.usebg_checkbox, 'Value') == 1;
    bg = double(imread([direct '\' bgfilename '_exp'
num2str(exposure) '_accum' num2str(accumulation) '.tif']));
    bg = gpuArray(bg);
end
```

```
if get(hObject, 'Value') == 1;
    h = waitbar(0, 'please wait...');
    vid.TriggerRepeat = inf;
    start(vid);
    close(h);
    while islogging(vid);


        data = getdata(vid);
        flushdata(vid);
        data = gpuArray(data);
        data = sum(data,4)/accum;
        if get(handles.usebg_checkbox, 'Value') == 1;
            data = data - bg;
        end
        data = gather(data);
        handles.preview_axis = imshow(data, 'DisplayRange', []);
colorbar;
        drawnow;
        clear data;
    end
else
    h = waitbar(0, 'please wait');
    stop(vid);
    flushdata(vid);
    vid.TriggerRepeat = 1;
    close(h);
    clear -except vid accumulation direct bgfilename
end

% --- Executes during object creation, after setting all
properties.
function usebg_checkbox_CreateFcn(hObject, eventdata, handles)
% hObject    handle to usebg_checkbox (see GCBO)
% eventdata  reserved - to be defined in a future version of
MATLAB
% handles    empty - handles not created until after all
CreateFcns called
set(hObject, 'Value', 1);

% --- Executes on button press in Save_Color.
function Save_Color_Callback(hObject, eventdata, handles)
% hObject    handle to Save_Color (see GCBO)
% eventdata  reserved - to be defined in a future version of
MATLAB
```

```
% handles    structure with handles and user data (see GUIDATA)
global vid2 filename direct exposure accumulation hFig src2
src2.ExposureTimeRaw = exposure;
vid2.FramesPerTrigger = accumulation;

cd(direct);
h = waitbar(0,'Please wait...');

%figure(hFig); imshow('white.png'); axis image;
%pause(1);
%src2.ExposureAuto = 'Continuous';

start(vid2);
img = getdata(vid2);
stop(vid2);
flushdata(vid2);
img = flipud(fliplr(img));
close(h);
%figure(hFig); imshow('black.png'); axis image;

%src2.ExposureAuto = 'Off';
%src2.ExposureTimeRaw = exposure;

img = sum(img,4)/vid2.FramesPerTrigger;
img = uint16(img);

figure;
imshow(img); axis image; axis off;
imwrite(img, [filename '_exp' num2str(src2.ExposureTimeRaw)
'_accum' num2str(vid2.FramesPerTrigger) '_color.tif'], 'tif');
%imwrite(img, [filename '_exp_AUTO' 'accum_'
num2str(vid2.FramesPerTrigger) '_color.tif'], 'tif');
clearvars -except filename direct hFig src2

% --- Executes on button press in save_wl.
function save_wl_Callback(hObject, eventdata, handles)
% hObject    handle to save_wl (see GCBO)
% eventdata  reserved - to be defined in a future version of
MATLAB
% handles    structure with handles and user data (see GUIDATA)
global vid direct filename accumulation exposure src hFig
cd(direct);

h = waitbar(0,'Please wait...');
vid.FramesPerTrigger = accumulation;
```

```
%figure(hFig); imshow('white.png'); axis image;
start(vid);
data = getdata(vid);
flushdata(vid);
stop(vid)
%figure(hFig); imshow('black.png'); axis image;

data = sum(data,4)/accumulation;
close(h);
imwrite(uint16(data), [filename '_exp' num2str(exposure)
'_accum' num2str(accumulation) '_WL.tif']);
figure;
imagesc(data, [0 max(max(data))]); axis image; colormap(gray);
axis off; colorbar;
clearvars -except vid direct filename accumulation hFig


% --- Executes on button press in Save_Flat.
function Save_Flat_Callback(hObject, eventdata, handles)
% hObject    handle to Save_Flat (see GCBO)
% eventdata  reserved - to be defined in a future version of
MATLAB
% handles    structure with handles and user data (see GUIDATA)
global vid direct filename accumulation bgfilename exposure
cd(direct);

bg = double(imread([direct '\' bgfilename '_exp'
num2str(exposure) '_accum' num2str(accumulation) '.tif']));
h = waitbar(0,'Please wait...');
vid.FramesPerTrigger = accumulation;
start(vid);

data = getdata(vid);
flushdata(vid); stop(vid)
data = sum(data,4)/accumulation-bg;
close(h);
imwrite(uint16(data), [filename '_exp' num2str(exposure)
'_accum' num2str(accumulation) '_Flat.tif']);
imagesc(data, [0 max(max(data))]); axis image; colormap(gray);
axis off; colorbar;
clearvars -except vid direct filename accumulation


% --- Executes on button press in Push_Threshold.
function Push_Threshold_Callback(hObject, eventdata, handles)
% hObject    handle to Push_Threshold (see GCBO)
```

```
% eventdata  reserved - to be defined in a future version of
MATLAB
% handles    structure with handles and user data (see GUIDATA)
global direct filename thresh threshvalue exposure accumulation
cd(direct);

img = imread([direct '\' filename '_exp' num2str(exposure)
'_accum' num2str(accumulation) '.tif']);
level = graythresh(img)+threshvalue; %autothresholding
img = im2bw(img, level); %binary threshold
img = gpuArray(img);
img = medfilt2(img, [3 3]); %median filter
thresh = gather(img);
imshow(thresh); axis image;

clear -except vid direct filename thresh threshvalue

% --- Executes on button press in Push_Project.
function Push_Project_Callback(hObject, eventdata, handles)
% hObject    handle to Push_Project (see GCBO)
% eventdata  reserved - to be defined in a future version of
MATLAB
% handles    structure with handles and user data (see GUIDATA)
global thresh hFig

figure(hFig)
cmap = [0 0 0; 0 1 0];
if get(hObject,'Value') == 1;
    figure(hFig)
    imshow(thresh);%imtranslate(thresh,[500 500])); axis image;
    zoom(1.165); %1.165
    colormap(cmap);
elseif get(hObject,'Value') == 0;
    figure(hFig)
    imshow('black.png');
end
clearvars -except hfig thresh

% --- Executes on button press in Toggle_FOV.
function Toggle_FOV_Callback(hObject, eventdata, handles)
% hObject    handle to Toggle_FOV (see GCBO)
% eventdata  reserved - to be defined in a future version of
MATLAB
% handles    structure with handles and user data (see GUIDATA)
% Hint: get(hObject,'Value') returns toggle state of Toggle_FOV
global hFig
```

```
if get(hObject,'Value') == 1;
    figure(hFig)
    imshow('FOV Focus.png'); axis image;
elseif get(hObject,'Value') == 0;
    figure(hFig)
    imshow('black.png'); axis image;
end
clearvars -except hfig

function ThreshValue_Callback(hObject, eventdata, handles)
% hObject    handle to ThreshValue (see GCBO)
% eventdata  reserved - to be defined in a future version of
MATLAB
% handles    structure with handles and user data (see GUIDATA)
% Hints: get(hObject,'String') returns contents of ThreshValue
as text
%        str2double(get(hObject,'String')) returns contents of
ThreshValue as a double
global direct filename thresh threshvalue exposure accumulation
threshvalue = str2double(get(hObject,'String'));

cd(direct);

img = imread([direct '\' filename '_exp' num2str(exposure)
'_accum' num2str(accumulation) '.tif']);
level = graythresh(img)+threshvalue; %autothresholding
img = im2bw(img, level); %binary threshold
img = gpuArray(img);
img = medfilt2(img, [3 3]); %median filter
thresh = gather(img);
imshow(thresh); axis image;

clear -except vid direct filename thresh threshvalue

% --- Executes during object creation, after setting all
properties.
function ThreshValue_CreateFcn(hObject, eventdata, handles)
% hObject    handle to ThreshValue (see GCBO)
% eventdata  reserved - to be defined in a future version of
MATLAB
% handles    empty - handles not created until after all
CreateFcns called
% Hint: edit controls usually have a white background on
Windows.
%       See ISPC and COMPUTER.
```

```
global threshvalue
set(hObject, 'Value', threshvalue); % set default exposure
if ispc && isequal(get(hObject,'BackgroundColor'),
get(0,'defaultUicontrolBackgroundColor'))
    set(hObject,'BackgroundColor','white');
end

% --- Executes on button press in LiveProjection.
function LiveProjection_Callback(hObject, eventdata, handles)
% hObject    handle to LiveProjection (see GCBO)
% eventdata  reserved - to be defined in a future version of
MATLAB
% handles    structure with handles and user data (see GUIDATA)
% Hint: get(hObject,'Value') returns toggle state of
LiveProjection
global vid accumulation direct bgfilename threshvalue hFig
exposure

vid.FramesPerTrigger = accumulation;
accum = gpuArray(accumulation);

cmap = [0 0 0; 0 1 0];

if get(handles.usebg_checkbox, 'Value') == 1;
    bg = double(imread([direct '\' bgfilename '_exp'
num2str(exposure) '_accum' num2str(accumulation) '.tif']));
    bg = gpuArray(bg);
end

if get(hObject, 'Value') == 1;
    imshow('black.png', 'Parent', handles.preview_axis);


    h = waitbar(0, 'please wait...');
    vid.TriggerRepeat = inf;
    start(vid);
    close(h);
    while islogging(vid);

        while get(vid,'FramesAvailable')<1  %Wait until at least
1 frame is available
            unavailable=1;
        end

        data = gpuArray(getdata(vid));
        flushdata(vid);
```

```
        data = sum(data,4)/accum;
        if get(handles.usebg_checkbox, 'Value') == 1;
            data = data - bg;
        end
        img = gather(uint16(data));
        level = graythresh(img)+threshvalue; %autothresholding
        img = im2bw(img, level); %binary threshold
        img = gpuArray(img);
        img = medfilt2(img, [3 3]); %median filter
        thresh = gather(img);

        figure(hFig);
        imshow(thresh, 'Colormap', cmap); axis image;
        zoom(1.165); %1.165
        %drawnow;
        clearvars data thresh level;
    end
else
    h = waitbar(0, 'please wait');
    stop(vid);
    flushdata(vid);
    vid.TriggerRepeat = 1;
    close(h);
    clearvars -except vid accumulation direct bgfilename
threshvalue
end

% --- Executes on button press in STOP.
function STOP_Callback(hObject, eventdata, handles)
% hObject    handle to STOP (see GCBO)
% eventdata  reserved - to be defined in a future version of
MATLAB
% handles    structure with handles and user data (see GUIDATA)
close all; clear all; reset(gpuDevice); close(GUI);

% --- Executes on button press in ResetNIR.
function ResetNIR_Callback(hObject, eventdata, handles)
% hObject    handle to ResetNIR (see GCBO)
% eventdata  reserved - to be defined in a future version of
MATLAB
% handles    structure with handles and user data (see GUIDATA)
global src vid
src.AcquisitionFrameRateEnable = 'False';
src.GainAuto = 'Off';
src.AllGainRaw = 0;
src.DigitalAllGainRaw = 0; %max = 95
```

```
src.DigitalShift = 0;
src.AnalogAllGainRaw = 3;
src.ExposureAuto = 'Off';
src.PacketSize = 9000;
vid.ROIPosition = [129 1 1025 1025];
vid.FramesPerTrigger = 1;
vid.timeout = 5000;

% --- Executes on button press in WL_NIR.
function WL_NIR_Callback(hObject, eventdata, handles)
% hObject    handle to WL_NIR (see GCBO)
% eventdata  reserved - to be defined in a future version of
MATLAB
% handles    structure with handles and user data (see GUIDATA)
global vid direct filename src hFig accumulation exposure
cd(direct);

h = waitbar(0,'Please wait...');
%vid.FramesPerTrigger = accumulation;
vid.FramesPerTrigger = 100;

%start(vid);
%bg = getdata(vid);
%flushdata(vid);
%stop(vid)

figure(hFig); imshow('white.png'); axis image;
pause(1);
src.ExposureAuto = 'Continuous';

start(vid);
data = getdata(vid);
flushdata(vid);
stop(vid)
figure(hFig); imshow('black.png'); axis image;

src.ExposureAuto = 'Off';
src.ExposureTimeRaw = exposure;

data = (sum(data,4)/vid.FramesPerTrigger); %-
(sum(bg,4)/accumulation);
close(h);
%imwrite(uint16(data), [filename '_exp' num2str(exposure)
'_accum' num2str(accumulation) '_WLNIR.tif']);
imwrite(uint16(data), [filename '_exp_AUTO' '_accum'
num2str(vid.FramesPerTrigger) '_WLNIR.tif']);
```

```
figure;
imagesc(data, [0 max(max(data))]); axis image; colormap(gray);
axis off; colorbar;
clearvars -except vid direct filename accumulation hFig


% --- Executes on button press in Profilometry.
function Profilometry_Callback(hObject, eventdata, handles)
% hObject    handle to Profilometry (see GCBO)
% eventdata  reserved - to be defined in a future version of
MATLAB
% handles    structure with handles and user data (see GUIDATA)
global hFig vid accumulation filename exposure direct

cd(direct);

freq = 0.1;

vid.FramesPerTrigger = accumulation;

h = waitbar(0,'Please wait...');

figure(hFig);
imshow('black.png'); axis image; axis off;

start(vid);
bg = getdata(vid);
flushdata(vid);
stop(vid)

for x = 1:4;

    image = square(freq*[1:1025]'+deg2rad(90*(x-
1))+pi/2)*ones(1, 1025);
    imshow(rot90(image));

    start(vid);
    temp = getdata(vid);
    flushdata(vid);
    stop(vid);

    data(:,:,x) = (sum(temp,4)/accumulation)-
(sum(bg,4)/accumulation);

    clear temp;
end
```

```
close(h);


imwrite(uint16(data), [filename '_exp' num2str(exposure)
'_accum' num2str(accumulation) '_profile.tif']);
figure;
imagesc(data(:,:,1), [0 max(max(data(:,:,1)))]); axis image;
colormap(gray); axis off; colorbar;
clear data


% --- Executes on button press in PreviewColor.
function PreviewColor_Callback(hObject, eventdata, handles)
% hObject    handle to PreviewColor (see GCBO)
% eventdata  reserved - to be defined in a future version of
MATLAB
% handles    structure with handles and user data (see GUIDATA)
global vid2 src2 accumulation
src2.ExposureTimeRaw = get(handles.exposure_slider,'Value');
preview(vid2);


% --- Executes on button press in push_invert.
function push_invert_Callback(hObject, eventdata, handles)
% hObject    handle to push_invert (see GCBO)
% eventdata  reserved - to be defined in a future version of
MATLAB
% handles    structure with handles and user data (see GUIDATA)
global thresh hFig

figure(hFig)
cmap = [0 0 0; 0 1 0];
if get(hObject,'Value') == 1;
    figure(hFig)
    imshow(imcomplement(thresh));%imtranslate(thresh,[500
500])); axis image;
    zoom(1.165); %1.165
    colormap(cmap);
elseif get(hObject,'Value') == 0;
    figure(hFig)
    imshow('black.png');
end
clearvars -except hfig thresh
```